THESIS

# DESCRIPTION AND EVALUATION OF THE CASA DUAL-DOPPLER SYSTEM

Submitted by
Matthew Martinez
Department of Electrical and Computer Engineering

In partial fulfillment of the requirements
for the Degree of Master of Science
Colorado State University
Fort Collins, Colorado
Spring 2011

Master's Committee

Advisor: Chandrasekar V. Chandra

Branislav Notaros
Paul W. Mielke

# ABSTRACT

## DESCRIPTION AND EVALUATION OF THE CASA DUAL-DOPPLER SYSTEM

Long range weather surveillance radars are designed for observing weather events for hundreds of kilometers from the radar and operate over a large coverage domain independently of weather conditions. As a result a loss in spatial resolution and limited temporal sampling of the weather phenomenon occurs. Due to the curvature of the Earth, long-range weather radars tend to make the majority of their precipitation and wind observations in the middle to upper troposphere, resulting in missed features associates with severe weather occurring in the lowest three kilometers of the troposphere. The spacing of long-range weather radars in the United States limits the feasibility of using dual-Doppler wind retrievals that would provide valuable information on the kinematics of weather events to end-users and researchers.

The National Science Foundation Center for Collaborative Adapting Sensing of the Atmosphere (CASA) aims to change the current weather sensing model by increasing coverage of the lowest three kilometers of the troposphere by using densely spaced networked short-range weather radars. CASA has deployed a network of these radars in south-western Oklahoma, known as Integrated Project 1 (IP1). The individual radars are adaptively steered by an automated system known as the Meteorological Command and Control (MCC). The geometry of the IP1 network is such that the coverage domains of the individual radars are overlapping.

A dual-Doppler system has been developed for the IP1 network which takes advantage of the overlapping coverage domains. The system is comprised of two subsystems, scan optimization and wind field retrieval. The scan strategy subsystem uses the DCAS model and the number of dual-Doppler pairs in the IP1 network to minimizes the normalized standard deviation in the wind field retrieval. The scan strategy subsystem also minimizes the synchronization error between two radars. The retrieval itself is comprised of two steps, data resampling and the retrieval process. The resampling step map data collected in radar coordinates to a common Cartesian grid. The retrieval process uses the radial velocity measurements to estimate the northward, eastward, and vertical component of the wind. The error in the retrieval is related to the beam crossing angle. The best retrievals occur at beam crossing angles greater than 30°.

During operations statistics on the scan strategy and wind field retrievals are collected in real-time. For the scan strategy subsystem statistics on the beam crossing angels, maximum elevation angle, number of elevation angles, maximum observable height, and synchronization time between radars in a pair are collected by the MCC. These statistics are used to evaluate the performance of the scan strategy subsystem. Observations of a strong wind event occurring on April 2, 2010 are used to evaluate the decision process associated with the scan strategy optimization. For the retrieval subsystem, the normalized standard deviation for the wind field retrieval is used to evaluate the quality of the retrieval. Wind fields from an EF2 tornado observed on May 14, 2009 are used to evaluate the quality of the wind field retrievals in hazardous wind events.

Two techniques for visualizing vector fields are available, streamlines and arrows. Each visualization technique is evaluated based on the task of visualizing small and large scale phenomenon. Applications of the wind field retrievals include the computation of the vorticity and divergence fields. Vorticity and divergence for an EF2 tornado observed on May 14, 2009 are evaluated against vorticity and divergence for other observed tornadoes.

# ACKNOWLEDGEMENTS

This work was supported by the Engineering Research Centers Program of the National Science Foundation under NSF Award Number 0313747, the National Science Foundation Bridge to the Doctorate Fellowship Program, and the NASA Earth and Space Science Fellowship Program.

# DEDICATION

To my wife Christine who never stopped believing in me

# TABLE OF CONTENTS

## LIST OF FIGURES

# LIST OF TABLES

# CHAPTER 1

# INTRODUCTION

## 1.1 Introduction

Current weather surveillance radars are designed for observing weather events for hundreds of kilometers from the radars. Large S-band weather radars, such as the Weather Surveillance Radar-1988 Doppler (WSR-88D or NEXRAD), used by the National Weather Service (NWS), are capable of observing weather at a maximum unambiguous range of 460 km (Crum and Alberty, 1993). These radars tend to operate over a large coverage domain and independently of weather conditions. As a result of this operational paradigm a loss in spatial resolution and limited temporal sampling of the weather phenomenon occurs. Due to the curvature of the Earth, long-range weather radars tend to make the majority of their precipitation and wind observations in the middle to the upper troposphere, which results in missed features associates with severe weather occurring in the lowest three kilometers of the troposphere. In addition, the spacing of WSR-88Ds in the United States limits the feasibility of using dual-Doppler wind retrievals that would otherwise provide valuable information on the dynamics of weather events to end-users and researchers.

To overcome the weaknesses of the WSR-88D, the National Science Foundation Engineering Research Center for Collaborative Adaptive Sensing of the Atmosphere (CASA) is working to change the current model for sensing weather. CASA is a collaborative research project between four core partner universities (Colorado State

University, the University of Massachusetts (lead university), the University of Oklahoma, and the University of Puerto Rico at Mayagez) and a partnership between various industry and government partners. The objective of CASA is to increase coverage of the lower three kilometers of the troposphere by deploying densely spaced networked short-range weather radars. As a proof of concept CASA has deployed a network of four short-range X-band, automated, agile radars with overlapping coverage domains in southwestern Oklahoma, known as Integrative Project 1 (IP1). Figure 1.1 shows a map of the location of the IP1 radars. The The IP1 radars can be divided into two main systems. The individual radars and the Meteorological Command and Control (MCC). The main role of the MCC is to adaptively steer the radars by optimizing the radar scan strategy based on end user needs and current weather conditions. This effectively creates a coordinated scan strategy for the IP1 radars.

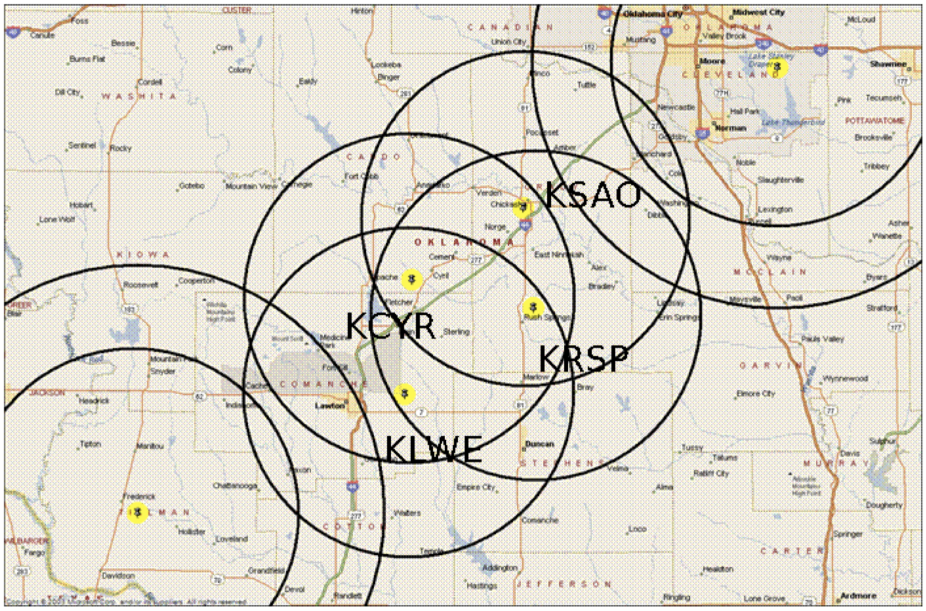

Figure 1.1: Map showing the location of the IP1 radars

Armijo (1969) showed that two Doppler (dual-Doppler) radars can be used to retrieve the magnitude and direction of the wind for a three dimensional wind field. It was shown by Ray et al. (1978, 1980) that multiple Doppler radars (multi-Doppler) can be used for wind field retrievals. The dual- and multi-Doppler techniques have implemented in several radar systems. Mohr and Vaughan (1979) describes the use of a dual-Doppler system for Cooperative Convective Precipitation Experiment (CCOPE), Chong et al. (2000) used a real-time dual-Doppler system during the Mesoscale Alpine Programme Special Observing Period, Dolan and Rutledge (2007) described the dual-Doppler capabilities along the Wyoming and Colorado Front Range, and Chandrasekar et al. (2010a) described the dual-Doppler system developed for the CASA-IP1 testbed. The dual-Doppler technique has also been extended to bistatic radar systems (Protat and Zawadzki, 1999; Satoh and Wurman, 2003; Friedrich and Hagen, 2004). Dual-Doppler observations have mainly been used to study kinematics of weather events. Heymsfield (1978), Ray et al. (1980), and Wurman et al. (2007a) have used wind field retrievals to study the kinematics and structure of tornados observed by dual- and multi-Doppler radar networks. The kinematics of convective storms using wind field retrievals have been studied by Ray et al. (1978), Kessinger et al. (1987), and Dolan and Rutledge (2010).

Because the CASA IP1 testbed is a network of short range radars with overlapping coverage domains it is advantageous for retrieving three dimensional wind fields within the network. The IP1 testbed is designed such that there are several possible dual- and triple-Doppler regions, and a single quad-Doppler region where the wind field can be retrieved. In order to retrieve the wind fields surrounding the IP1 network a dual-Doppler system has been developed. The system is made up of two subsystems, the scan strategy subsystem, and the retrieval subsystem. The scan strategy subsystem, embedded inside the MCC, determines the best possible regions to retrieve the wind field based on the location of a storm cell and provides a decision to the MCC on how the radars should be steered. The retrieval subsystem is responsible for resampling reflectivity and velocity data to a common Cartesian grid and then retrieving the horizontal wind field. Once a wind field is retrieved the data from the dual-Doppler system is provided to end users.

## 1.2 Focus of Thesis

The main focus of this thesis is on the detailed description and characterization, and evaluation of the CASA dual-Doppler system. The description of the CASA dual-Doppler system will provide an overview of the system as a whole, focusing on dual-Doppler coverage in the IP1 network, and the two main subsystems. The description and characterization of the dual-Doppler coverage in the IP1 network will focus on the number of pairs in the network, and dual-Doppler capacity of each pair. The description of the scan strategy subsystem will provide a specification of the implemented dual-Doppler scan optimization, the best pair regions within the IP1 network, and the dual-Doppler capacity of the entire network. The description of the retrieval subsystem will focus on specifications of the subsystem and will give example wind field retrievals from events occurring on during the 2009 and 2010 spring experiments.The evaluation portion of this thesis will focus on how well each subsystem performed during the 2009 spring experiment. Case studies will be used to highlight the performance of each subsystem during specific events. The first cases study is from April 2, 2010, a hazardous wind event, which will focus on the performance of the dual-Doppler scan strategy subsystem when there is significant attenuation in dual-Doppler regions. The second case study is from May 14, 2009, a tornado event. This case study will focus on the quality of the wind field retrievals during a hazardous weather event. Finally applications of the dual-Doppler data will be provided.

## 1.3 Organization of Thesis

This thesis is organized into five chapters. Chapter 2 will provide a description of the CASA Integrative Project 1 (IP1) radar system and the two data fields, reflectivity and velocity, which are important to wind field retrievals. The specifications of each subsystem will be discussed and the theory for computing reflectivity and velocity from radar measurements will be given. Chapter 3 will focus on the necessary theory needed for wind field retrieval (data resampling, horizontal wind retrieval, and vertical wind retrieval) and will provide a characterization of the CASA dual-Doppler system. The characterization will be done for the dual-Doppler coverage in the IP1 network, and the two major subsystems, scan strategy and retrieval. Chapter 4 will provide an evaluation of the two subsystems, also applications of the dual-Doppler system will be provided. The evaluation of the scan strategy subsystem will focus on the dual-Doppler coverage in the IP1 network, the vertical coverage in each scan, and how well the data is synchronized between a pair of radars. The evaluation of the retrieval subsystem will discuss the quality of the dual-Doppler retrievals for a merged wind field. A demonstration of how the dual-Doppler data can be used to compute vorticity and divergence fields will also be given. Chapter 5 will conclude the thesis by summarizing the key results and provide suggestions for future work.

# CHAPTER 2

# CASA IP1 RADAR SYSTEM

## 2.1 Introduction

The CASA IP1 testbed is designed as a proof of concept for a new paradigm in remote sensing of the atmosphere. The testbed, located in southwester Oklahoma, uses short wave length technology to scan the lowest altitudes of the troposphere. The testbed also uses an automated system, meteorological command and control (MCC), to scan the IP1 domain based on the features of the current weather or short predictions of the weather. The radar system is divided into five separate subsystems. The antenna, transmitter, receiver, data acquisition, and signal processor. These subsystems transmit and receive weather signals and then computes measurements, i.e. reflectivity, velocity, of the sensed weather. These measurements are then used in further processing and analysis. For wind field retrievals the most important measurements are reflectivity and velocity. The reflectivity from two or more radars is used to create a composite reflectivity field. The velocity data from two or more radars is used to retrieve the wind field in the overlapping coverage domains of the IP1 network. The retrieved winds are then overlaid over the composite reflectivity field. Section 2.2 will describe the IP1 radars and the MCC, and section 2.3 will describe the data used for wind field retrievals.

Table 2.1: Location and FCC identifier for CASA radars

| Location | FCC Identifier | Latitude (°) | Longitude (°) | Altitude (m) |
|---|---|---|---|---|
| Chickasha | KSAO | 35.0312 | -97.9567 | 353.99 |
| Rush Springs | KRSP | 34.8129 | -97.9313 | 414.84 |
| Lawton | KLWE | 34.6238 | -98.2720 | 377.45 |
| Cyril | KCYR | 34.8739 | -98.2514 | 445.30 |

## 2.2 System Description

The IP1 test bed is a network of four low-power, short-range, dual-polarized Doppler radars with overlapping coverage domains. The radars are controlled by an automation system (MCC) that maximizes the value of the radar observations (Junyent et al., 2010; Zink et al., 2005). At each radar clutter filtering, spectral moment processing, and attenuation correction are performed. The results of the computations are stored in network common data format (netCDF). Once the netCDF file is created it is sent over internet to the System Operation and Control Center (SOCC), which runs the MCC algorithms such as wind field retrievals and nowcasting. The SOCC is located in the National Weather Center building in Norman, Oklahoma.

The IP1 test bed is deployed in southwestern Oklahoma. The locations of the radars are in Chickasha, Rush Spring, Lawton, and Cyril. Table 2.1 gives the FCC identifier and the latitude, longitude, and altitude for the individual radars. The radars are approximately 30 kilometer apart (Junyent et al., 2010).

The IP1 radars use magnetron transmitters that operate at about 9.41 GHz. Specifications for the IP1 transmitter are given in table 2.2. The radars transmit a 660 ns pulse at a maximum average power of 25 W. At a pulse repetition frequency (PRF) of 1kHz the unambiguous velocity would be around ±7m/s (Junyent et al., 2010), which is not suitable for weather applications since velocities exceeding ±25m/s are easily observed. To increase the systems unambiguous velocity a dual-PRF scheme is used (Bharadwaj et al., 2010). $\mathrm{PRF}_1$ for this scheme is at 1.6 kHz and $\mathrm{PRF}_2$ is at

Table 2.2: Specifications for CASA radar's transmitter

| Transmitter | |
|---|---|
| Type | Magnetron |
| Center Frequency | 9.41 GHz |
| Peak power output | 8.0 kW (per channel) |
| Average peak power | 12 W (per channel) |
| Pulse width | 660  1000 ns |
| Polarization | Dual linear, horizontal and vertical |
| Max duty cycle | 0.16% |

Table 2.3: Specifications for CASA radar's antenna

| Atenna | |
|---|---|
| Type | Dual-polarized parabolic center feed reflector |
| Diameter | 1.2 m |
| 3-dB beamwidth | 1.80° |
| Gain | 38.0 dB |

2.4 kHz. $PRF_1$ is transmitted for 40 pulses and $PRF_2$ is transmitted for 54 pulses. This method increases the unambiguous velocity to $\pm 38.3$m/s.

The antenna used for the individual radars is a dual-Polarized parabolic center feed reflector. The antenna is mounted on an agile azimuth pedestal, which is limited to a maximum elevation angle of 35° (Junyent et al., 2010). The elevation limitation is not a concern since the system is intended to scan at low elevations. During operations the radar scans at 21° per seconds in azimuth. Table 2.3 summarizes the specifications of the IP1 radar antennas.

A characteristic of the IP1 radars is the ability to perform adaptive coordinated scans. The optimal set of scan tasks are determined in real-time by the MCC and updated every 60 seconds (from now on referred to as the system heartbeat). The scan tasks are then fed back to the radars (Junyent et al., 2010). In normal operation the MCC chooses elevation angles from the set $\{1, 2, 3, 5, 7, 9, 13, 16, 19\}$ (from here on this be referred to as standard mode), all angles are in degrees. The radars are able to operate in other modes, for instance CLASIC (Cloud and Land Surface Interaction Campaign (Miller et al., 2007)) mode and multi-heartbeat mode. In CLASIC mode a longer heartbeat (2 minutes) is used and the elevation angles are chosen from a larger set then in the standard mode. A typical elevation angle set for CLASIC mode is $\{1, 3, 15, 5.28, 7.40, 9.50, 11.57, 13.62, 15.92, 18.57, 21.57, 24.95, 28.70\}$. In multi-heartbeat mode the radars collect data using a user specified set of elevation angles, but the data collection time is not fixed to a specific interval. For this mode each radar will collect data at different intervals depending on the number of elevation angles in the set. Data collection mode does not have an effect on wind field retrievals. Since the scanning is adaptive, a scan task does not necessarily use all the possible elevation angles, and does not make full PPI scans for each elevation angle in the task (except during normal operation the $2^\circ$ scan is a full PPI).

The IP1 radars use a dual channel coherent on receive receiver. One channel for horizontal polarization and the other channel for vertical polarization. The analog receiver receives the signal at the RF frequency and then converts to an intermediate frequency (IF). The IF signal is then sampled by the digital receiver where the signal is digitally down converted to based band. The specifications for the receiver are given in table 2.4. In the digital down conversion the received signal is output as inphase (I) and quadrature (Q) components. From Bringi and Chandrasekar (2001) the I and Q components for a pulsed Doppler radar are expressed as:

$$I(t) = Acos(2\pi f_0 \tau) U_{tr}(t - \tau) \tag{2.1}$$

$$Q(t) = -Asin(2\pi f_0 \tau) U_{tr}(t - \tau) \tag{2.2}$$

Where $U_{tr}$ is the function describing the transmit waveform. The I and Q components are used to compute reflectivity, spectral moments, and dual-polarization products.

Table 2.4: Specifications for CASA radar's receiver

| Receiver | |
|---|---|
| Type | Dual-channel linear output I/Q |
| Dynamic range (BW = 1.5 MHz) | 103 dB |
| Noise Figure | 6.5 dB |
| Sampling Rate | 100 MS $\mathrm{s}^{-1}$ |
| Data transfer rate | 88.3 MB $\mathrm{s}^{-1}$ |

## 2.3 Data Description

At each radar reflectivity, radial velocity, spectrum width and dual-polarized (dual-pol) products are produced. Prior to the computation of products, ground clutter contamination is removed using an adaptive spectral clutter filter (Bharadwaj et al., 2010) similar to Gaussian model adaptive processing (GMAP) (Siggia and Passarelli, 2004). Some of the assumptions made during the clutter filtering process is that both ground clutter and weather spectral density functions are Gaussian, the spectral width of clutter is less then weather, and that clutter has very narrow Doppler spectrum width and is centered at zero Doppler velocity (Bharadwaj et al., 2010). After the clutter filtering process, reflectivity, spectral moments and dual-polarization moments are computed. For wind field retrievals reflectivity and velocity are the most important parameters. Velocity is used to compute the wind field, and the retrieved wind field is then overlaid over a composite reflectivity field. Section 2.3.1 and 2.3.2 describe the computation of reflectivity and velocity, respectively.

### 2.3.1 Reflectivity

A weather signal is a combination of echoes from a large number of hydrometers. The received voltage at range time $\tau_s$ is given as:

$$V(\tau_s) = \frac{1}{\sqrt{2}} \sum_i A_i W_i e^{-j4\pi r_i/\lambda} \tag{2.3}$$

Where $W_i$ is a range dependent weight. The contribution from each scatter to the mean power is:

$$E\left[P_i\right] = \alpha \frac{1}{2} |W_i|^2 E\left[|A_i|^2\right] \tag{2.4}$$

where $P_i$ is the sample time mean power of the individual hydrometeor. As a hydrometeor falls it is subjected to changes in its shape or orientation, therefore the backscatter cross section $\sigma_b$ will oscillate around its mean value. To determine $E\left[P_i\right]$ the mean $\sigma_b$ is needed. If an elemental volume $dV$ containing hydrometeors is considered, then the expected echo power $E\left[dP\right]$ due to $dV$ becomes:

$$E\left[dP\right] = \frac{1}{2} \alpha \sum_i |W_i|^2 E\left[|A_i|^2\right] \tag{2.5}$$

Relating the $E\left[dP\right]$ to the received power for a point scatter, $E\left[dP\right]$ becomes:

$$E\left[dP\right] = \left(\frac{cT_0}{2}\right) \left[\frac{\lambda^2 P_t G_0^2}{(4\pi)^3}\right] \left[\frac{\pi \theta_1 \phi_1}{8ln2}\right] dV \int_0^\infty \sigma_b(D) N(D,r) dD \tag{2.6}$$

Where c is the speed of light, $T_0$ is the pulse width, $P_t$ is the transmitted power, $G_0$ is the antenna gain, $\theta_1$ and $\phi_1$ are the $3-dB$ beamwidths, $D$ is the diameter of the hydrometeor, and $N(D,r)$ is the hydrometeor size distribution. Let

$$\eta(r) = \int_0^\infty \sigma_b N(D,r) dD \tag{2.7}$$

Integrating over $r$, $\theta$ and $\phi$, the received power then becomes

$$\overline{P}_r\left(r_0\right) = \left(\frac{cT_0}{2}\right) \left[\frac{\lambda^2 P_t G_0^2}{(4\pi)^3}\right] \left[\frac{\pi \theta_1 \phi_1}{8ln2}\right] \frac{\eta\left(r_0\right)}{r_0^2} \tag{2.8}$$

Where $\eta_{r_0}$ is the back scatter cross section per unit volume. In radar meteorology it is conventional to express $\eta$ in terms of the equivalent reflectivity factor $Z_e$ which is defined as:

$$Z_e = \frac{\lambda^4}{\pi^5 |K_w|^2} \eta \tag{2.9}$$

Where $K_w$ is the dielectric factor for water. Substituting equation 2.9 into equation 2.8 yields:

$$\overline{P}_r\left(r_0\right) = \left(\frac{cT_0}{2}\right)\left[\frac{P_t G_0^2}{\lambda^2\left(4\pi\right)^3}\right]\left[\frac{\pi\theta_1\phi_1}{8ln2}\right]\frac{\pi^5|K_w|^2 Z_e\left(r_0\right)}{r_0^2} \tag{2.10}$$

The CASA IP1 radars operate at an attenuating frequency, therefore the reflectivity needs to be corrected for this effect (Bringi and Chandrasekar, 2001). To correct for attenuation the CASA radars employ a self consistency method described in Bringi et al. (2001). In their method the attenuation effect is corrected for using the measured differential propagation phase ($\Phi_{dp}$). Figure 2.1 and 2.2 shows the attenuated and attenuation corrected reflectivity, respectively, observed on May 14, 2009 at 02:31:16 UTC by the Cyril radar .

During operations, the attenuation corrected reflectivity from each radar is used to generate a composite reflectivity field. A composite reflectivity field can be generated two ways. In both methods, the data is resampled from radar coordinates to a common Cartesian grid either in (lat, lon, alt) or (x,y,z), and the maximum reflectivity value in overlapping regions is taken. Where the two methods differ is how each altitude level is handled. In the first method, hence forth called the CSU composite, each altitude level is retained. The CSU composte is used for the composite reflectivity field used in the dual-Doppler retrievals. In the second method, hence forth called the WDSS-II composite, the three dimensional grid is projected onto a two dimensional grid. This is done by taking the maximum value in the vertical column and projecting it to two dimensions (Lakshmanan et al., 2007). This method is used to visualize CASA composite reflectivity images during real-time operations. Figure 2.3 shows an example of both methods. The left image is an example of the CSU composite. The figure shows the composite reflectivity at an altitude of 1 km. The right image is and example of the WDSS-II composite.

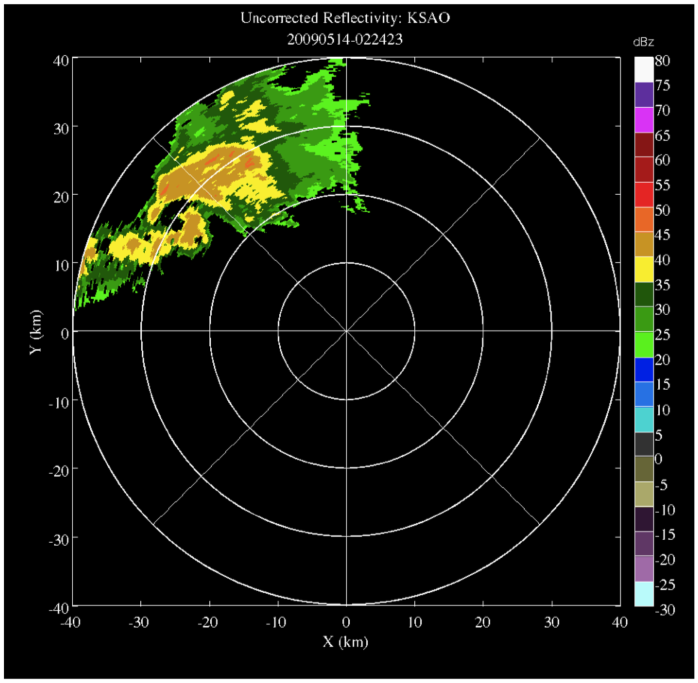

Figure 2.1: Uncorrected reflectivity observed on May 14, 2009 at 02:31:16 UTC by KCYR

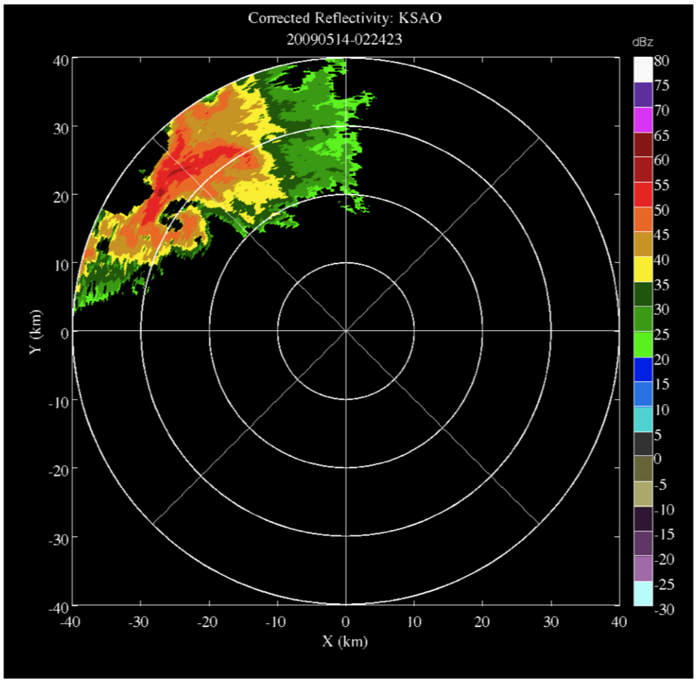

Figure 2.2: Corrected reflectivity observed on May 14, 2009 at 02:31:16 UTC by KCYR

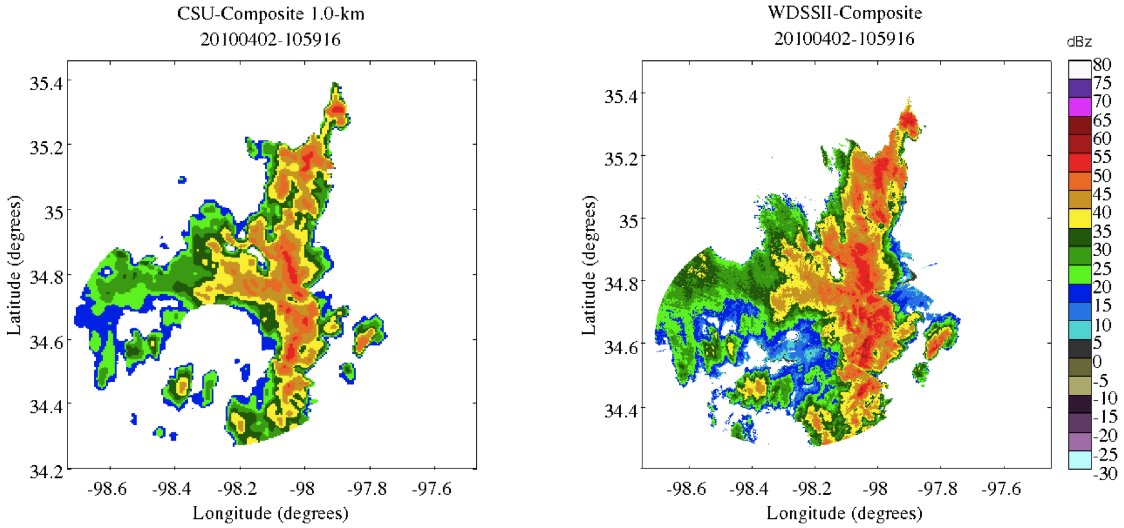

Figure 2.3: Composite reflectivity field observed on April 2, 2010 at 10:59:16 UTC

### 2.3.2 Velocity

A weather signal's power spectral density is a power weighted distribution of the scatterer's radial velocity. For a moving particle, the power spectrum, or Doppler spectrum, is a delta function located at $f = -2v/\lambda$. A scatterer that is moving away from the radar will have a positive velocity (negative frequency) and a scatterer that is moving towards the radar will have a negative velocity (positive frequency). In a volume of hydrometeors, the Doppler spectrum will be a superposition of the individual scatters, resulting in a continuous Doppler spectrum. Figure 2.4 shows an example Doppler spectrum for a simulated weather signal. Overall the power spectral density of a weather signal is not symmetric about $f = 0$, which results in a complex autocovariance function. The mean frequency, $\overline{f}$, of the power spectral density is the frequency where the spectrum is symmetric. The mean frequency is determined from the phase of the autocovariance function:

$$\overline{f} = \frac{arg\left[R\left(t\right)\right]}{2\pi t} \tag{2.11}$$

Where $arg$ is the argument of a complex number. Since the mean frequency is related to the Doppler shift, then the mean velocity is given as:

$$\overline{v} = \frac{-\lambda}{4\pi t} arg\left[R\left(t\right)\right] \tag{2.12}$$

Figure 2.5 shows and example velocity plot from the Cyril radar.

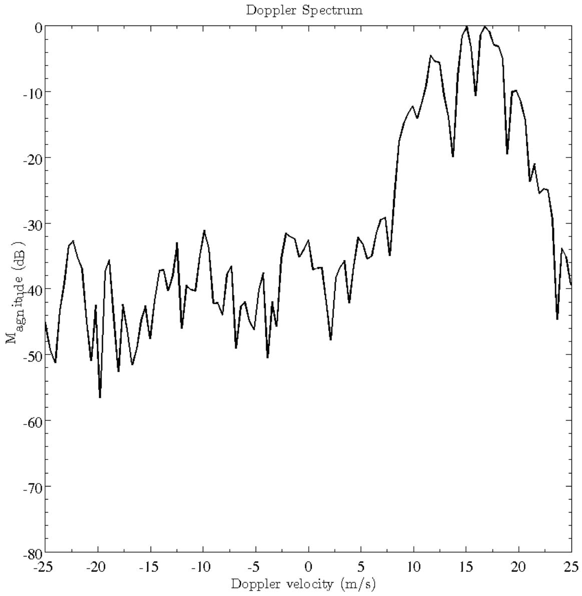

Figure 2.4: Doppler spectrum from simulated signal

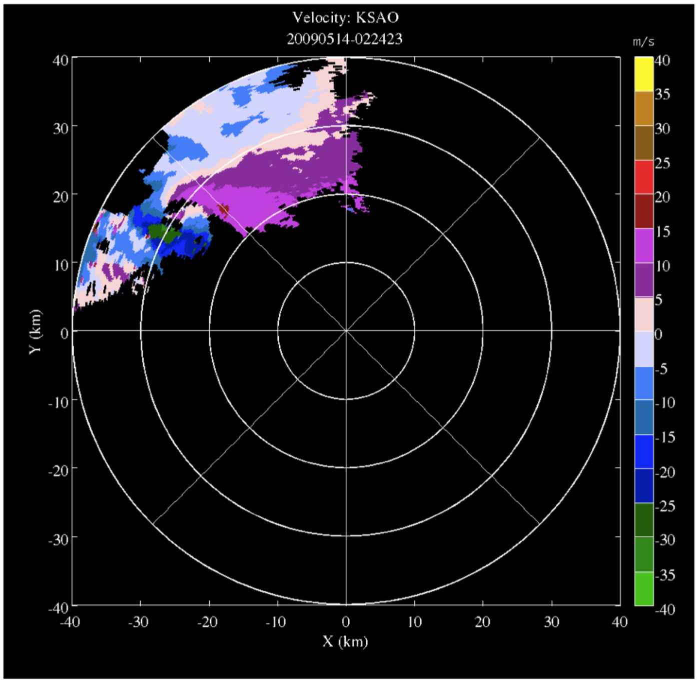

Figure 2.5: Radial velocity observed on May 14, 2009 at 02:31:16 UTC by KCYR

## 2.4 Summary

This chapter has described the CASA IP1 system and the relevant data fields need for dual-Doppler retrievals. A description of the CASA IP1 radars was given. The description focused on each major subsystem of the radar, transmitter, antenna, receiver, and data acquisition. A description of clutter remove was given along with a description of reflectivity and velocity fields. Example images of reflectivity and velocity where given. A description of composite reflectivity field generation was also provided, along with example images for the CSU composite and the WDSS-II composite.

# CHAPTER 3

# WIND FIELD RETRIEVALS

## 3.1 Introduction

Due to the overlapping coverage domains, the geometry of the IP1 radars is ideal for wind field retrievals. The retrieval process can be divided into two separate subsystems. The scan strategy and the retrieval. The scan strategy serves two roles. The first is that coordinated scanning minimizes the synchronization time between collected data. Making the data collected by all the radars as simultaneous as possible. The second is that the normalized standard deviation in the retrieval is minimized. The wind retrieval itself can be divided into two steps, resampling to a common three dimensional Cartesian grid and the wind retrieval. Resampling to a common Cartesian grid provides a way to convert data in radar coordinates to Cartesian coordinates. The common grid references the data from multiple radars to a coordinate system that is referenced to a single point. The retrieval process retrieves the three components of the air motion, u,v, and w. This chapter will describe the necessary theory for dual- and multi-Doppler retrievals. Section 3.2 will discuss techniques for resampling radar data to a common Cartesian grid. Section 3.3 will provide an overview of the theory for retrieving a three-dimensional wind field using both the dual- and multi-Doppler techniques. Section 3.4 will provide an error analysis , and section 3.5 will discuss the CASA IP1 real-time dual-Doppler system.

## 3.2 Resampling

Radar observations are not uniformly distributed in Cartesian space, therefore prior to retrieving the wind field, reflectivity and velocity measurements are interpolated to a three dimensional common Cartesian grid. Methods used for interpolation from radar space $(r, \theta, \phi)$ to Cartesian space $(x, y, z)$ are linear interpolation and distance-dependent weighed average (DDWA) interpolation schemes. In a linear interpolation procedure (Mohr and Vaughan, 1979), the six closest points (two in range, two in azimuth, and two in elevation) to the grid point are used in a bilinear interpolation procedure to estimate the radar measurement at that grid point. It has been noted in Trapp and Dowswell (2000) that bilinear and nearest-neighbor interpolation schemes tend to introduce noise into the interpolated field, and therefore will not be included in this discussion. In a DDWA interpolation scheme (Cressman, 1959; Barnes, 1964), points in radar space within a specified distance (radius of influence) from the grid point are used for estimating the value at the grid point. Figure 3.1 shows the concept of DDWA. In the figure the observations are represented by +, and the grid point is the star. The radius of influence is represented by the circle with radius R.

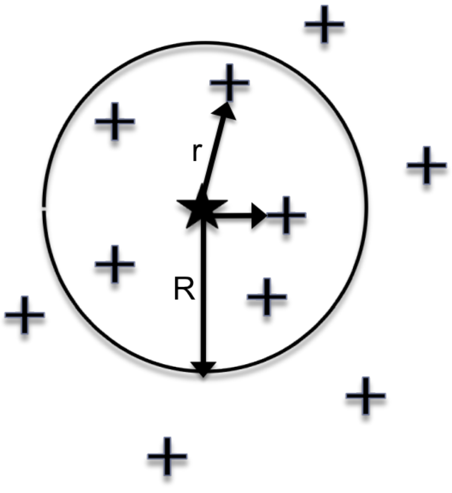

Figure 3.1: DDWA resampling scheme

For distance-weighting interpolation schemes the output grid point value at the point $(i, j, k)$ is calculated as

$$V_e(i,j,k) = V_g(i,j,k) + \frac{\sum_{m=1}^{M} w_m(V_{om} - V_{gm})}{\sum_{m=1}^{M} w_m} \tag{3.1}$$

Where $V_g$ is the value of a guess field at grid point $(i, j, k)$, $V_{om}$ is the observation at point $m$, $V_{gm}$ is the guess field value at point $m$, $w_m$ is the distance-dependent weight, and $M$ is the number of points within a specified radius of influence from the grid point $(i, j, k)$. When interpolating radar observations to a Cartesian grid, the point m is defined by the observation at point $(r, \theta, \phi)$. In many meteorological applications the guess field is a forecast of the field of interest. When interpolating reflectivity and velocity fields to a common Cartesian grid the guess fields are a zero fields.

The most common weighting function is the Cressman weight. The Cressman weighting function (Cressman, 1959) is given by:

$$w_m = \begin{cases} \dfrac{R^2 - r^2}{R^2 + r^2} & r < R \\ 0 & otherwise \end{cases} \tag{3.2}$$

Where R is the radius of influence, and r is the distance from the radar data point $(r, \theta, \phi)$ to the grid point $(i, j, k)$. Figure 3.2 shows the Cressman weight for four radii of influence, 0.5 kilometers, 1.0 kilometers, 1.5 kilometers, and 2.0 kilometers.

From equation 3.1 and 3.2 it is apparent that DDWA interpolation schemes effectively produce a filtered interpolated field. The filtering effects, described in Trapp and Dowswell (2000), are able to filter out undesired scales of motion (and in some cases desired scales of motion) from the observed field. In many cases the choice of radius of influence should not exceed the largest sampling interval found in any given direction (Carbone et al., 1985). Large radii of influence tend to produce an over smoothed interpolated field, whereas too small radii of influence tend to alias unresolved scales of motion.

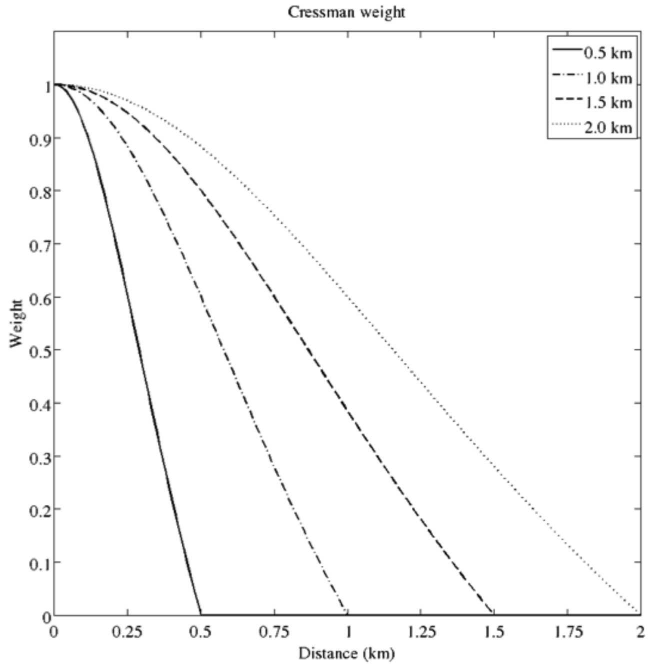

Figure 3.2: Cressmanwieght for varying radius of influence

## 3.3 Wind Retrievals

The theory for determining a three-dimensional wind field using two Doppler radars is described in Armijo (1969), and O'Brien (1970). Sections 3.3.1 and 3.3.2 will discuss the pertinent theory for three-dimensional wind field retrieval using two or more Doppler radars respectively.

### 3.3.1 Horizontal Retrievals

In the Cartesian coordinate system, a particle's motion can be expressed as $(u, v, w + V_t)$ where $u$ is the motion of the particle in the eastward direction, $v$ is the particle's motion in the northward direction, $w + V_t$ is the sum of the particle's motion in the vertical direction and the fall speed of the particle. The projection of the particles motion onto a Doppler radar's radial is:

$$v_r = usin\theta cos\phi + vcos\theta cos\phi + (w + V_t)sin\phi \tag{3.3}$$

Where $\theta$ and $\phi$ are the azimuth and elevation angles of the radar.

Consider two radars observing the same particle located at a point P(x, y, z), then the projection of the particle's motion at the two different beam angles forms a system of linear equations:

$$v_r^1 = usin\theta_1 cos\phi_1 + vcos\theta_1 cos\phi_1 + (w + V_t)sin\phi_1 \tag{3.4}$$

$$v_r^2 = usin\theta_2 cos\phi_2 + vcos\theta_2 cos\phi_2 + (w + V_t)sin\phi_2 \tag{3.5}$$

In matrix notation the linear system becomes:

$$\mathbf{v_r} = \mathbf{H} \left[ \begin{array}{ccc} u & v & w + V_t \end{array} \right]^T \tag{3.6}$$

$$\mathbf{v_r} = \left[ \begin{array}{cc} v_r^1 & v_r^2 \end{array} \right]^T \tag{3.7}$$

$$\mathbf{H} = \left[ \begin{array}{ccc} sin\theta_1 cos\phi_1 & cos\theta_1 sin\phi_1 & sin\phi_1 \\ sin\theta_2 cos\phi_2 & cos\theta_2 sin\phi_2 & sin\phi_2 \end{array} \right] \tag{3.8}$$

The above equations assume that the measurements made by the radars are made simultaneously. However, this is not practical since both radars will inevitably sample the same volume of space at slightly different times due to the different scan times. However, this assumption can be approximated during the interpolation from radar space to Cartesian space by using a space-time correction method, or advection. The method estimates a mean storm motion vector based on the movement of reflectivity cells in multiple radar scenes. The computed mean storm motion vector can then be used to advect locations of the data. Smaller time differences between radar collection time implies that less advection needs to be applied to the data. In the case of CASA the synchronization between radars is small enough the effect of advection is minimal (see Chapter 4).

The three-dimensional wind field can be solved for using a least-squares approach, which minimizes the error between the observed field and the synthesized field. Using this approach, the estimates of the wind field are derived as follows:

$$\begin{aligned} \bigtriangledown \left[ \left( \mathbf{v_r} - \mathbf{H}\mathbf{b}^T \right) \left( \mathbf{v_r} - \mathbf{H}\mathbf{b} \right) \right] &= 0 \\ = \bigtriangledown \left[ \mathbf{v_r}^T \mathbf{v_r}^T - \mathbf{v_r}^T \mathbf{H}\mathbf{b} - \mathbf{b}^T \mathbf{H}^T \mathbf{v_r} + \mathbf{b}^T \mathbf{H}^T \mathbf{H}\mathbf{b} \right] &= 0 \end{aligned} \tag{3.9}$$

Since ${\mathbf{v_r}}^T\mathbf{H}\mathbf{b} = \mathbf{b}^T\mathbf{H}^T\mathbf{v_r} = \left(\mathbf{H}^T{\mathbf{v_r}}^T\mathbf{b}\right)$ then the above equation reduces to

$$\bigtriangledown \left[{\mathbf{v_r}}^T\mathbf{v} - 2\left(\mathbf{H}^T\mathbf{v_r}\right)^T\mathbf{b} + \mathbf{b}^T\mathbf{H}^T\mathbf{H}\mathbf{b}\right] = 0 \tag{3.10}$$

Taking the gradient yields

$$-2\mathbf{H}^T\mathbf{v_r} + 2\mathbf{H}^T\mathbf{H}\mathbf{b} = 0 \tag{3.11}$$

solving for $\mathbf{b}$ gives the least squares estimate of the particles motion, thus

$$\hat{\mathbf{b}} = \left(\mathbf{H}^T\mathbf{H}\right)^{-1}\mathbf{H}^T\mathbf{v_r} \tag{3.12}$$

The vertical motion of the particle, w, can be solved for using the mass continuity equation (Armijo, 1969; Miller and Strauch, 1974). Methods for solving the mass continuity equation are given in section 3.3.2.

$$\frac{\partial(\rho u)}{\partial x} + \frac{\partial(\rho v)}{\partial y} + \frac{\partial(\rho w)}{\partial z} = 0 \tag{3.13}$$

Where $\rho$ is the air density. When using two radars, the system of equations is an under determined system, therefore the fall speed of the particle is assumed a priori from the reflectivity prior to solving for the vertical component of the particle's motion. Power law based reflectivity fall speed relations have been given by Atlas et al. (1973). By using the reflectivity fall speed relation the system reduces to three unknowns in three equations.

When using two radars to resolve the wind field, an initial estimate of the wind field is determined by omitting the component of vertical motion. Therefore, u and v can be solved from:

$$\left[\begin{array}{cc} u' & v' \end{array}\right] = \mathbf{H}^{-1}\mathbf{v_r} \tag{3.14}$$

Where it is assumed that $\mathbf{H}$ is invertible. The horizontal components of the wind field are then given by:

$$\left[\begin{array}{cc} u & v \end{array}\right]^T = \left[\begin{array}{cc} u' & v' \end{array}\right]^T + (w + V_t)\,\epsilon \tag{3.15}$$

Where $\epsilon$ is an error parameter. The mass continuity equation can then be used to solve for the vertical component of the particles motion. Methods for solving the mass continuity equation are given in section 3.3.2.

The above analysis can easily be extended to a radar network consisting of m radars. For m radars:

$$\mathbf{v_r} = \begin{bmatrix} v_r^1 & \cdots & v_r^m \end{bmatrix}^T \tag{3.16}$$

$$\mathbf{H} = \begin{bmatrix} sin\theta_1 cos\phi_1 & cos\theta_1 sin\phi_1 & sin\phi_1 \\ \vdots & \vdots & \vdots \\ sin\theta_m cos\phi_m & cos\theta_m sin\phi_m & sin\phi_m \end{bmatrix} \tag{3.17}$$

The components of the particles motion can be solved for using a generalized least-squares method. In a multi-Doppler method prior knowledge of the particle's fall speed is not needed and the estimates of u and v can be determined directly and then applied to the mass continuity equation.

### 3.3.2 Vertical Retrievals

The mass continuity equation is used to solve for the vertical component of a particle's motion. The vertical component can be retrieved using three different integration methods, upward integration, downward integration, and a variational integration method. Although the vertical component is not solved for in the CASA Dual-Doppler System (see Chapter 4) a review of vertical air motion retrieval is given in order to complete the theory associated with the wind retrievals.

In an upward integration method, w is solved for by setting the boundary condition at the ground to zero, and integrating in the upward direction. A boundary condition of zero is chosen at the ground because it is assumed that the air motion is minimal at the Earths surface. The upward integration method is prone to several errors (Ray et al., 1980; Bohn and Srivastava, 1975). One problem associated with the upward integration method is that any error associated with setting the boundary condition are amplified in the integration causing the errors at the top of the storm to be unreasonably large. This effect is present in the integration method because the boundary condition is selected in a region where the air density is at its maximum. Thus the upward integration method is unsuitable for retrieving any kinematic information beyond a few kilometers (Matejka and Bartles, 1998).

In a downward integration method, w is solved for by setting a boundary condition at the top of the storm to zero, and then integrating in a downward direction A boundary condition of zero is selected at the storm top, since it is assumed that there is none to little air motion at the top of the storm. When compared to the upward integration method, downward integration produces more accurate estimates of w (Ray et al., 1980; Bohn and Srivastava, 1975). The improved estimates are associated with the selection of the boundary condition. Unlike the upward integration method, the downward method sets the boundary condition where air density is low causing errors in boundary condition selection to have a less of an effect on the estimate of w. The integration method tends to dampen any errors, which more then compensates for an error in setting the upper boundary condition. The downward method is the most widely used integration method.

In the variational method introduced by O'Brien (1970), w is solved for by setting the boundary conditions at the ground and storm top to zero and then integrating twice. The first integration is in the upward direction and the second is in the downward direction. The variational method distributes the errors associated with the upward integration, during the downward portion, which reduces the effect of errors from the upward integration. Since a boundary condition at the ground and storm needs to be set, this not a preferred integration method because of the difficulty in setting a boundary condition at the ground.

## 3.4 Error Analysis

From the discussion in section 3.3.1 it is apparent that the dual- and multi-Doppler retrieval technique is a linear transformation that converts observations in a nonorthogonal vector space to an orthogonal vector space. Due to the transformation, the error variances in the retrieved wind field generally exceed that of the measured radial velocities (Miller and Strauch, 1974). The covariance of the wind retrieval is given as

$$\begin{aligned} cov\left[\begin{array}{ccc} u & v & w+V_t \end{array}\right] &= cov\left(\left(\mathbf{H}^T\mathbf{H}\right)^{-1}\mathbf{H}^T\mathbf{v_r}\right) \\ &= E\left[\left(\left(\mathbf{H}^T\mathbf{H}\right)^{-1}\mathbf{H}^T\mathbf{v_r}\right)\left(\left(\mathbf{H}^T\mathbf{H}\right)^{-1}\mathbf{H}^T\mathbf{v_r}\right)^T\right] \end{aligned} \tag{3.18}$$

Performing the matrix multiplication and simplifying yields

$$\left(\mathbf{H}^T\mathbf{H}\right)^{-1}\mathbf{H}^T E\left[v_r v_r^T\right]\mathbf{H}\left(\mathbf{H}^T\mathbf{H}\right)^T \tag{3.19}$$

It can be assumed that the variances in the measured radial velocities are independent (Bringi and Chandrasekar, 2001) end equal (for the case of the CASA radars), therefore the variance in the multi-Doppler retrieval can be normalized as:

$$\frac{tr\left(cov\left[\begin{array}{ccc} u & v & w+V_t \end{array}\right]\right)}{3var\left(v_r^1\right)} = tr\left(\mathbf{H}^T\mathbf{H}\right)^{-T} \tag{3.20}$$

For a network of two radars the normalized variance reduces to:

$$\frac{\sigma_u^2+\sigma_v^2}{2\sigma_{v_r}^2} = csc^2\beta\frac{cos^2\phi_1+cos^2\phi_2}{2cos^2\phi_1 cos^2\phi_2} \tag{3.21}$$

Where $\sigma_u^2$ and $\sigma_v^2$ are the variances in eastwardly and northwardly components of the wind vector, and $\sigma_{v_r}^2$ is the variance in the radial velocity estimate. The angle $\beta$ is the beam crossing angle. From the above equation it is apparent that the normalized variance for dual-Doppler wind estimates are dependent on elevation angle. This fact will be used to establish a scan strategy for the IP1 network. At low elevation angles ($\geq 10\,^\circ$) the effects of the vertical component of motion are negligible (Given and Ray, 1994). For low elevations and a network of two radars the normalized variance reduces to

$$\frac{\sigma_u^2+\sigma_v^2}{2\sigma_{v_r}^2} = csc^2\beta \tag{3.22}$$

It is clear that the error variance in the dual-Doppler technique is related to the geometry of the network (Davies-Jones, 1979). Figure 3.3 shows the dual-Doppler coverage as a function of beam crossing angle for two arbitrary radars located at (-15, 0) and (15, 0), the maximum range for both radars is 40 km. Figure 3.4 shows the geometry of the two radars. Figure 3.3 demonstrates the spatial dependence of the beam crossing angle or variance in the wind vector estimates. As the beam crossing angle increases the error variance in the retrieval decreases, and as the angle decreases the error variance becomes infinitely large. Figure 3.5 shows the standard deviation in the retrieval as a function of beam crossing for an elevation of zero degrees. For small beam crossing angles the radial velocities measured by both radars are nearly equal in magnitude but opposite in direction, thus no new information about the direction of the wind perpendicular to the radial is add. Therefore, the wind vector should not be retrieved near the baseline (the line connecting the two radars in figure 3.4 ). It has been shown in Davies-Jones (1979) that beam crossing angles greater then or equal to $30^\circ$ are adequate for wind vector retrievals.

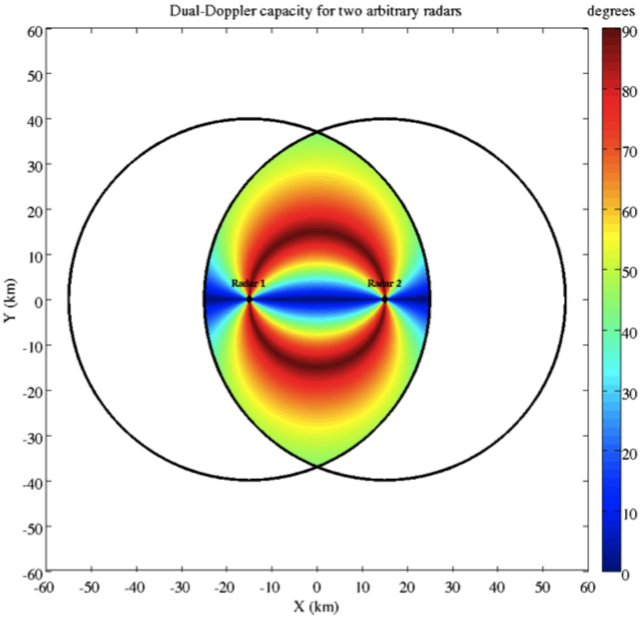

Figure 3.3: Dual-Doppler coverage as a function of beam crossing angle for two arbitrary radars

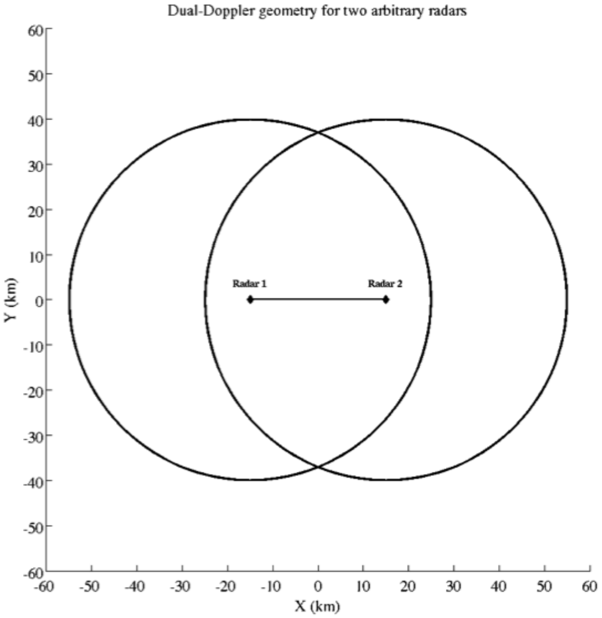

Figure 3.4: Geometry of network formed by two arbitrary radars

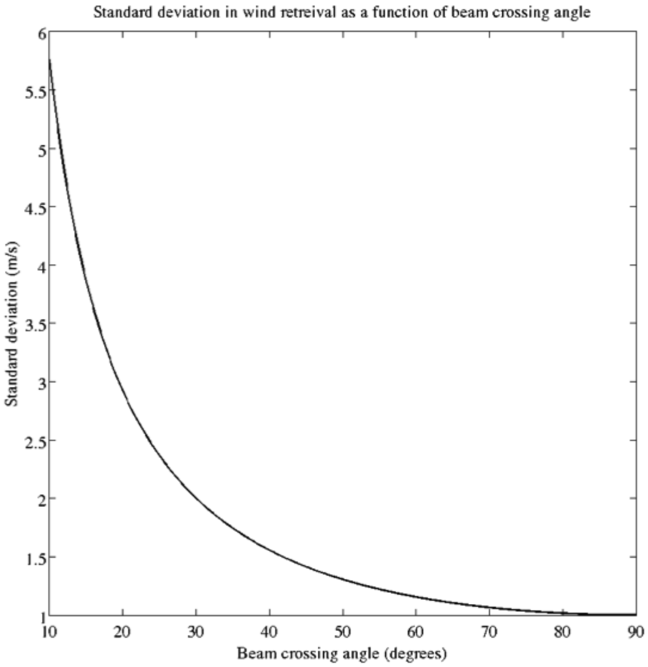

Figure 3.5: Standard deviation in wind estimate versus beam crossing angle

## 3.5 IP1 Real-time Dual-Doppler System

The real-time dual-Doppler system for IP1 (see figure 3.6) is composed of two subsystems, the scan strategy optimization subsystem and the retrieval subsystem. The scan strategy subsystem is part of the MCC, and determines the optimal beam crossing angles and dual-Doppler pairs given the location of weather echoes within the network. The retrieval subsystem combines the incoming sector scans from the individual radars into volumes, re-samples the attenuation corrected reflectivity and radial velocity data from the individual radars onto a three dimensional Cartesian grid, and then retrieves the components of the horizontal wind field to generate a composite wind field for the IP1 network (Chandrasekar et al., 2010a)

### 3.5.1 IP1 Dual-Doppler Coverage

The topology of the IP1 network (see figure 3.7) is such that multiple candidate pairs for dual-Doppler and multi-Doppler retrievals exist. The total number of dual-

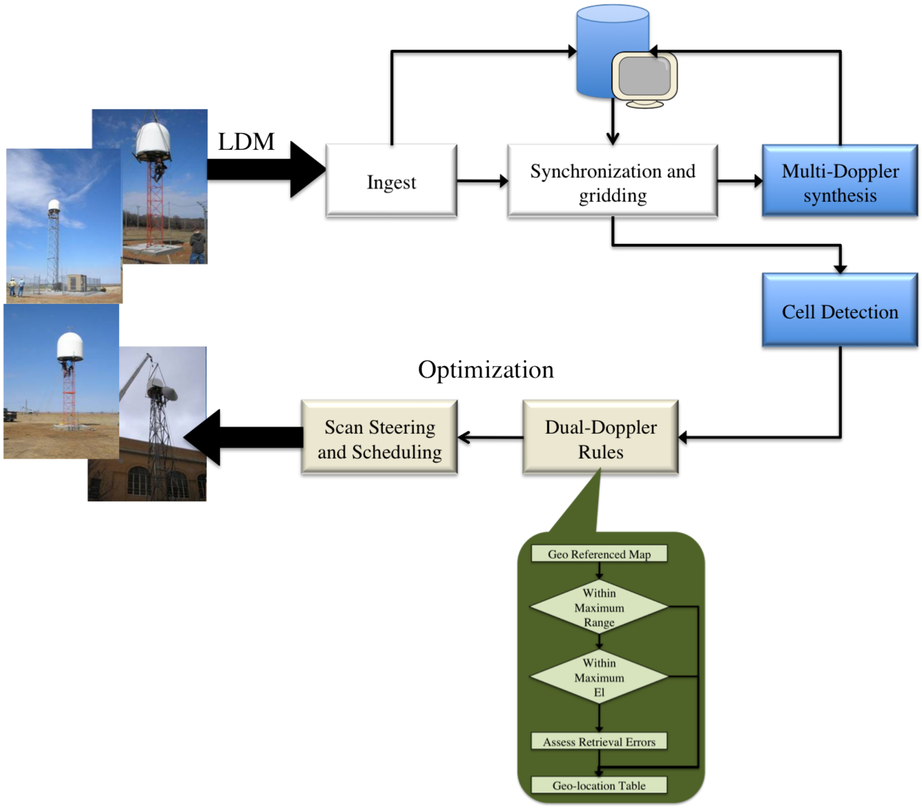

Figure 3.6: Block diagram of CASA dual-Doppler system

, triple-, and quad-Doppler pairs within the network can be determined by using combinations where arrangement is not a concern. For a network of n radars with overlapping coverage the number of pairs in network for wind retrievals is given by $\binom{n}{k}$, where n is the number of radars and k is the desired level of radar coverage domain overlap. Therefore, within the network there are $\binom{4}{2} = 6$ dual-Doppler pairs, $\binom{4}{3} = 4$ triple-Doppler regions, and $\binom{4}{4} = 1$ quad-Doppler region. The six dual-Doppler pairs within the network are formed by KCYR and KSAO, KCYR and KRSP, KCYR and KLWE, KRSP and KSAO, KRSP and KLWE, and KSAO and KLWE. Figures 3.8, 3.10, 3.12 3.14, 3.16, and 3.18 show each dual-Doppler pairs location within the network, and figures 3.9, 3.11, 3.13, 3.15, 3.17, and 3.19 show the dual-Doppler coverage as a function of beam crossing angle for each pair.

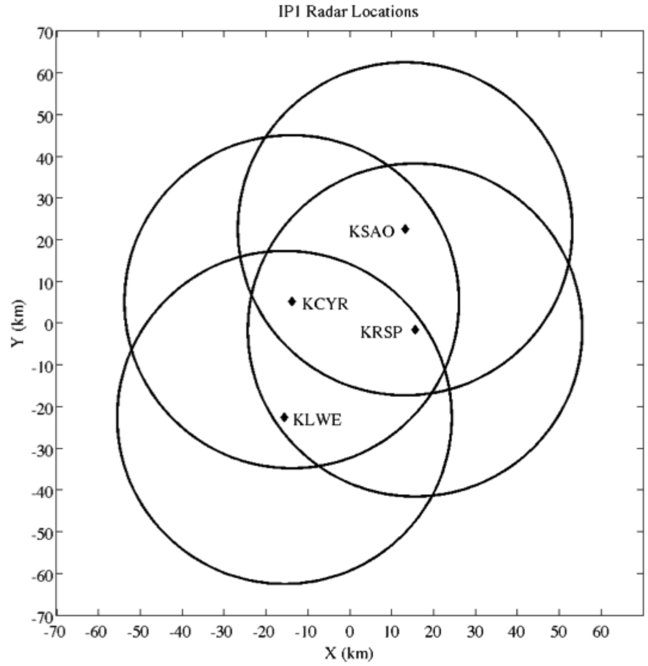

Figure 3.7: Topology of IP1 network

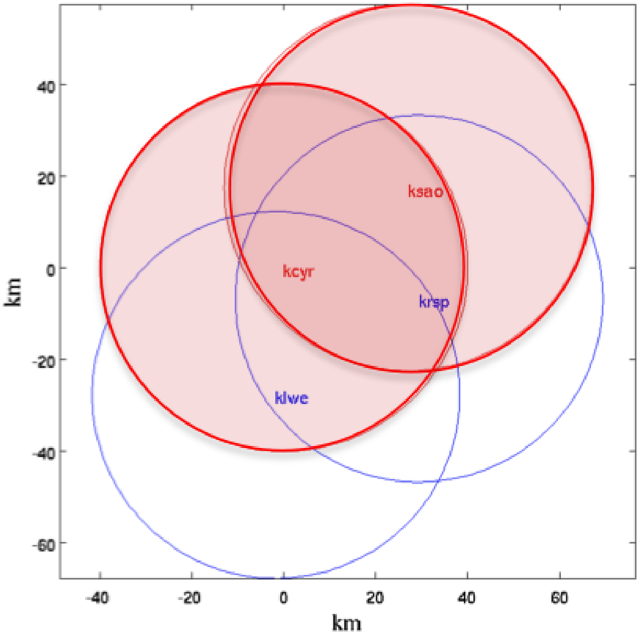

Figure 3.8: Location of (KCYR, KSAO) in IP1 network

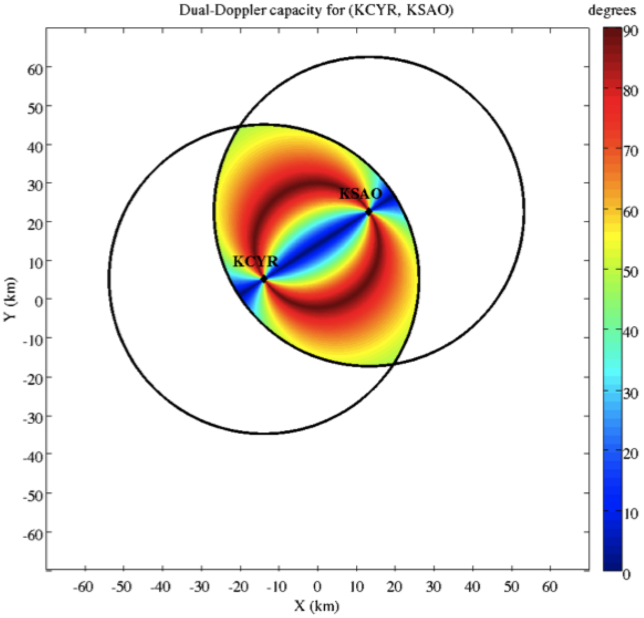

Figure 3.9: Dual-Doppler coverage as a function of beam crossing angle for (KCYR, KSAO)

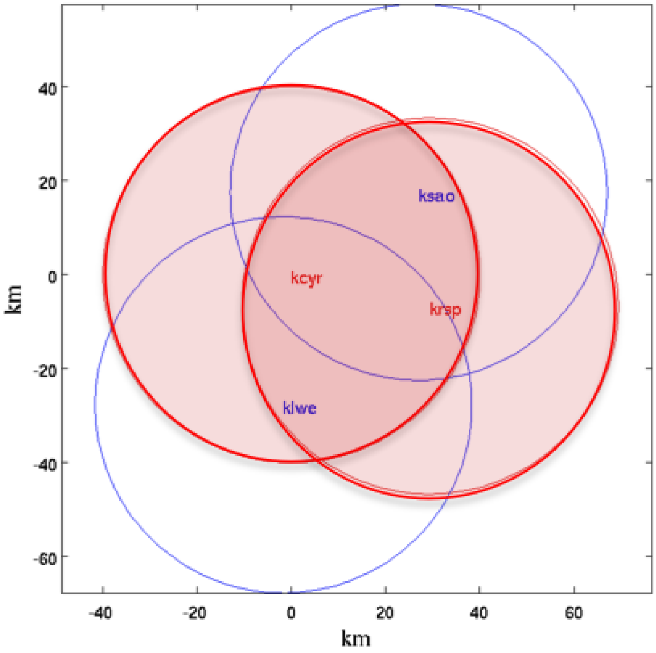

Figure 3.10: Location of (KCYR, KRSP) in IP1 network

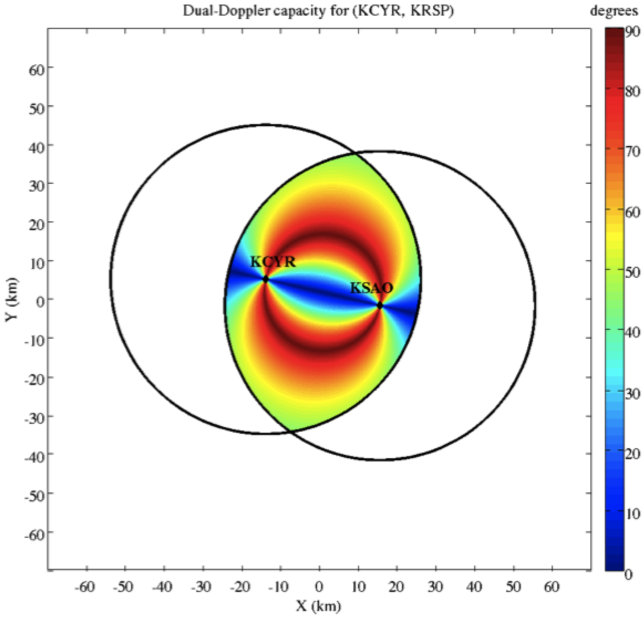

Figure 3.11: Dual-Doppler coverage as a function of beam crossing angle for (KCYR, KRSP)

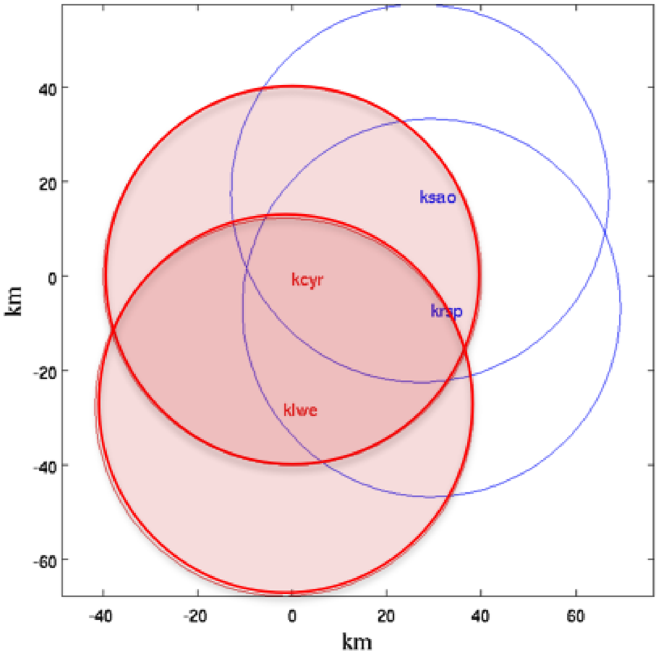

Figure 3.12: Location of (KCYR, KLWE) in IP1 network

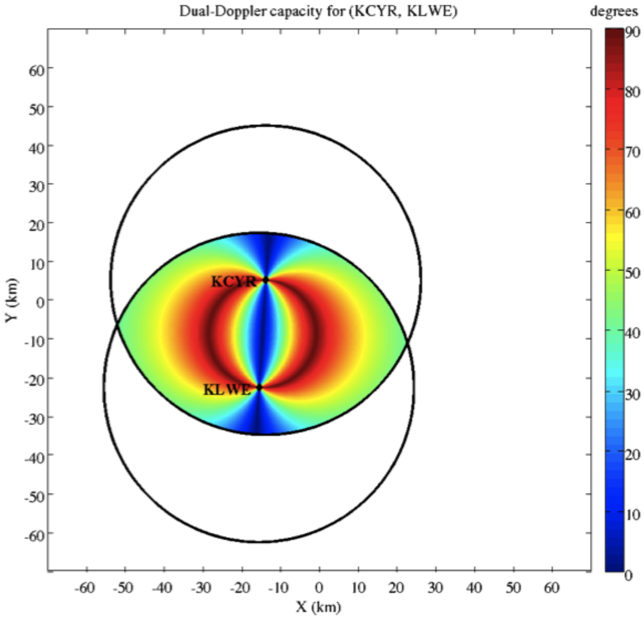

Figure 3.13: Dual-Doppler coverage as a function of beam crossing angle for (KCYR, KLWE)

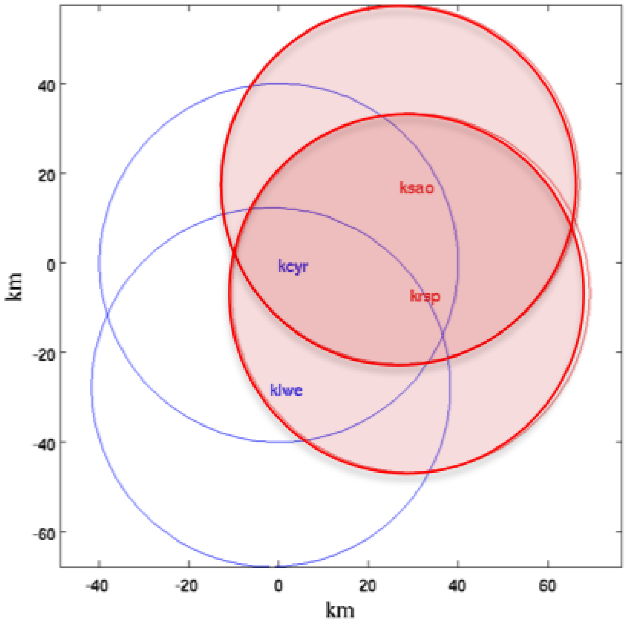

Figure 3.14: Location of (KRSP, KSAO) in IP1 network

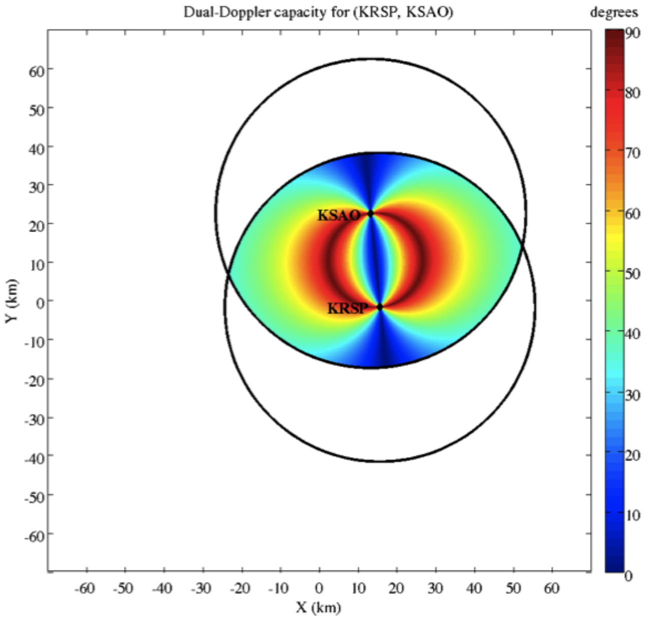

Figure 3.15: Dual-Doppler coverage as a function of beam crossing angle for (KRSP, KSAO)

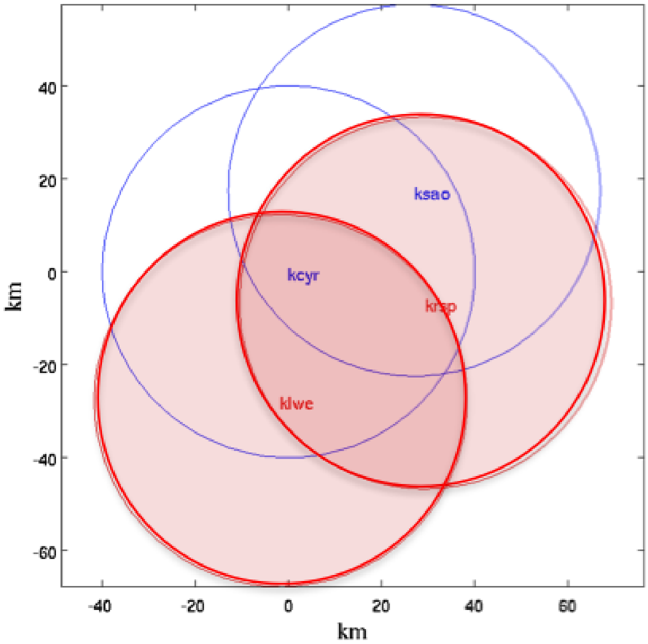

Figure 3.16: Location of (KRSP, KLWE) in IP1 network

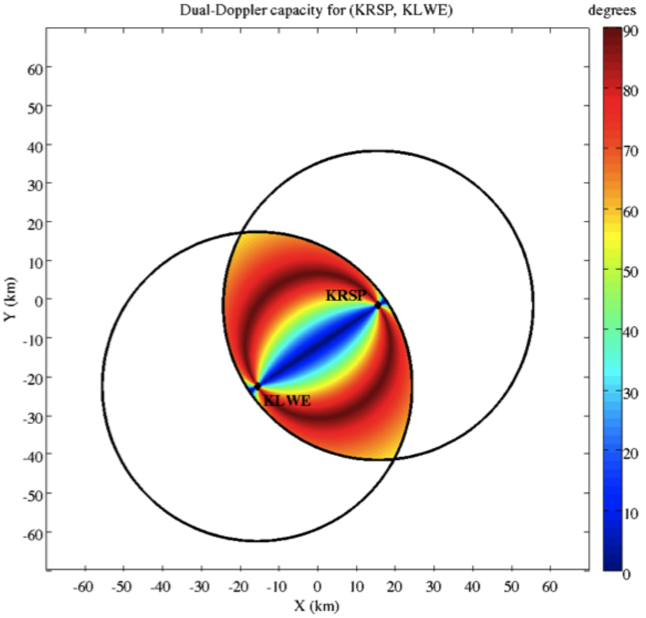

Figure 3.17: Dual-Doppler coverage as a function of beam crossing angle for (KRSP, KLWE)

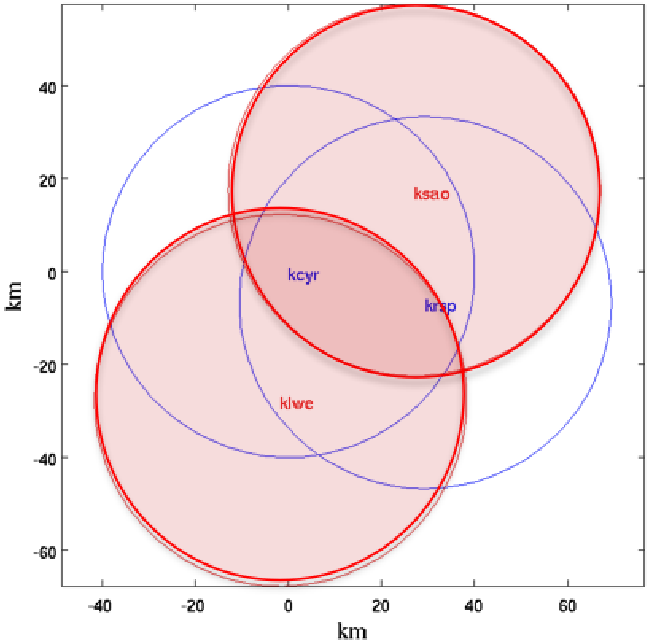

Figure 3.18: Location of (KSAO, KLWE) in IP1 network

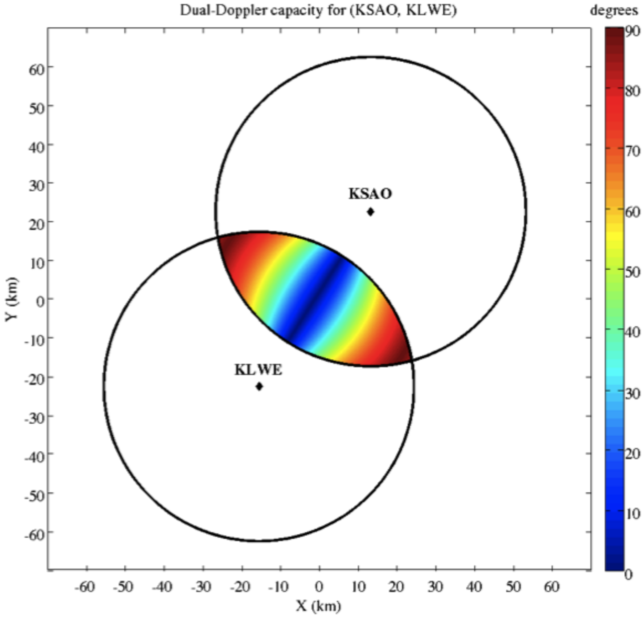

Figure 3.19: Dual-Doppler coverage as a function of beam crossing angle for (KSAO, KLWE)

### 3.5.2 Scan Strategy Optimization

Within much of the IP1 network multiple dual-Doppler pairs exist. From figure 3.21 it is apparent that the dual-Doppler regions intertwine throughout the network. Therefore, the dual-Doppler system uses a scan strategy optimizer to determine the best dual-Doppler pair for a given storm location. Since the IP1 radars are mechanically scanned, the beam steering limitation of the radars is used as a constraint in the optimization, therefore the optimization is performed at the maximum altitude. The scan strategy can be determined by minimizing the error variance, at the maximum altitude. Nevertheless, other factors need to also be considered in the optimization. For instance, during the scan strategy optimization, radar scans at higher elevation angles are less preferred because of the longer time required to steer the beam. This places higher preference on radar pairs that have lower elevation angles at long ranges. However, the beam resolution worsens in proportion of $r^2$, and the signal strength at the antenna port decreases in the order of $r^2$ (Wang et al., 2008). Therefore the objective function is defined as (Wang et al., 2008):

$$F = \frac{\sigma_u^2 + \sigma_v^2}{2\sigma_{v_r}^2} + \left( \frac{max\left(\theta_1, \theta_2\right)}{\theta_{max}} \right)^2 + \left( \frac{max\left(r_1, r_2\right)}{r_{max}} \right)^2 \tag{3.23}$$

where $\theta_{max}$ is the maximum elevation angle and $r_{max}$ is the maximum range. The zones of the best dual-Doppler regions at an altitude of 5km are given in figure 3.20. Figure 3.21 shows the dual-Doppler coverage as a function of beam crossing angle for the IP1 network. For real-time operations a lookup table of geo-located dual-Doppler zones is used in conjunction with storm detection and other rules and constraints, i.e., end user requirements, to determine the best dual-Doppler scan (Wang et al., 2008). During operations the MCC outputs a set of convex polygons that are provided to the dual-Doppler scan optimizer. During the real-time operations the MCC generates contours from the composite reflectivity. The contours are outlines of different reflectivity values starting at 30 dBz and ending at 60 dBz in 10 dBz increments. The 30 dBz contours are then used to create a convex polygon. Figure 3.22 shows a convex polygon overlaid on to reflectivity data observed on May 28, 2008 at 10:48 UTC. The convex polygons are used in the optimization to determine the best dual-Doppler scan in real-time.

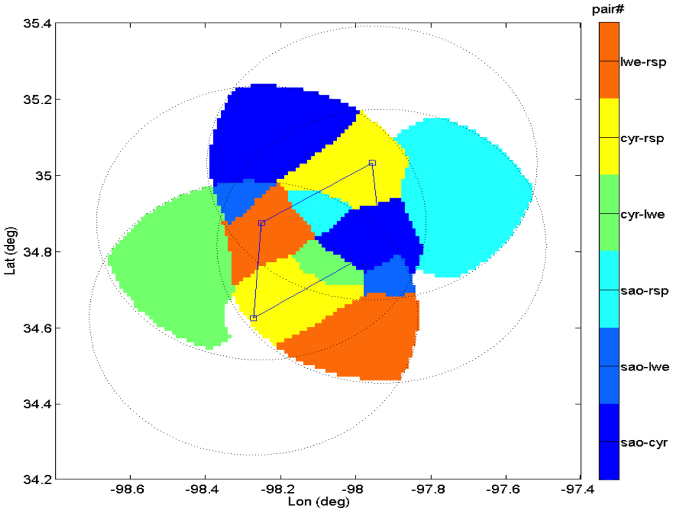

Figure 3.20: Zones for best dual-Doppler pairs for the IP1 network

### 3.5.3 Real-time Dual-Doppler Retrievals

The real-time dual-Doppler retrieval subsystem is interfaced with the IP1 closed loop through a Local Data Manager (LDM). The LDM is an event-driven distribution software that streams netCDF files containing moment data from the four radars to the SOCC where the real-time wind field retrievals are performed. The event driven nature of the LDM enables the processing and storage of moment data in real-time. Once moment data is received at the SOCC, it is ingested into the system, and volume lists are created which enable volume based processing. In volume based processing, the retrieval algorithm processes the entire set of PPI scans for an individual radar.

Once a volume of data is received at the SOCC, the real-time retrieval subsystem re-samples the reflectivity and velocity data from the individual radars onto a common three dimensional Cartesian grid. The grid is centered at (34.8276 ° N, 98.1007 ° W, 0.0 m) where the grid center point is given as (latitude, longitude, altitude). The

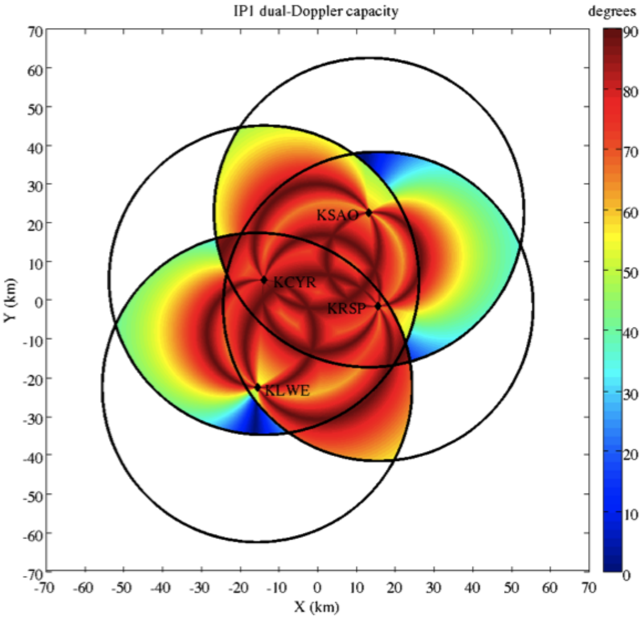

Figure 3.21: Dual-Doppler coverage as a function of beam crossing angle for the IP1 network

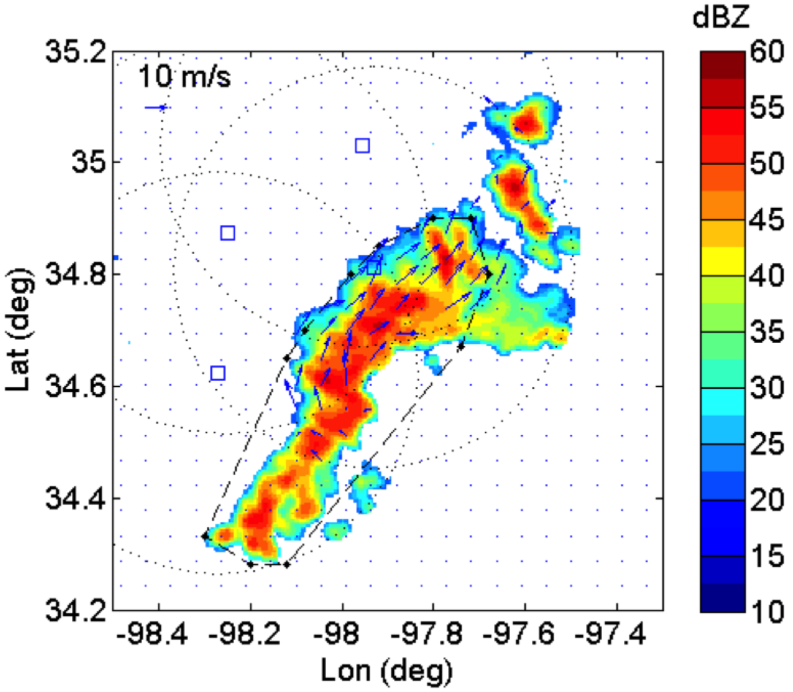

Figure 3.22: Example convex polygon. From Wang et al. (2008)

center point corresponds to the origin (0, 0, 0) in a three dimensional Cartesian coordinate system. The common grid extends from -70 to 70 km in the E-W direction, -70 to 70 km in the N-S direction, and 0.5 to 10 km (sea level) in the vertical direction. The resolution of the common Cartesian grid is 0.5 km in the x, y, and z directions. A denser resolution is not used because of the increased computational complexity associated with the increased resolution. The reflectivity and velocity estimates at the grid point are determined using a Cressman weighting function that has a radius of influence no greater then 1 kilometer.

Once the data is re-sampled onto a common Cartesian grid the wind retrieval is performed. During the wind retrieval step, the components of the air motion are retrieved and a reflectivity composite is generated. The composite reflectivity field is generated by taking the maximum reflectivity value in the regions where there is overlapping coverage. For the IP1 radars the vertical component of air motion is not retrieved since on average the maximum elevation is less then $10^\circ$. However, some system wide scan strategies, such as CLASSIC, do warrant the need for retrieving the vertical component of the air motion due to the higher elevation angles in the scanning set. The u and v components of the air motion are retrieved using the method described in section 3.3.1. The wind retrieval is done using all incoming data and multi-Doppler radar sets as well as dual-Doppler pairs are considered (Chandrasekar et al., 2010a). Due to computational requirements during real-time operations, it is not possible to perform dual-Doppler retrievals on all six pairs within the required system heartbeat. However, the retrieval software handles both dual- and multi-Doppler regions of IP1 network separately.

Once the u and v components are retrieved, the results are quality controlled. The u and v components are first quality controlled on beam crossing angle. Therefore, any point that is in a region where the beam crossing angle is less then $30^\circ$ is masked as a bad point. This corresponds to points where $\sqrt{\sigma_u^2 + \sigma_v^2} \leq 2.83$. The second quality control method checks for outliers using a local de-spiking routine. For each u and v grid point the routine takes the mean all the points within 2 grid points of the value. If the value deviates by more then 7.5 standard deviations from the mean or there are fewer then four good points in vicinity of the value, then the value is masked as a bad point. Both u and v need to be good for that grid point to be considered good. If either u or v are bad then the point is masked as bad point. After the retrieval the values of u, v, $\sigma_v$, $\sigma_u$, and the reflectivity composite are stored in a netCDF file. The file is is archived and sent to an external display. Figure 3.23 shows processes involved in the real-time retrieval subsystem. Figure 3.24 shows the process of retrieving the horizontal wind field. Figure 3.25 shows an example wind field from an EF2 tornado observed by the IP1 network on May 14, 2009.

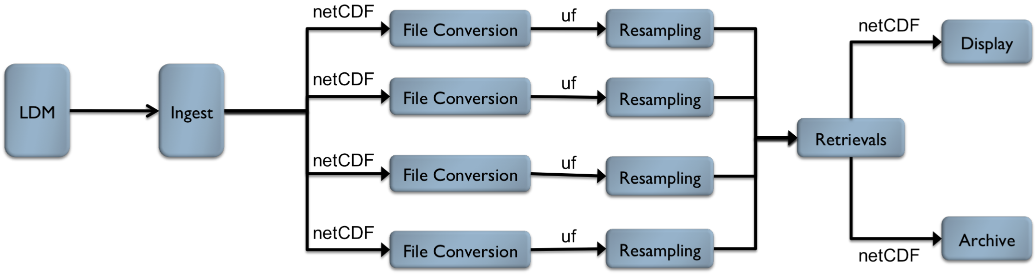

Figure 3.23: Block diagram of real-time retrieval subsystem

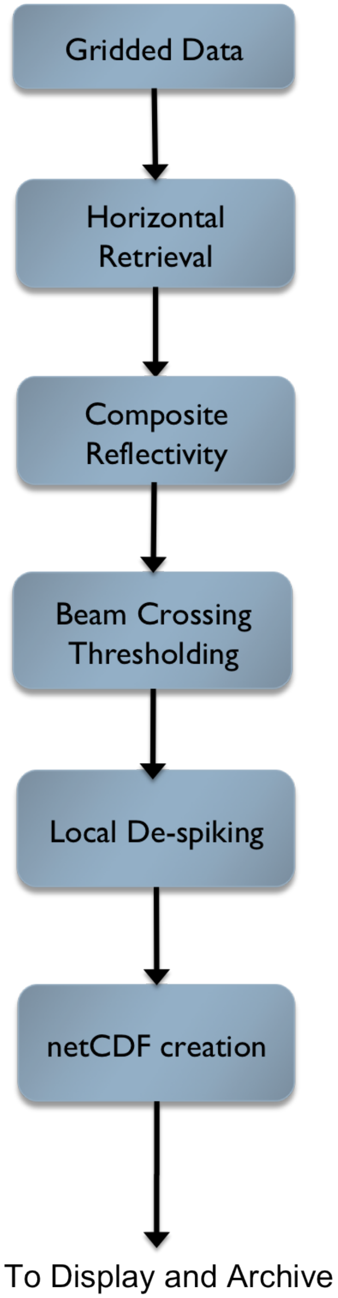

Figure 3.24: Block diagram of real-time retrieval

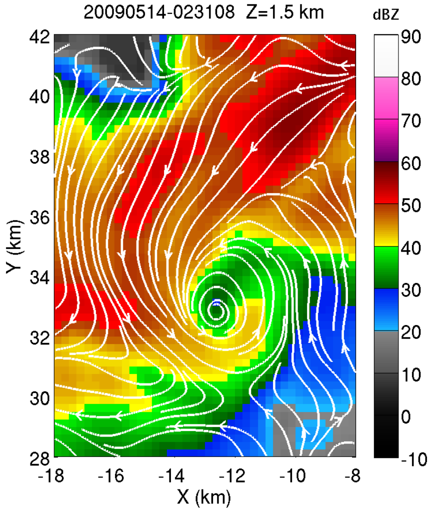

Figure 3.25: Example dual-Doppler retrieval

## 3.6 summary

This chapter described the necessary theory for the retrieval of three dimensional wind fields and also provided a description of the CASA dual-Doppler system. The resampling process to a common Cartesian grid was discussed, and weighting functions used in the resmapling process were provided. The theory needed for retrieving the horizontal and vertical components of the wind field was also discussed. The discussion covered methods for retrieving the horizontal component of the wind field using two Doppler radars, and a more general case with $m$ Doppler radars was provided. Various methods of vertical integration for the retrieval of the vertical component of air motion were discussed and the advantages of each methods were also given. A detailed error analysis was given for both cases of two Doppler radars and $m$ Doppler radars. The description of the CASA dual-Doppler system discussed the dual-Doppler coverage in the IP1 network, and each subsystem, scan strategy and retrieval, were described.

# CHAPTER 4

# EVALUATION OF THE CASA DUAL-DOPPLER SYSTEM

## 4.1 Introduction

During the spring of each year between 2006 and 2010 the IP1 radars were operational from March until June, called the IP1 spring experiment. The spring experiment provides an opportunity to test new real-time products, the functionality of the system, and to experiment with new scan strategies. For the 2009 spring experiment 13 storm events where observed by the IP1 network starting on February 10, 2009 and ending on May 23, 2009. During the 2009 spring experiment the CASA dual-Doppler product was in its testing phase. While in the testing phase statistics on scan strategy, and the retrievals where collected. Data on the dual-Doppler scan strategy was logged by the MCC in real-time. For each dual-Doppler pair in the IP1 network the MCC logged data on beam crossing angle, number of elevation angles, maximum elevation/tilt angle, maximum measured observation altitude, and synchronization time between the radars in a pair. The data logged by the MCC will be used to assess the performance of the dual-Doppler scan strategy. For the wind field retrievals the normalized standard deviation was computed for each valid grid point in the retrieved field. The normalized standard deviation will be used to determine the quality of the wind field retrieval. The resulting wind field can then be used to compute other fields such as vorticity and divergence. This chapter will discuss the evaluation and applications of the CASA dual-Doppler system. Section 4.2 will provide an evaluation of the dual-Doppler scan strategy used in the CASA dual-Doppler system for the 2009 spring experiment and provide a case study of the scan strategy's performance for a severe thunderstorm observed by the IP1 network on April 2, 2010. Section 4.3 will provide an evaluation of the dual-Doppler retrievals for the spring 2009 experiment and provide a case study for an EF-2 tornado that was observed by the IP1 network on May 14, 2009. Section 4.4 will provide some applications of the dual-Doppler system, including visualization of dual-Doppler data using streamlines and arrows, and the computation of vorticity and divergence.

## 4.2 Evaluation of Dual-Doppler Scan Strategy

The performance of the dual-Doppler scan strategy was assessed using the 13 storm events making up the 2009 spring experiment. Also a case study for a storm event occuring on April 2, 2010 is used to evaluate the performance of the dual-Doppler scan strategy when there is significant attenuation in the dual-Doppler regions. The April 2, 2010 storm event was a severe thunderstorm that had noticeable circulation features in the dual-Doppler regions formed by KRSP and KSAO, KRSP and KLWE, and KRSP and KCYR. The event also had significant attenuation in the dual-Doppler regions formed by KRSP and KLWE, and KSAO and KLWE. Section 4.2.1 will give an evaluation of the scan strategy performance during the 2009 spring experiment, and section 4.2.2 will provide an evaluation for the event occurring on April 2, 2010.

### 4.2.1 2009 Spring Experiment

Six parameters were used to evaluate the performance of the dual-Doppler scan strategy. These parameters are 1) the number of pairs tasked per system heartbeat, 2) maximum and minimum beam-crossing angle, 3) maximum elevation/tilt angle, 4) number of elevation angles, 5) maximum measured observation altitude above ground level, and 6) time synchronization. The number of pairs per heartbeat gives insight into the level of dual-Doppler coverage for each event. The maximum and minimum beam crossing angle determines the quality of the dual-Doppler data from each scan.

The maximum and minimum beam crossing angle can be used to determine the expected upper and lower bounds on the error in horizontal wind field retrieval. The number of elevation angles, maximum elevation/tilt angle, and maximum observation altitude provide an objective measure that determines the possiblity of retrieving the vertical component of the wind field. The synchronization time between radars in each pair indicates how well matched in time the data from each radar is. The synchronization time also gives a measurement of the amount of advection that needs to be applied to the collected data.

For the 13 weather events that make up the spring 2009 experiment 12 were available for analysis for the pairs formed by KCYR and KSAO, KCYR and KRSP, and KCYR and KLWE, due to KCYR being non-operational on April 30th, 2009. This section will use the data logged by the MCC for the 13 events to analyze the performance of the dual-Doppler scan strategy as a whole. Section 4.2.1.1 will assess the dual-Doppler coverage for each heartbeat, section 4.2.1.2 will evaluate the minimum and maximum beam crossing angle for each pair, section 4.2.1.3 will evaluate the vertical coverage in the dual-Doppler regions, and section 4.2.1.4 will analyze the time synchronization between each radar in a pair.

#### 4.2.1.1 Number of Pairs Tasks per Heartbeat

For the 13 events that make up the 2009 spring experiment the dual-Doppler coverage per heartbeat was assessed. For each heartbeat upto six pairs can be tasked for dual-Doppler. Figure 4.1 shows a bar chart for the total number pairs tasked per heartbeat, and table 4.1 summarizes the statistics for the plot. The event on April 30, 2009 only had a maximum of three possible pairs since KCYR was not operational at that time. The rest of the events had a maximum of six possible pairs that could be tasked during a heartbeat. Of the 13 events 53.85% had a mean number of pairs tasked between 2 and 3 pairs. 30.77% of the events had a mean number of pairs tasked greater than 3, and 15.38% of the events had a mean number of pairs tasked less than 2. The standard deviations for the events remained relatively the same for the 13 events, between slightly less than one and two pairs. The April 30, 2009 event had a the minimum standard deviation, 0.9143 pairs, while February 10, 2009 had the maximum standard deviation, 1.9932 pairs. Since the standard deviations remain between slightly less than one and two pairs, the number of pairs tasked during a given event does have some variation throughout the life of the event. This variation is expected since different stages of an event's life will have a varied degree of dual-Doppler coverage. At the beginning and end of an event's life, the event has the minimum possible dual-Doppler coverage. This occurs because the event is localized to the outer regions of the IP1 network where there is little to no dual-Doppler coverage. In the middle stage of the event's life there is more dual-Doppler coverage as the event is in the domain of multiple radars. This results in an increase of coverage in overlapping regions.

For the 13 cases occurring during the 2009 spring experiment, the dual-Doppler scan strategy provided sufficient dual-Doppler coverage of the events. Most of the events had at mean of 2 or more pairs covering the event. This indicates that in a DCAS environment the dual-Doppler scan strategy is able to provide continuous dual-Doppler coverage throughout the life of an event. Being able to provide continuous dual-Doppler coverage is important to end users, since the dual-Doppler product gives added information about low-level vector winds in severe weather events. The dual-Doppler scan strategy was able to succeed at providing continuous dual-Doppler coverage.

#### 4.2.1.2 Maximum and Minimum Beam Crossing Angle and Error Bounds

A single sector scan contains a range of beam crossing angles between 0 ° and 90 °. In a single scan the beam crossing angles can be described by the minimum (or worst) and the maximum (or best) beam crossing angle. Knowing the optimal and least optimal beam crossing angles in a scan gives an indication of how usable the

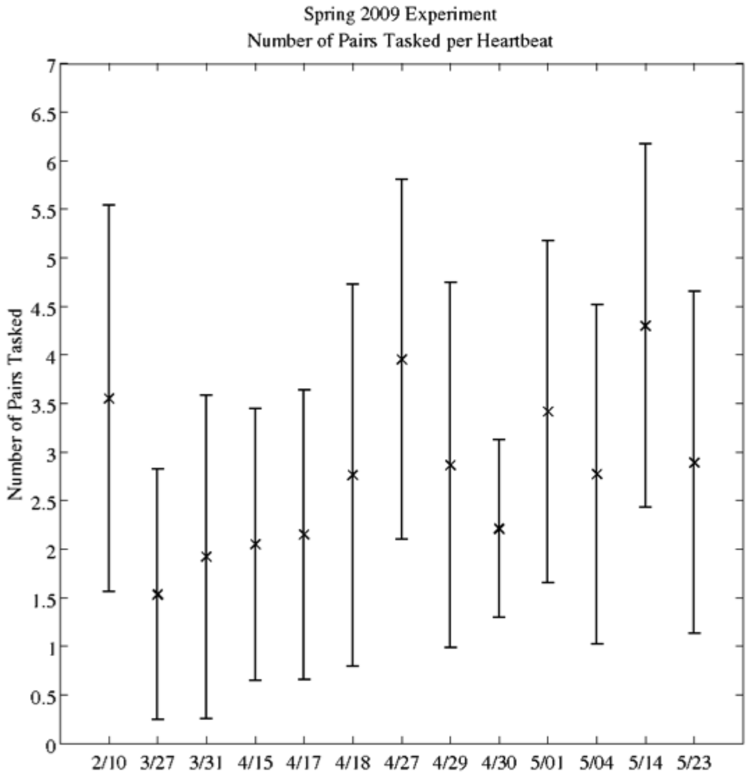

Figure 4.1: Bar chart of the number of pairs tasked per heartbeat.

Table 4.1: Statistics for the number of pairs tasked per heartbeat

| Date | Mean | std | Minimum | Maximum |
|---|---|---|---|---|
| 02/10/2009 | 3.6 | 2.0 | 1.0 | 6.0 |
| 03/27/2009 | 1.5 | 1.3 | 1.0 | 6.0 |
| 03/31/2009 | 1.9 | 1.7 | 1.0 | 6.0 |
| 04/15/2009 | 2.0 | 1.4 | 1.0 | 6.0 |
| 04/17/2009 | 2.1 | 1.5 | 1.0 | 6.0 |
| 04/18/2009 | 2.8 | 2.0 | 1.0 | 6.0 |
| 04/27/2009 | 4.0 | 1.9 | 1.0 | 6.0 |
| 04/29/2009 | 2.9 | 1.9 | 1.0 | 6.0 |
| 04/30/2009 | 2.2 | 0.9 | 1.0 | 3.0 |
| 05/01/2009 | 3.4 | 1.8 | 1.0 | 6.0 |
| 05/04/2009 | 2.8 | 1.7 | 1.0 | 6.0 |
| 05/14/2009 | 4.3 | 1.9 | 1.0 | 6.0 |
| 05/23/2009 | 2.9 | 1.8 | 1.0 | 6.0 |

data is for wind field retrievals. The beam crossing measurement is produced by the MCC during real-time operations. Bar charts for all six pairs are given in figures 4.2 - 4.7 and tables 4.2 - 4.7 summarize the statistics for each plot.

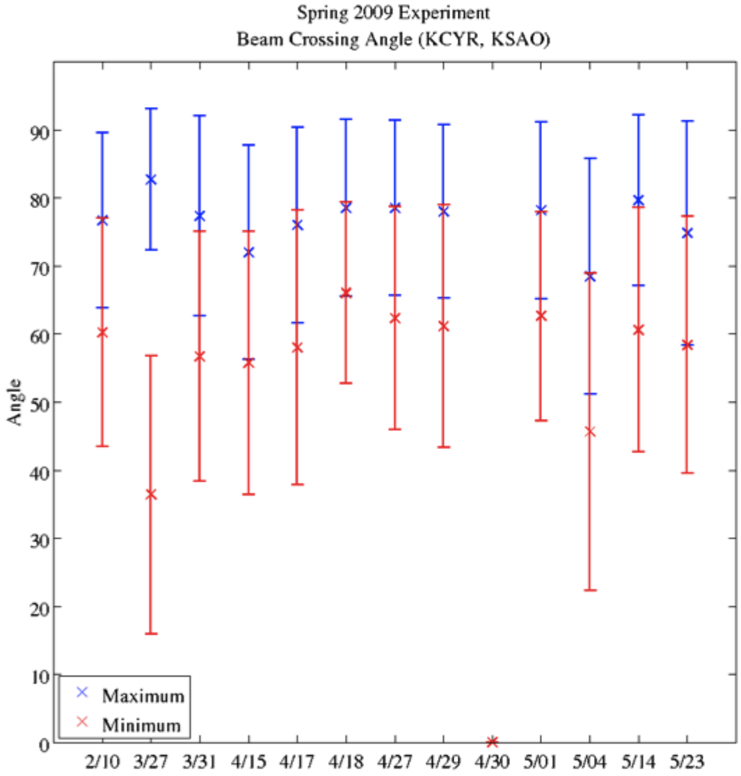

Figure 4.2: Bar chart of the best and worst beam crossing angles for (KCYR, KSAO).

The given results in figures 4.2 - 4.7 indicate that for the 2009 spring experiment the data collected using coordinated scanning is on average above the 30° threshold needed for accurate dual-Doppler retrievals. The scan strategy optimization does a satisfactory job of maintaining scans that consist of beam crossing angles between 30° and 90°. For any given event the scan strategy will be able to optimize the best beam crossing angles that maximize the quality of the data needed for dual-Doppler retrievals.

From the beam crossing angles the expected lower and upper bounds on the normalized standard deviation can be determined. The lower and upper bounds on the

Table 4.2: Statistics for minimum and maximum beam crossing angles for (KCYR, KSAO)

| Date | Mean (°) | | std (°) | | Minimum (°) | | Maximum (°) | |
|---|---|---|---|---|---|---|---|---|
| | Best | Worst | Best | Worst | Best | Worst | Best | Worst |
| 02/10/2009 | 76.7 | 60.2 | 12.9 | 16.8 | 31.3 | 0.3 | 90.0 | 84.9 |
| 03/27/2009 | 82.7 | 36.4 | 10.4 | 20.5 | 44.1 | 0.1 | 90.0 | 79.7 |
| 03/31/2009 | 77.4 | 56.8 | 14.7 | 18.3 | 24.5 | 0.3 | 90.0 | 81.5 |
| 04/15/2009 | 72.0 | 55.7 | 15.8 | 19.4 | 28.4 | 1.4 | 90.0 | 84.3 |
| 04/17/2009 | 76.0 | 58.0 | 14.3 | 20.2 | 30.3 | 6.8 | 90.0 | 84.3 |
| 04/18/2009 | 78.6 | 66.0 | 13.0 | 13.3 | 51.0 | 6.5 | 90.0 | 83.7 |
| 04/27/2009 | 78.6 | 62.4 | 12.9 | 16.4 | 17.8 | 0.3 | 90.0 | 83.2 |
| 04/29/2009 | 78.0 | 61.2 | 12.8 | 17.8 | 33.9 | 0.2 | 90.0 | 83.7 |
| 04/30/2009 | NA | NA | NA | NA | NA | NA | NA | NA |
| 05/01/2009 | 78.2 | 62.7 | 13.0 | 15.4 | 22.8 | 0.5 | 90.0 | 84.3 |
| 05/04/2009 | 68.4 | 45.6 | 17.3 | 23.3 | 23.1 | 0.2 | 90.0 | 76.2 |
| 05/14/2009 | 79.7 | 60.6 | 12.5 | 17.9 | 16.8 | 0.1 | 90.0 | 84.3 |
| 05/23/2009 | 74.9 | 58.4 | 16.5 | 18.9 | 23.3 | 0.1 | 90.0 | 81.9 |

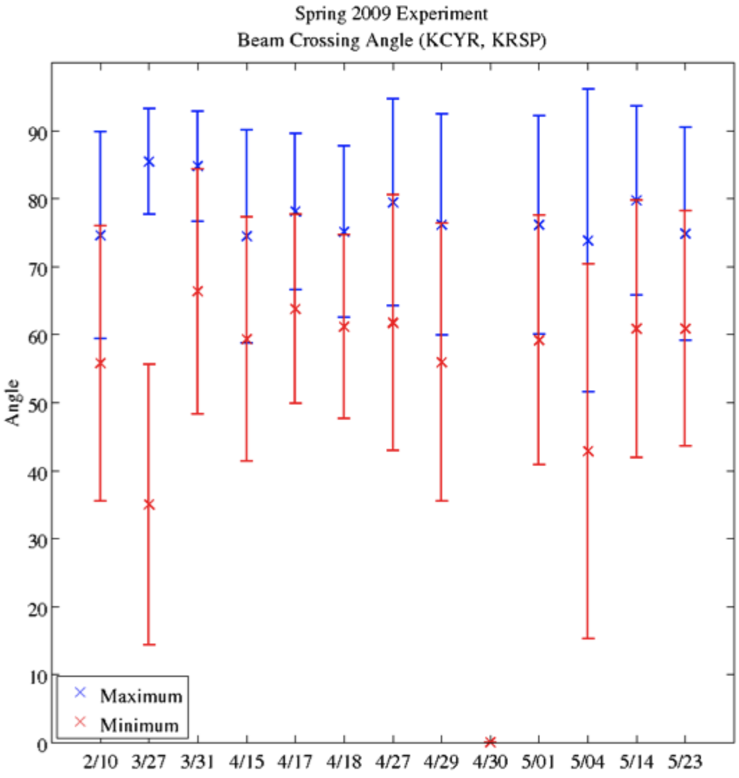

Figure 4.3: Bar chart of the minimum and maximum beam crossing angles for (KCYR, KRSP).

Table 4.3: Statistics for minimum and maximum beam crossing angles for (KCYR, KRSP)

| Date | Mean (°) | | std (°) | | Minimum (°) | | Maximum (°) | |
|---|---|---|---|---|---|---|---|---|
| | Best | Worst | Best | Worst | Best | Worst | Best | Worst |
| 02/10/2009 | 74.7 | 55.8 | 15.3 | 20.3 | 17.1 | 0.0 | 90.0 | 84.3 |
| 03/27/2009 | 85.5 | 35.0 | 7.8 | 20.7 | 53.9 | 0.1 | 90.0 | 70.2 |
| 03/31/2009 | 84.8 | 66.4 | 8.1 | 18.0 | 62.9 | 4.0 | 90.0 | 83.2 |
| 04/15/2009 | 74.5 | 59.4 | 15.7 | 18.0 | 16.3 | 1.8 | 90.0 | 82.3 |
| 04/17/2009 | 78.1 | 63.8 | 11.5 | 13.9 | 52.4 | 13.8 | 90.0 | 82.3 |
| 04/18/2009 | 75.1 | 61.2 | 12.6 | 13.5 | 47.2 | 25.9 | 90.0 | 82.7 |
| 04/27/2009 | 79.5 | 61.7 | 15.2 | 18.8 | 27.9 | 2.8 | 90.0 | 81.9 |
| 04/29/2009 | 76.2 | 55.9 | 16.3 | 20.5 | 13.9 | 0.0 | 90.0 | 82.7 |
| 04/30/2009 | NA | NA | NA | NA | NA | NA | NA | NA |
| 05/01/2009 | 76.2 | 59.2 | 16.0 | 18.4 | 11.9 | 0.1 | 90.0 | 82.7 |
| 05/04/2009 | 73.8 | 42.8 | 22.2 | 27.6 | 9.3 | 0.2 | 90.0 | 82.7 |
| 05/14/2009 | 79.7 | 60.9 | 14.0 | 18.9 | 24.5 | 0.7 | 90.0 | 83.2 |
| 05/23/2009 | 74.8 | 60.9 | 15.7 | 17.3 | 14.5 | 0.2 | 90.0 | 82.7 |

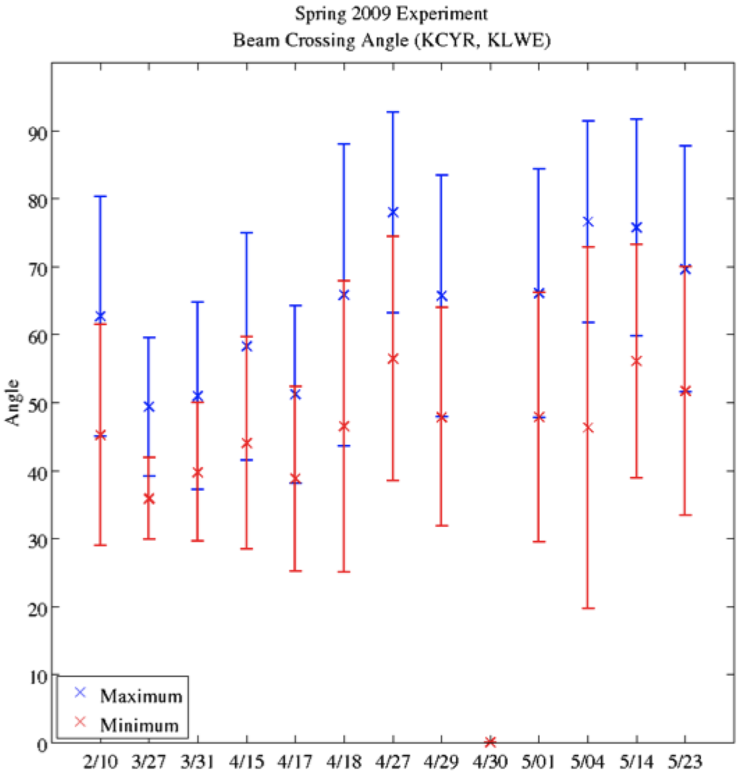

Figure 4.4: Bar chart of the minimal and maximum beam crossing angles for (KCYR, KLEW).

Table 4.4: Statistics for minimum and maximum beam crossing angles for (KCYR, KLWE)

| Date | Mean (°) | | std (°) | | Minimum (°) | | Maximum (°) | |
|---|---|---|---|---|---|---|---|---|
| | Best | Worst | Best | Worst | Best | Worst | Best | Worst |
| 02/10/2009 | 62.7 | 45.2 | 17.6 | 16.3 | 21.7 | 0.2 | 90.0 | 82.3 |
| 03/27/2009 | 49.4 | 35.9 | 10.2 | 6.0 | 42.0 | 0.2 | 90.0 | 72.7 |
| 03/31/2009 | 51.0 | 39.8 | 13.8 | 10.2 | 29.1 | 5.5 | 90.0 | 80.8 |
| 04/15/2009 | 58.3 | 44.0 | 16.7 | 15.6 | 11.2 | 0.3 | 90.0 | 79.1 |
| 04/17/2009 | 51.2 | 38.8 | 13.1 | 13.6 | 11.2 | 0.3 | 70.2 | 57.1 |
| 04/18/2009 | 65.8 | 46.5 | 22.2 | 21.5 | 31.3 | 10.5 | 90.0 | 73.5 |
| 04/27/2009 | 78.0 | 56.5 | 14.7 | 18.0 | 39.0 | 0.9 | 90.0 | 80.8 |
| 04/29/2009 | 65.7 | 47.9 | 17.7 | 16.1 | 10.3 | 1.1 | 90.0 | 79.4 |
| 04/30/2009 | NA | NA | NA | NA | NA | NA | NA | NA |
| 05/01/2009 | 66.1 | 47.9 | 18.3 | 18.4 | 16.7 | 0.1 | 90.0 | 80.8 |
| 05/04/2009 | 76.6 | 46.3 | 14.9 | 26.6 | 39.1 | 0.1 | 90.0 | 79.1 |
| 05/14/2009 | 75.8 | 56.1 | 15.9 | 17.2 | 29.7 | 1.0 | 90.0 | 80.8 |
| 05/23/2009 | 69.7 | 51.7 | 18.1 | 18.3 | 14.4 | 0.3 | 90.0 | 80.8 |

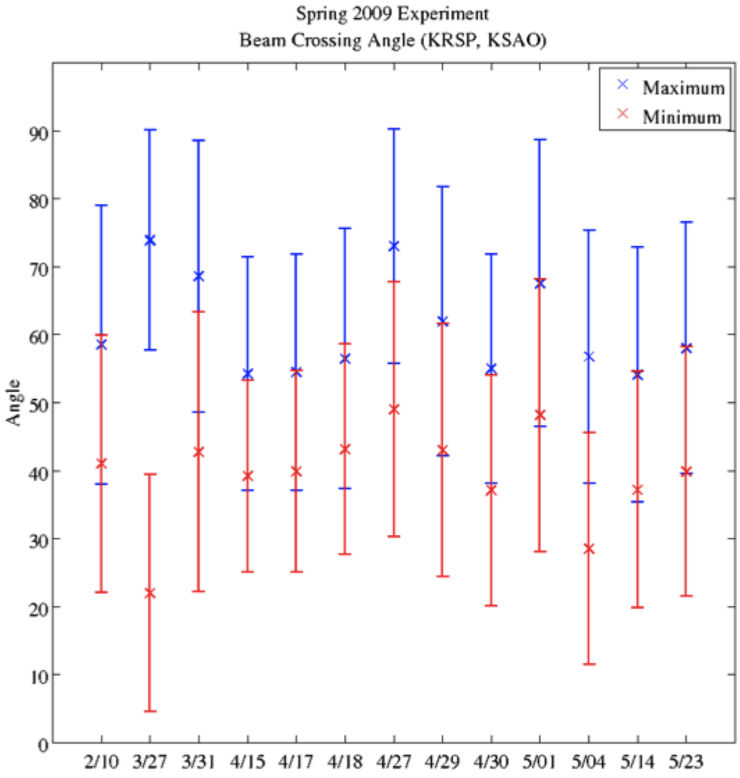

Figure 4.5: Bar chart of the minimum and maximum beam crossing angles for (KRSP, KSAO).

Table 4.5: Statistics for minimum and maximum beam crossing angles for (KRSP, KSAO)

| Date | Mean (°) | | std (°) | | Minimum (°) | | Maximum (°) | |
|---|---|---|---|---|---|---|---|---|
| | Best | Worst | Best | Worst | Best | Worst | Best | Worst |
| 02/10/2009 | 58.5 | 41.0 | 20.5 | 19.0 | 8.8 | 0.1 | 90.0 | 81.5 |
| 03/27/2009 | 73.9 | 22.0 | 16.2 | 17.5 | 37.2 | 0.1 | 90.0 | 66.2 |
| 03/31/2009 | 68.6 | 42.7 | 20.0 | 20.6 | 32.9 | 0.3 | 90.0 | 79.1 |
| 04/15/2009 | 54.2 | 39.2 | 17.2 | 14.1 | 12.5 | 0.1 | 90.0 | 70.9 |
| 04/17/2009 | 54.4 | 39.9 | 17.3 | 14.8 | 12.5 | 0.1 | 90.0 | 70.9 |
| 04/18/2009 | 56.5 | 43.2 | 19.2 | 15.5 | 35.4 | 20.1 | 90.0 | 79.1 |
| 04/27/2009 | 73.0 | 49.0 | 17.2 | 18.7 | 28.0 | 0.1 | 90.0 | 79.4 |
| 04/29/2009 | 62.0 | 43.0 | 19.8 | 18.6 | 8.8 | 0.5 | 90.0 | 78.8 |
| 04/30/2009 | 55.0 | 37.0 | 16.8 | 17.0 | 32.3 | 0.0 | 90.0 | 78.5 |
| 05/01/2009 | 67.6 | 48.2 | 21.2 | 20.0 | 6.3 | 0.1 | 90.0 | 79.7 |
| 05/04/2009 | 56.8 | 28.5 | 18.6 | 17.0 | 23.9 | 0.2 | 90.0 | 72.7 |
| 05/14/2009 | 54.1 | 37.2 | 18.8 | 17.4 | 8.6 | 0.2 | 90.0 | 78.5 |
| 05/23/2009 | 58.0 | 39.9 | 18.5 | 18.4 | 12.4 | 0.0 | 90.0 | 78.5 |

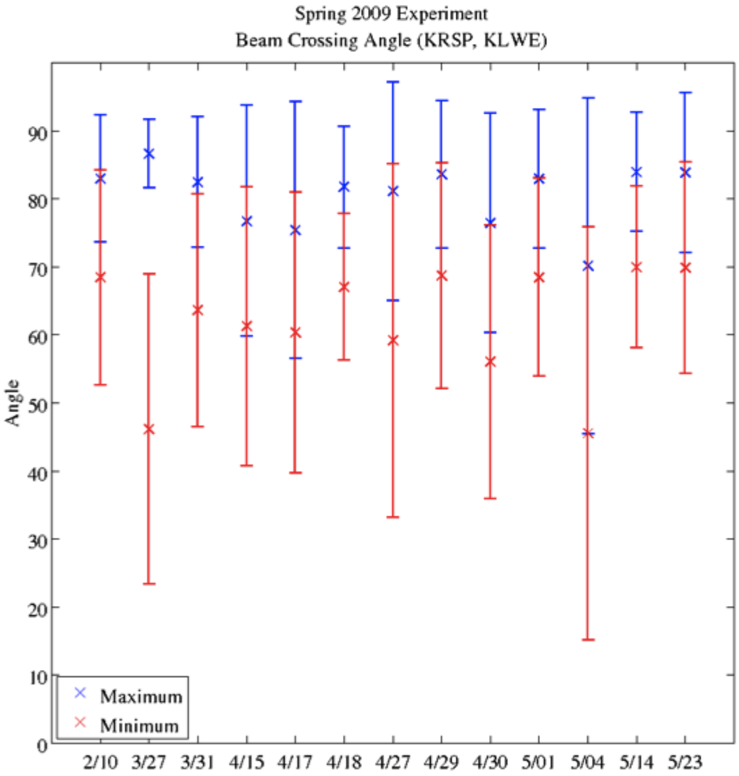

Figure 4.6: Bar chart of the minimum and maximum beam crossing angles for (KRSP, KLWE).

Table 4.6: Statistics for minimum and maximum beam crossing angles for (KRSP, KLWE)

| Date | Mean (°) |  | std (°) |  | Minimum (°) |  | Maximum (°) |  |
|---|---|---|---|---|---|---|---|---|
|  | Best | Worst | Best | Worst | Best | Worst | Best | Worst |
| 02/10/2009 | 83.0 | 68.5 | 9.3 | 15.8 | 23.3 | 0.6 | 90.0 | 85.6 |
| 03/27/2009 | 86.6 | 46.1 | 5.0 | 22.8 | 74.4 | 0.1 | 90.0 | 75.7 |
| 03/31/2009 | 82.5 | 63.6 | 9.6 | 17.1 | 46.6 | 18.5 | 90.0 | 84.3 |
| 04/15/2009 | 76.8 | 61.3 | 17.0 | 20.5 | 15.0 | 0.3 | 90.0 | 83.7 |
| 04/17/2009 | 75.4 | 60.3 | 18.9 | 20.6 | 15.0 | 0.3 | 90.0 | 83.2 |
| 04/18/2009 | 81.8 | 67.1 | 9.0 | 10.8 | 67.3 | 42.9 | 90.0 | 83.7 |
| 04/27/2009 | 81.1 | 59.2 | 16.0 | 26.0 | 14.3 | 0.2 | 90.0 | 83.7 |
| 04/29/2009 | 83.6 | 68.7 | 10.9 | 16.6 | 33.3 | 0.0 | 90.0 | 84.9 |
| 04/30/2009 | 76.4 | 56.0 | 16.1 | 20.1 | 26.4 | 0.0 | 90.0 | 84.3 |
| 05/01/2009 | 83.0 | 68.5 | 10.2 | 14.6 | 15.7 | 0.5 | 90.0 | 84.3 |
| 05/04/2009 | 70.1 | 45.5 | 24.7 | 30.4 | 15.8 | 0.5 | 90.0 | 82.3 |
| 05/14/2009 | 84.0 | 70.0 | 8.8 | 11.9 | 37.3 | 20.7 | 90.0 | 85.6 |
| 05/23/2009 | 83.9 | 69.9 | 11.7 | 15.6 | 29.8 | 0.3 | 90.0 | 85.6 |

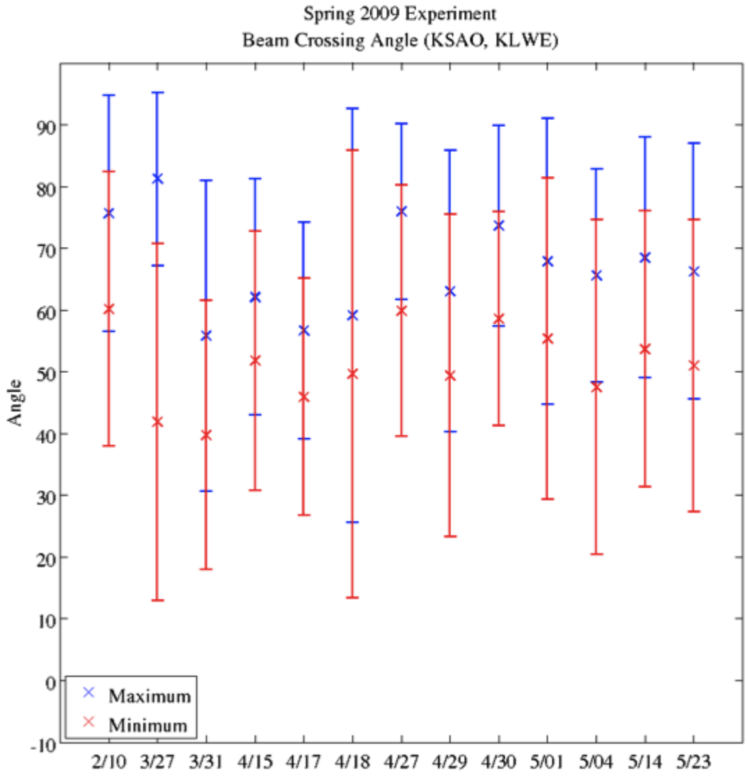

Figure 4.7: Bar chart of the minimum and maximum beam crossing angles for (KSAO, KLWE).

Table 4.7: Statistics for minimum and maximum beam crossing angles for (KSAO, KLWE)

| Date | Mean (°) | | std (°) | | Minimum (°) | | Maximum (°) | |
|---|---|---|---|---|---|---|---|---|
| | Best | Worst | Best | Worst | Best | Worst | Best | Worst |
| 02/10/2009 | 75.6 | 60.2 | 19.2 | 22.2 | 7.6 | 0.1 | 90.0 | 86.4 |
| 03/27/2009 | 81.2 | 41.9 | 14.0 | 28.9 | 37.6 | 0.3 | 90.0 | 85.6 |
| 03/31/2009 | 55.8 | 39.8 | 25.2 | 21.8 | 7.2 | 0.1 | 90.0 | 84.9 |
| 04/15/2009 | 62.1 | 51.8 | 19.1 | 21.0 | 17.0 | 2.8 | 90.0 | 84.9 |
| 04/17/2009 | 56.6 | 45.9 | 17.6 | 19.2 | 17.0 | 2.8 | 84.3 | 75.5 |
| 04/18/2009 | 59.1 | 49.7 | 33.5 | 36.2 | 9.3 | 0.0 | 90.0 | 86.4 |
| 04/27/2009 | 76.0 | 59.9 | 14.2 | 20.3 | 26.2 | 2.8 | 90.0 | 85.6 |
| 04/29/2009 | 63.0 | 49.4 | 22.8 | 26.1 | 12.4 | 0.0 | 90.0 | 86.4 |
| 04/30/2009 | 73.6 | 58.6 | 16.2 | 17.3 | 13.0 | 0.8 | 90.0 | 85.6 |
| 05/01/2009 | 67.8 | 55.3 | 23.2 | 26.0 | 7.3 | 0.1 | 90.0 | 86.4 |
| 05/04/2009 | 65.5 | 47.5 | 17.2 | 27.1 | 18.9 | 0.2 | 90.0 | 84.3 |
| 05/14/2009 | 68.5 | 53.7 | 19.5 | 22.4 | 10.4 | 0.1 | 90.0 | 85.6 |
| 05/23/2009 | 66.2 | 51.0 | 20.7 | 23.7 | 19.1 | 1.0 | 90.0 | 85.6 |

normalized standard deviation are determined by relating the minimum and maximum beam crossing angle to the normalized standard deviation (see Chapter 3). The expected bound is given as $\frac{1}{n}\sum_{i=1}^{N} csc^2\beta$. Using the beam crossing angles for each pair the expected lower and upper bounds were determined for the 13 events that make up the 2009 spring experiment. Tables 4.2.1.2 - 4.2.1.2 give the expected upper and lower bounds for all six pairs. Based on these results the collected data for each pair is bounded between 1 m/s and 2 m/s. Data that lies in regions that exceed the 2 m/s are thresholded out in the retrieval process. Therefore, between the dual-Doppler scan strategy and the retrieval process it is expected that the collected data is within the sufficient beam crossing regions for a reliable retrieval.

#### 4.2.1.3 Number of Elevation/Tilt Angles, Maximum Elevation/Tilt Angle, and Maximum Observation Altitude

The number of elevation/tilt angles, maximum elevation/tilt angle, and maximum observation altitude can be used to determine the possibility of retrieving vertical air motion in the CASA IP1 network. The number of elevation/tilt angles and maximum

Table 4.8: Minimum and maximum error bounds for (KCYR, KSAO)

| Date | Minimum Bound (m/s) | Maximum bound (m/s) |
|---|---|---|
| 02/10/2009 | 1.0 | 1.2 |
| 03/27/2009 | 1.0 | 1.7 |
| 03/31/2009 | 1.0 | 1.2 |
| 04/15/2009 | 1.1 | 1.2 |
| 04/17/2009 | 1.0 | 1.2 |
| 04/18/2009 | 1.0 | 1.1 |
| 04/27/2009 | 1.0 | 1.1 |
| 04/29/2009 | 1.0 | 1.1 |
| 04/30/2009 | NA | NA |
| 05/01/2009 | 1.0 | 1.1 |
| 05/04/2009 | 1.1 | 1.4 |
| 05/14/2009 | 1.0 | 1.1 |
| 05/23/2009 | 1.0 | 1.2 |

Table 4.9: Minimum and maximum error bounds for (KCYR, KRSP)

| Date | Minimum Bound (m/s) | Maximum bound (m/s) |
|---|---|---|
| 02/10/2009 | 1.0 | 1.2 |
| 03/27/2009 | 1.0 | 1.7 |
| 03/31/2009 | 1.0 | 1.1 |
| 04/15/2009 | 1.0 | 1.2 |
| 04/17/2009 | 1.0 | 1.1 |
| 04/18/2009 | 1.0 | 1.1 |
| 04/27/2009 | 1.0 | 1.1 |
| 04/29/2009 | 1.0 | 1.2 |
| 04/30/2009 | NA | NA |
| 05/01/2009 | 1.0 | 1.2 |
| 05/04/2009 | 1.0 | 1.5 |
| 05/14/2009 | 1.0 | 1.1 |
| 05/23/2009 | 1.0 | 1.1 |

Table 4.10: Minimum and maximum error bounds for (KCYR, KLWE)

| Date | Minimum Bound (m/s) | Maximum bound (m/s) |
|---|---|---|
| 02/10/2009 | 1.1 | 1.4 |
| 03/27/2009 | 1.3 | 1.7 |
| 03/31/2009 | 1.3 | 1.6 |
| 04/15/2009 | 1.2 | 1.4 |
| 04/17/2009 | 1.3 | 1.6 |
| 04/18/2009 | 1.1 | 1.4 |
| 04/27/2009 | 1.0 | 1.2 |
| 04/29/2009 | 1.1 | 1.3 |
| 04/30/2009 | NA | NA |
| 05/01/2009 | 1.1 | 1.3 |
| 05/04/2009 | 1.3 | 1.4 |
| 05/14/2009 | 1.0 | 1.2 |
| 05/23/2009 | 1.1 | 1.3 |

Table 4.11: Minimum and maximum error bounds for (KRSP, KSAO)

| Date | Minimum Bound (m/s) | Maximum bound (m/s) |
|---|---|---|
| 02/10/2009 | 1.2 | 1.5 |
| 03/27/2009 | 1.0 | 2.7 |
| 03/31/2009 | 1.1 | 1.5 |
| 04/15/2009 | 1.2 | 1.6 |
| 04/17/2009 | 1.2 | 1.6 |
| 04/18/2009 | 1.2 | 1.5 |
| 04/27/2009 | 1.0 | 1.3 |
| 04/29/2009 | 1.1 | 1.5 |
| 04/30/2009 | 1.2 | 1.7 |
| 05/01/2009 | 1.1 | 1.3 |
| 05/04/2009 | 1.2 | 2.1 |
| 05/14/2009 | 1.2 | 1.7 |
| 05/23/2009 | 1.2 | 1.6 |

Table 4.12: Minimum and maximum error bounds for (KRSP, KLWE)

| Date | Minimum Bound (m/s) | Maximum bound (m/s) |
|---|---|---|
| 02/10/2009 | 1.0 | 1.1 |
| 03/27/2009 | 1.0 | 1.4 |
| 03/31/2009 | 1.0 | 1.1 |
| 04/15/2009 | 1.0 | 1.1 |
| 04/17/2009 | 1.0 | 1.2 |
| 04/18/2009 | 1.0 | 1.1 |
| 04/27/2009 | 1.0 | 1.2 |
| 04/29/2009 | 1.0 | 1.1 |
| 04/30/2009 | 1.0 | 1.2 |
| 05/01/2009 | 1.0 | 1.1 |
| 05/04/2009 | 1.0 | 1.4 |
| 05/14/2009 | 1.0 | 1.1 |
| 05/23/2009 | 1.0 | 1.1 |

Table 4.13: Minimum and maximum error bounds for (KSAO, KLWE)

| Date | Minimum Bound (m/s) | Maximum bound (m/s) |
|---|---|---|
| 02/10/2009 | 1.0 | 1.2 |
| 03/27/2009 | 1.0 | 1.5 |
| 03/31/2009 | 1.2 | 1.6 |
| 04/15/2009 | 1.1 | 1.3 |
| 04/17/2009 | 1.2 | 1.4 |
| 04/18/2009 | 1.2 | 1.3 |
| 04/27/2009 | 1.0 | 1.2 |
| 04/29/2009 | 1.1 | 1.3 |
| 04/30/2009 | 1.0 | 1.2 |
| 05/01/2009 | 1.1 | 1.2 |
| 05/04/2009 | 1.1 | 1.4 |
| 05/14/2009 | 1.1 | 1.2 |
| 05/23/2009 | 1.1 | 1.3 |

elevation angle are logged by the MCC during real-time operations. The maximum observation altitude is computed from the maximum elevation angle and the slant range of the target. For a 4/3-Earth model, the maximum observation altitude is computed as:

$$H = Rsin\phi + \frac{R^2}{2R_e} \tag{4.1}$$

Where $R$ is the slant range, $\phi$ is the elevation/tilt angle and $R_e$ is the radius of the Earth. Figure 4.8 gives the relation between the height of a target and the Earth's radius.

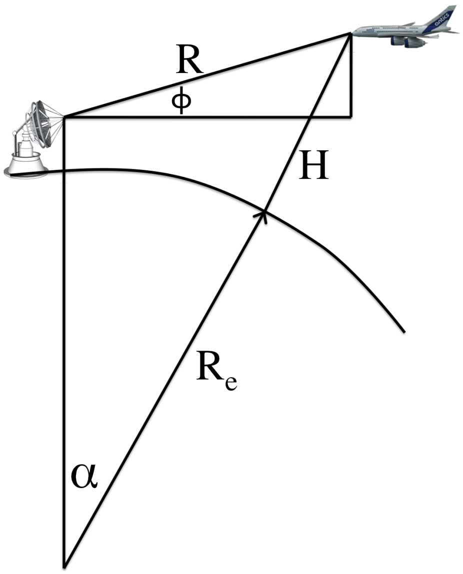

Figure 4.8: Relation between target height and Earth's radius.

Bar chart for the number of elevation/tilt angles per heartbeat are given for each pair in figures 4.9 - 4.14 and tables 4.14 - 4.19 summarize the statistics for the plots. Bar chart for the maximum elevation/tilts angle per heartbeat are given for each pair in figures 4.15 - 4.20 and tables 4.20 - 4.25 summarize the statistics for the plots. Bar chart for the maximum observation altitude per heartbeat are given for each pair in figures 4.21 - 4.26 and tables 4.26 - 4.31 summarize the statistics for the plots.

From the results in tables 4.26 - 4.31 the average maximum observation altitude for each radar in each pair is not sufficient for retrieving vertical air motion during normal operation (non-CLASIC mode) of the IP1 network. On average the IP1 radars cover three to five kilometers of the vertical atmosphere, which makes it difficult to retrieve vertical air motion using a reliable method since a storm is rarely topped throughout the entire dual-Doppler domain. This makes it difficult in setting the boundary condition at the top of storm for the downward integration method, and the upward integration method produces results that are too erroneous. Typical storm tops during the spring and summer months can exceed 10 km. Figure 4.27 shows reflectivity data from an ARM vertical profiler collected on April 29, 2009. In the figure the storm top is around 12 km above ground level (AGL) and at some time periods exceeds 12 km. With an elevation set of $\{1, 2, 3, 5, 7, 9, 11, 13, 16, 19\}$ the IP1 radars are only able to scan a height of 12 km AGL at a slant range of 40 km. Therefore the IP1 radars are unable to top a storm at ranges close to the radar. Figure 4.28 shows the CASA beam height versus slant range for a 4/3-Earth model. The figure uses the $\{1, 2, 3, 5, 7, 9, 11, 13, 16, 19\}$ elevation angle set to compute the observation altitude above ground as a function of slant range. Although for some events the maximum measured observation altitude exceeds 12 km, this occurred when using a elevation angle set other then $\{1, 2, 3, 5, 7, 9, 11, 13, 16, 19\}$. For instance on May 4, 2009, the elevation set was

$$\{1.00, 2.00, 3.15, 5.28, 7.40, 9.50, 11.57, 13.62, 15.92, 18.57, 21.57, 28.70\}$$

However, the average maximum elevation angle was between 4 ° -12 ° for each radar in each pair. This corresponds to an average maximum observation altitude, at a slant range of 40 kilometers, between 2.6 km and 7.7 km. Figure 4.29 shows the CASA beam height versus slant range for the May 4, 2009 elevation angle set. For vertical velocity retrieval to be possible, the CASA heartbeat would have to be extended beyond 1 minute so that more elevation angles could be included in the scan task. Also the

$\{1, 2, 3, 5, 7, 9, 11, 13, 16, 19\}$ elevation set would have to be increased to include larger elevation angles so that the storm could be topped close to the radar.

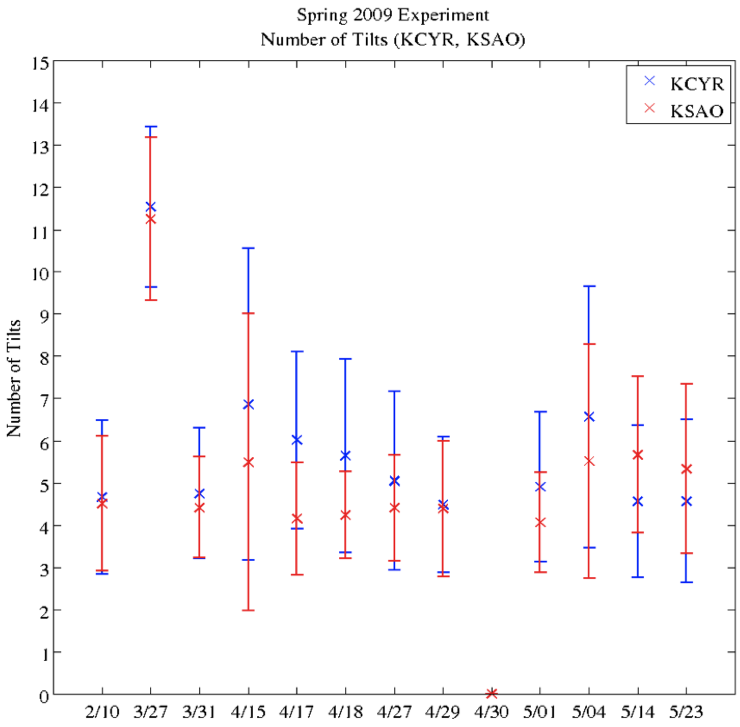

Figure 4.9: Number of elevation angles per heartbeat for (KCYR, KSAO).

Table 4.14: Statistics for number of elevation angles for (KCYR, KSAO)

| Date | Mean | | std | | Minimum | | Maximum | |
|---|---|---|---|---|---|---|---|---|
| | KCYR | KSAO | KCYR | KSAO | KCYR | KSAO | KCYR | KSAO |
| 02/10/2009 | 4.7 | 4.5 | 1.8 | 1.6 | 3.0 | 3.0 | 8.0 | 8.0 |
| 03/27/2009 | 11.5 | 11.3 | 1.9 | 1.9 | 9.0 | 9.0 | 13.0 | 13.0 |
| 03/31/2009 | 4.8 | 4.4 | 1.6 | 1.2 | 3.0 | 3.0 | 7.0 | 9.0 |
| 04/15/2009 | 6.9 | 5.5 | 3.7 | 3.5 | 3.0 | 3.0 | 19.0 | 18.0 |
| 04/17/2009 | 6.0 | 4.1 | 2.1 | 1.3 | 3.0 | 3.0 | 10.0 | 10.0 |
| 04/18/2009 | 5.6 | 4.2 | 2.3 | 1.0 | 3.0 | 3.0 | 7.0 | 10.0 |
| 04/27/2009 | 5.0 | 4.4 | 2.1 | 1.3 | 3.0 | 3.0 | 10.0 | 10.0 |
| 04/29/2009 | 4.5 | 4.4 | 1.6 | 1.6 | 3.0 | 3.0 | 13.0 | 11.0 |
| 04/30/2009 | NA | NA | NA | NA | NA | NA | NA | NA |
| 05/01/2009 | 4.9 | 4.1 | 1.8 | 1.2 | 3.0 | 3.0 | 10.0 | 10.0 |
| 05/04/2009 | 6.6 | 5.5 | 3.1 | 2.8 | 3.0 | 3.0 | 13.0 | 13.0 |
| 05/14/2009 | 4.6 | 5.7 | 1.8 | 1.9 | 3.0 | 3.0 | 10.0 | 10.0 |
| 05/23/2009 | 4.6 | 5.3 | 1.9 | 2.0 | 3.0 | 3.0 | 10.0 | 10.0 |

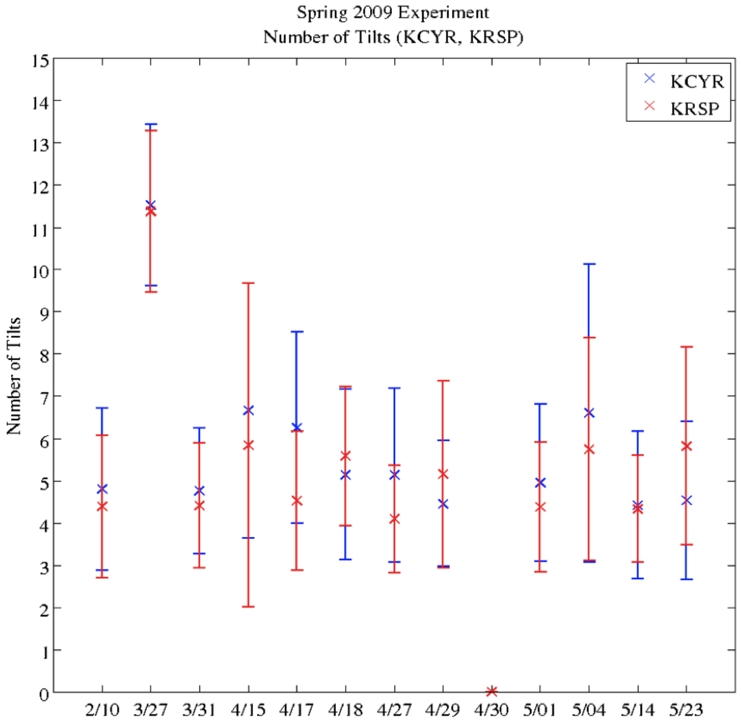

Figure 4.10: Number of elevation angles per heartbeat for (KCYR, KRSP).

Table 4.15: Statistics for number of elevation angles for (KCYR, KRSP)

| Date | Mean | | std | | Minimum | | Maximum | |
|---|---|---|---|---|---|---|---|---|
| | KCYR | KRSP | KCYR | KRSP | KCYR | KRSP | KCYR | KRSP |
| 02/10/2009 | 4.8 | 4.4 | 1.9 | 1.7 | 3.0 | 3.0 | 8.0 | 8.0 |
| 03/27/2009 | 11.5 | 11.4 | 1.9 | 1.9 | 9.0 | 9.0 | 13.0 | 13.0 |
| 03/31/2009 | 4.8 | 4.4 | 1.5 | 1.5 | 3.0 | 3.0 | 9.0 | 8.0 |
| 04/15/2009 | 6.7 | 5.8 | 3.0 | 3.8 | 3.0 | 3.0 | 17.0 | 19.0 |
| 04/17/2009 | 6.2 | 4.5 | 2.3 | 1.7 | 3.0 | 3.0 | 10.0 | 10.0 |
| 04/18/2009 | 5.1 | 5.6 | 2.0 | 1.7 | 3.0 | 3.0 | 10.0 | 10.0 |
| 04/27/2009 | 5.1 | 4.1 | 2.1 | 1.3 | 3.0 | 3.0 | 10.0 | 10.0 |
| 04/29/2009 | 4.5 | 5.1 | 1.5 | 2.2 | 3.0 | 3.0 | 11.0 | 13.0 |
| 04/30/2009 | NA | NA | NA | NA | NA | NA | NA | NA |
| 05/01/2009 | 5.0 | 4.4 | 1.9 | 1.5 | 3.0 | 3.0 | 10.0 | 10.0 |
| 05/04/2009 | 6.6 | 5.7 | 3.5 | 2.6 | 3.0 | 3.0 | 13.0 | 13.0 |
| 05/14/2009 | 4.4 | 4.3 | 1.7 | 1.3 | 3.0 | 3.0 | 10.0 | 9.0 |
| 05/23/2009 | 4.5 | 5.8 | 1.9 | 2.3 | 3.0 | 3.0 | 10.0 | 10.0 |

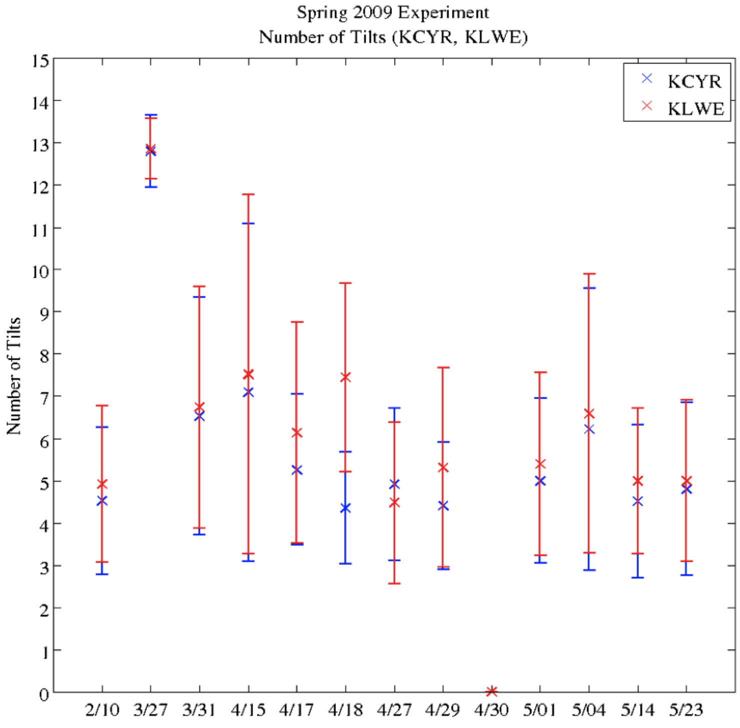

Figure 4.11: Number of elevation angles per heartbeat for (KCYR, KLWE).

Table 4.16: Statistics for number of elevation angles for (KCYR, KLWE)

| Date | Mean | | std | | Minimum | | Maximum | |
|---|---|---|---|---|---|---|---|---|
| | KCYR | KLWE | KCYR | KLWE | KCYR | KLWE | KCYR | KLWE |
| 02/10/2009 | 4.5 | 4.9 | 1.8 | 1.8 | 3.0 | 3.0 | 8.0 | 8.0 |
| 03/27/2009 | 12.8 | 12.9 | 0.9 | 0.7 | 9.0 | 9.0 | 13.0 | 13.0 |
| 03/31/2009 | 6.5 | 6.7 | 2.8 | 2.9 | 3.0 | 3.0 | 10.0 | 10.0 |
| 04/15/2009 | 7.1 | 7.5 | 4.0 | 4.3 | 3.0 | 3.0 | 18.0 | 19.0 |
| 04/17/2009 | 5.3 | 6.1 | 1.8 | 2.6 | 3.0 | 3.0 | 10.0 | 10.0 |
| 04/18/2009 | 4.4 | 7.4 | 1.3 | 2.2 | 3.0 | 3.0 | 8.0 | 10.0 |
| 04/27/2009 | 4.9 | 4.5 | 1.8 | 1.9 | 3.0 | 3.0 | 10.0 | 10.0 |
| 04/29/2009 | 4.4 | 5.3 | 1.5 | 2.4 | 3.0 | 3.0 | 11.0 | 13.0 |
| 04/30/2009 | NA | NA | NA | NA | NA | NA | NA | NA |
| 05/01/2009 | 5.0 | 5.4 | 1.9 | 2.2 | 3.0 | 3.0 | 10.0 | 10.0 |
| 05/04/2009 | 6.2 | 6.6 | 3.3 | 3.3 | 3.0 | 3.0 | 13.0 | 13.0 |
| 05/14/2009 | 4.5 | 5.0 | 1.8 | 1.7 | 3.0 | 3.0 | 10.0 | 10.0 |
| 05/23/2009 | 4.8 | 5.0 | 2.0 | 1.9 | 3.0 | 3.0 | 10.0 | 10.0 |

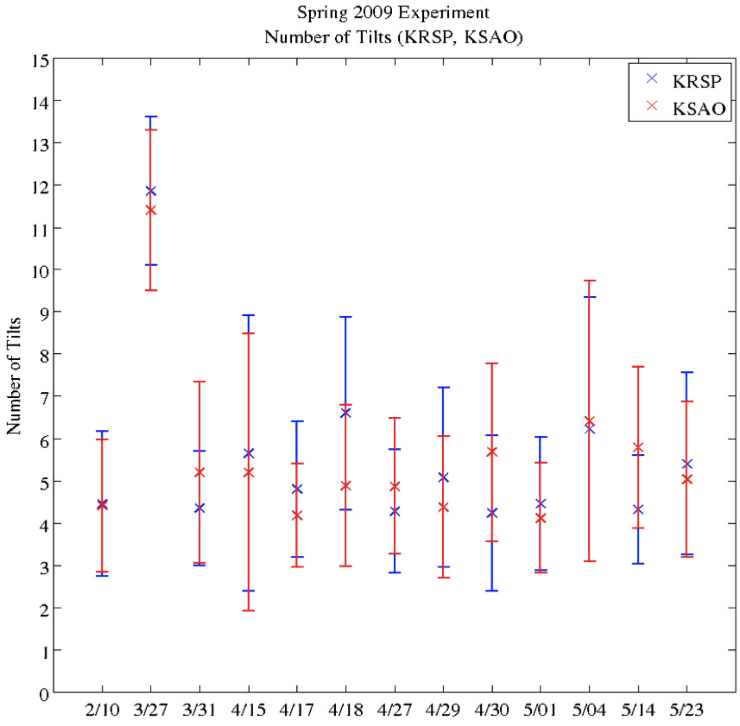

Figure 4.12: Number of elevation angles per heartbeat for (KRSP, KSAO).

Table 4.17: Statistics for number of elevation angles for (KRSP, KSAO)

| Date | Mean | | std | | Minimum | | Maximum | |
|---|---|---|---|---|---|---|---|---|
| | KRSP | KSAO | KRSP | KSAO | KRSP | KSAO | KRSP | KSAO |
| 02/10/2009 | 4.4 | 4.4 | 1.7 | 1.6 | 3.0 | 3.0 | 8.0 | 8.0 |
| 03/27/2009 | 11.9 | 11.4 | 1.8 | 1.9 | 9.0 | 9.0 | 13.0 | 13.0 |
| 03/31/2009 | 4.3 | 5.2 | 1.4 | 2.1 | 3.0 | 3.0 | 8.0 | 10.0 |
| 04/15/2009 | 5.6 | 5.2 | 3.3 | 3.3 | 3.0 | 3.0 | 19.0 | 19.0 |
| 04/17/2009 | 4.8 | 4.2 | 1.6 | 1.2 | 3.0 | 3.0 | 10.0 | 10.0 |
| 04/18/2009 | 6.6 | 4.9 | 2.3 | 1.9 | 3.0 | 3.0 | 10.0 | 10.0 |
| 04/27/2009 | 4.3 | 4.9 | 1.5 | 1.6 | 3.0 | 3.0 | 10.0 | 10.0 |
| 04/29/2009 | 5.1 | 4.4 | 2.1 | 1.7 | 3.0 | 3.0 | 13.0 | 13.0 |
| 04/30/2009 | 4.2 | 5.7 | 1.8 | 2.1 | 3.0 | 3.0 | 13.0 | 10.0 |
| 05/01/2009 | 4.5 | 4.1 | 1.6 | 1.3 | 3.0 | 3.0 | 10.0 | 10.0 |
| 05/04/2009 | 6.2 | 6.4 | 3.1 | 3.3 | 3.0 | 3.0 | 13.0 | 13.0 |
| 05/14/2009 | 4.3 | 5.8 | 1.3 | 1.9 | 3.0 | 3.0 | 9.0 | 10.0 |
| 05/23/2009 | 5.4 | 5.0 | 2.2 | 1.8 | 3.0 | 3.0 | 10.0 | 10.0 |

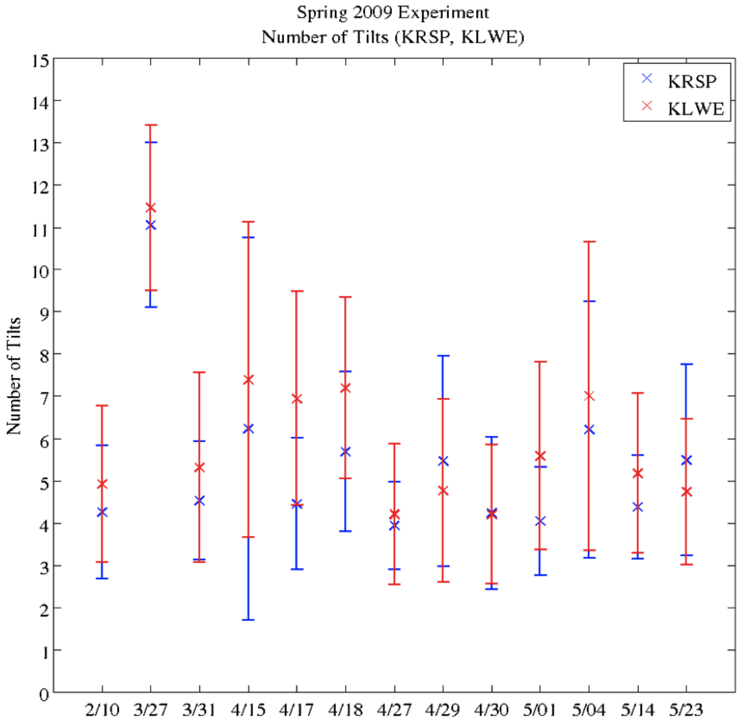

Figure 4.13: Number of elevation angles per heartbeat for (KRSP, KLWE).

Table 4.18: Statistics for number of elevation angles for (KRSP, KLWE)

| Date | Mean | | std | | Minimum | | Maximum | |
|---|---|---|---|---|---|---|---|---|
| | KRSP | KLWE | KRSP | KLWE | KRSP | KLWE | KRSP | KLWE |
| 02/10/2009 | 4.3 | 4.9 | 1.6 | 1.9 | 3.0 | 3.0 | 8.0 | 8.0 |
| 03/27/2009 | 11.1 | 11.5 | 2.0 | 2.0 | 9.0 | 9.0 | 13.0 | 13.0 |
| 03/31/2009 | 4.5 | 5.3 | 1.4 | 2.2 | 3.0 | 3.0 | 8.0 | 10.0 |
| 04/15/2009 | 6.2 | 7.4 | 4.5 | 3.7 | 3.0 | 3.0 | 19.0 | 19.0 |
| 04/17/2009 | 4.4 | 6.9 | 1.6 | 2.5 | 3.0 | 3.0 | 10.0 | 10.0 |
| 04/18/2009 | 5.7 | 7.2 | 1.9 | 2.1 | 3.0 | 3.0 | 10.0 | 10.0 |
| 04/27/2009 | 3.9 | 4.2 | 1.0 | 1.7 | 3.0 | 3.0 | 8.0 | 10.0 |
| 04/29/2009 | 5.5 | 4.8 | 2.5 | 2.2 | 3.0 | 3.0 | 13.0 | 13.0 |
| 04/30/2009 | 4.2 | 4.2 | 1.8 | 1.6 | 3.0 | 3.0 | 13.0 | 13.0 |
| 05/01/2009 | 4.0 | 5.6 | 1.3 | 2.2 | 3.0 | 3.0 | 10.0 | 10.0 |
| 05/04/2009 | 6.2 | 7.0 | 3.0 | 3.7 | 3.0 | 3.0 | 13.0 | 13.0 |
| 05/14/2009 | 4.4 | 5.2 | 1.2 | 1.9 | 3.0 | 3.0 | 8.0 | 10.0 |
| 05/23/2009 | 5.5 | 4.7 | 2.3 | 1.7 | 3.0 | 3.0 | 10.0 | 10.0 |

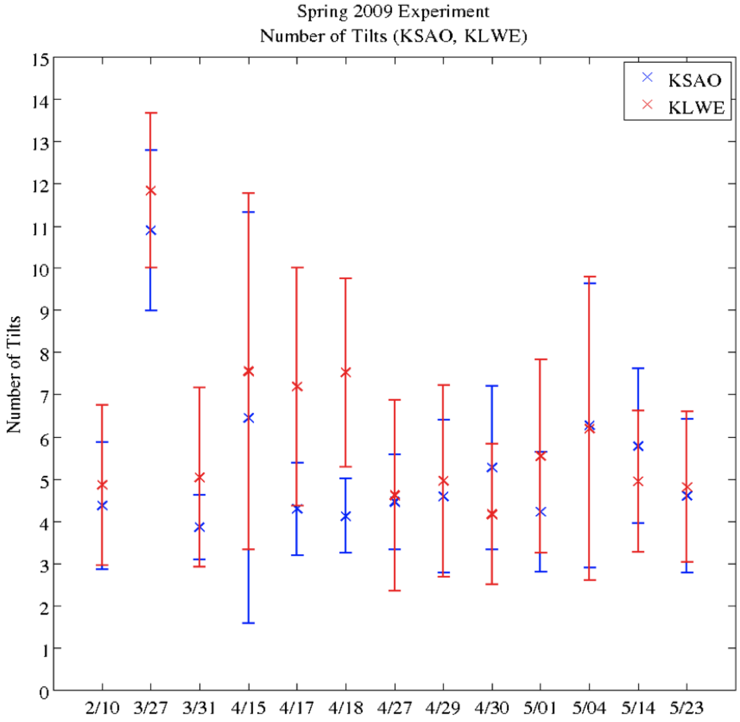

Figure 4.14: Number of elevation angles per heartbeat for (KSAO, KLWE).

Table 4.19: Statistics for number of elevation angles for (KSAO, KLWE)

| Date | Mean | | std | | Minimum | | Maximum | |
|---|---|---|---|---|---|---|---|---|
| | KSAO | KLWE | KSAO | KLWE | KSAO | KLWE | KSAO | KLWE |
| 02/10/2009 | 4.4 | 4.9 | 1.5 | 1.9 | 3.0 | 3.0 | 8.0 | 8.0 |
| 03/27/2009 | 10.9 | 11.8 | 1.9 | 1.8 | 9.0 | 9.0 | 13.0 | 13.0 |
| 03/31/2009 | 3.9 | 5.0 | 0.8 | 2.1 | 3.0 | 3.0 | 5.0 | 10.0 |
| 04/15/2009 | 6.4 | 7.6 | 4.9 | 4.2 | 3.0 | 3.0 | 19.0 | 19.0 |
| 04/17/2009 | 4.3 | 7.2 | 1.1 | 2.8 | 3.0 | 3.0 | 6.0 | 10.0 |
| 04/18/2009 | 4.1 | 7.5 | 0.9 | 2.2 | 3.0 | 3.0 | 6.0 | 10.0 |
| 04/27/2009 | 4.5 | 4.6 | 1.1 | 2.3 | 3.0 | 3.0 | 7.0 | 10.0 |
| 04/29/2009 | 4.6 | 5.0 | 1.2 | 2.3 | 3.0 | 3.0 | 13.0 | 13.0 |
| 04/30/2009 | 5.3 | 4.2 | 1.9 | 1.7 | 3.0 | 3.0 | 10.0 | 13.0 |
| 05/01/2009 | 4.2 | 5.5 | 1.4 | 2.3 | 3.0 | 3.0 | 10.0 | 10.0 |
| 05/04/2009 | 6.3 | 6.2 | 3.4 | 3.6 | 3.0 | 3.0 | 13.0 | 13.0 |
| 05/14/2009 | 5.8 | 4.9 | 1.8 | 1.7 | 3.0 | 3.0 | 10.0 | 10.0 |
| 05/23/2009 | 4.6 | 4.8 | 1.8 | 1.8 | 3.0 | 3.0 | 10.0 | 10.0 |

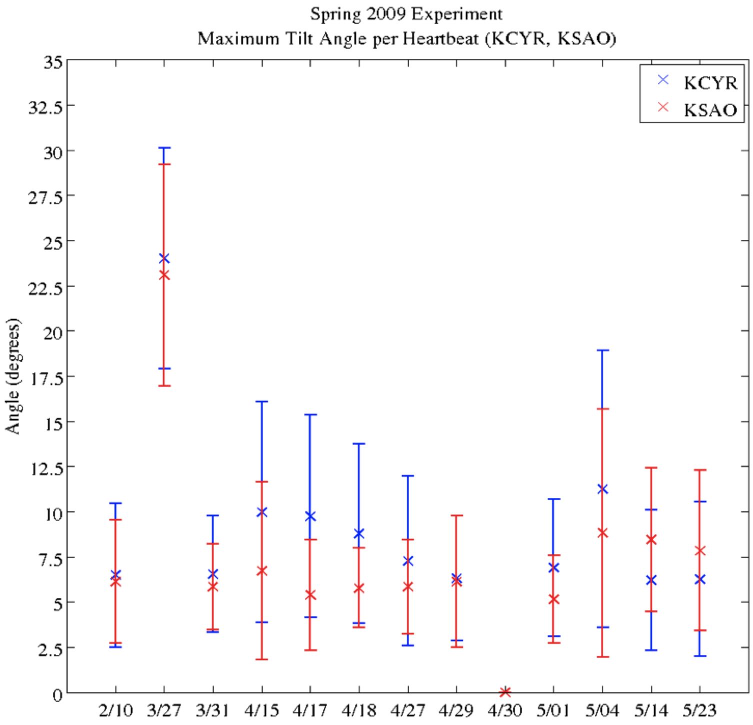

Figure 4.15: Maximum elevation angle per heartbeat for (KCYR, KSAO).

Table 4.20: Statistics for the maximum elevation/tilt angles for the pair (KCYR, KSAO)

| Date | Mean (°) | | std (°) | | Minimum (°) | | Maximum (°) | |
|---|---|---|---|---|---|---|---|---|
| | KCYR | KSAO | KCYR | KSAO | KCYR | KSAO | KCYR | KSAO |
| 02/10/2009 | 6.5 | 6.1 | 4.0 | 3.4 | 3.0 | 3.0 | 14.0 | 14.0 |
| 03/27/2009 | 24.0 | 23.1 | 6.1 | 6.1 | 15.9 | 15.9 | 28.7 | 28.7 |
| 03/31/2009 | 6.5 | 5.8 | 3.2 | 2.4 | 3.0 | 3.0 | 17.0 | 11.0 |
| 04/15/2009 | 10.0 | 6.7 | 6.1 | 4.9 | 3.0 | 3.0 | 25.0 | 28.7 |
| 04/17/2009 | 9.7 | 5.4 | 5.6 | 3.1 | 3.0 | 3.0 | 22.0 | 22.0 |
| 04/18/2009 | 8.8 | 5.8 | 5.0 | 2.2 | 3.2 | 3.2 | 18.56 | 11.6 |
| 04/27/2009 | 7.3 | 5.8 | 4.7 | 2.6 | 3.0 | 3.0 | 19.0 | 19.0 |
| 04/29/2009 | 6.3 | 6.1 | 3.4 | 3.6 | 3.2 | 3.2 | 21.6 | 28.7 |
| 04/30/2009 | NA | NA | NA | NA | NA | NA | NA | NA |
| 05/01/2009 | 6.9 | 5.1 | 3.8 | 2.4 | 3.0 | 3.0 | 19.0 | 19.0 |
| 05/04/2009 | 11.2 | 8.8 | 7.7 | 6.9 | 3.2 | 3.2 | 28.7 | 28.7 |
| 05/14/2009 | 6.2 | 8.4 | 3.9 | 4.0 | 3.0 | 3.0 | 19.0 | 19.0 |
| 05/23/2009 | 6.3 | 7.8 | 4.3 | 4.4 | 3.0 | 3.0 | 19.0 | 19.0 |

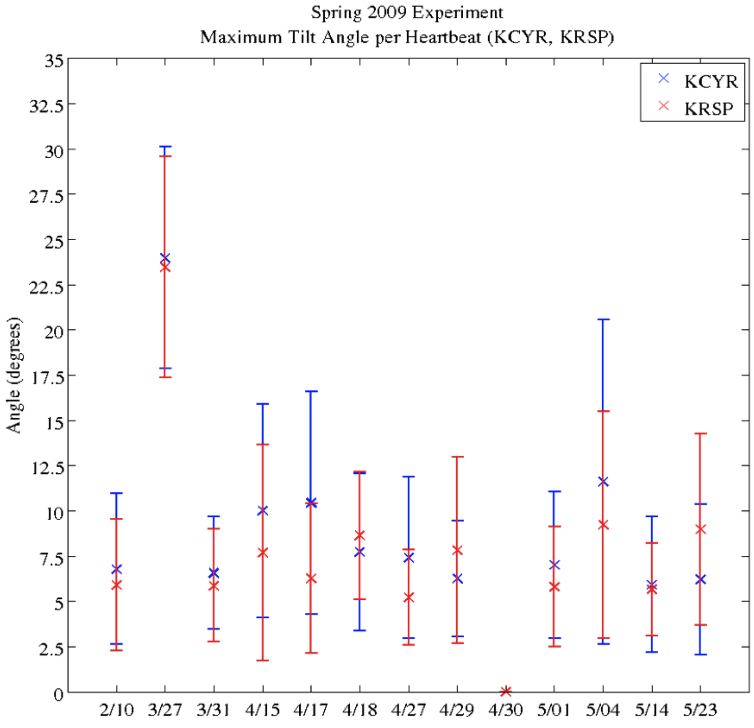

Figure 4.16: Maximum elevation angle per heartbeat for (KCYR, KRSP).

Table 4.21: Statistics for the maximum elevation/tilt angles for the pair (KCYR, KRSP)

| Date | Mean (°) | | std (°) | | Minimum (°) | | Maximum (°) | |
|---|---|---|---|---|---|---|---|---|
| | KCYR | KRSP | KCYR | KRSP | KCYR | KRSP | KCYR | KRSP |
| 02/10/2009 | 6.8 | 5.9 | 4.2 | 3.6 | 3.0 | 3.0 | 14.0 | 14.0 |
| 03/27/2009 | 24.0 | 23.5 | 6.1 | 6.1 | 15.9 | 15.9 | 28.7 | 28.7 |
| 03/31/2009 | 6.6 | 5.9 | 3.1 | 3.1 | 3.0 | 3.0 | 17.0 | 14.0 |
| 04/15/2009 | 10.0 | 7.7 | 5.9 | 6.0 | 3.0 | 3.0 | 22.0 | 28.7 |
| 04/17/2009 | 10.4 | 6.3 | 6.1 | 4.1 | 3.0 | 3.0 | 22.0 | 22.0 |
| 04/18/2009 | 7.7 | 8.6 | 4.3 | 3.5 | 3.2 | 3.2 | 18.6 | 18.6 |
| 04/27/2009 | 7.4 | 5.2 | 4.5 | 2.6 | 3.0 | 3.0 | 19.0 | 19.0 |
| 04/29/2009 | 6.2 | 7.8 | 3.2 | 5.1 | 3.2 | 3.2 | 21.6 | 28.7 |
| 04/30/2009 | NA | NA | NA | NA | NA | NA | NA | NA |
| 05/01/2009 | 7.0 | 5.8 | 4.0 | 3.3 | 3.0 | 3.0 | 19.0 | 19.0 |
| 05/04/2009 | 11.6 | 9.2 | 9.0 | 6.3 | 3.2 | 3.2 | 28.7 | 28.7 |
| 05/14/2009 | 5.9 | 5.7 | 3.7 | 2.6 | 3.0 | 3.0 | 19.0 | 16.0 |
| 05/23/2009 | 6.2 | 9.0 | 4.2 | 5.3 | 3.0 | 3.0 | 19.0 | 19.0 |

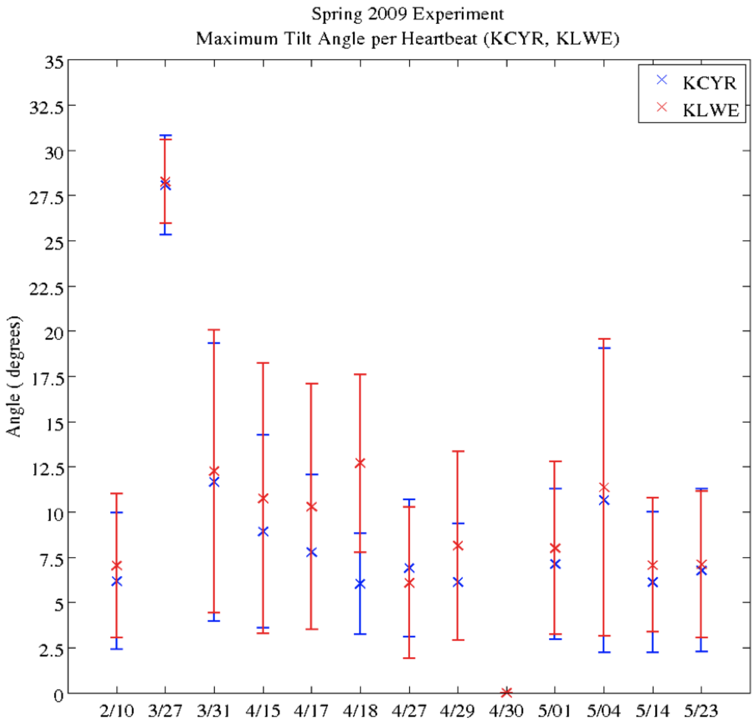

Figure 4.17: Maximum elevation angle per heartbeat for (KCYR, KLWE).

Table 4.22: Statistics for the maximum elevation/tilt angles for the pair (KCYR, KLWE)

| Date | Mean (°) | | std (°) | | Minimum (°) | | Maximum (°) | |
|---|---|---|---|---|---|---|---|---|
| | KCYR | KLWE | KCYR | KLWE | KCYR | KLWE | KCYR | KLWE |
| 02/10/2009 | 6.2 | 7.0 | 3.8 | 4.0 | 3.0 | 3.0 | 14.0 | 14.0 |
| 03/27/2009 | 28.1 | 28.3 | 2.8 | 2.3 | 15.9 | 15.9 | 28.7 | 28.7 |
| 03/31/2009 | 11.7 | 12.2 | 7.7 | 7.8 | 3.0 | 3.0 | 22.0 | 22.0 |
| 04/15/2009 | 8.9 | 10.7 | 5.3 | 7.5 | 3.0 | 3.0 | 25.0 | 28.7 |
| 04/17/2009 | 7.8 | 10.3 | 4.3 | 6.8 | 3.0 | 3.0 | 22.0 | 22.0 |
| 04/18/2009 | 6.0 | 12.7 | 2.8 | 4.9 | 3.2 | 3.2 | 13.6 | 18.6 |
| 04/27/2009 | 6.9 | 6.1 | 3.8 | 4.2 | 3.0 | 3.0 | 19.0 | 19.0 |
| 04/29/2009 | 6.1 | 8.1 | 3.2 | 5.2 | 3.2 | 3.2 | 21.6 | 28.7 |
| 04/30/2009 | NA | NA | NA | NA | NA | NA | NA | NA |
| 05/01/2009 | 7.1 | 8.0 | 4.2 | 4.8 | 3.0 | 3.0 | 19.0 | 19.0 |
| 05/04/2009 | 10.6 | 11.4 | 8.4 | 8.2 | 3.2 | 3.2 | 28.7 | 28.7 |
| 05/14/2009 | 6.1 | 7.1 | 3.9 | 3.7 | 3.0 | 3.0 | 19.0 | 19.0 |
| 05/23/2009 | 6.8 | 7.1 | 4.5 | 4.1 | 3.0 | 3.0 | 19.0 | 19.0 |

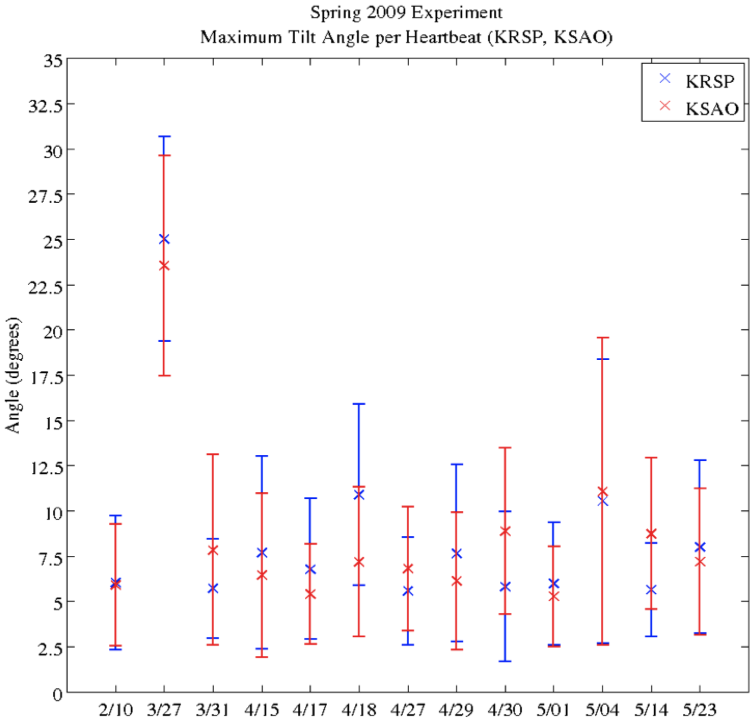

Figure 4.18: Maximum elevation angle per heartbeat for (KRSP, KSAO).

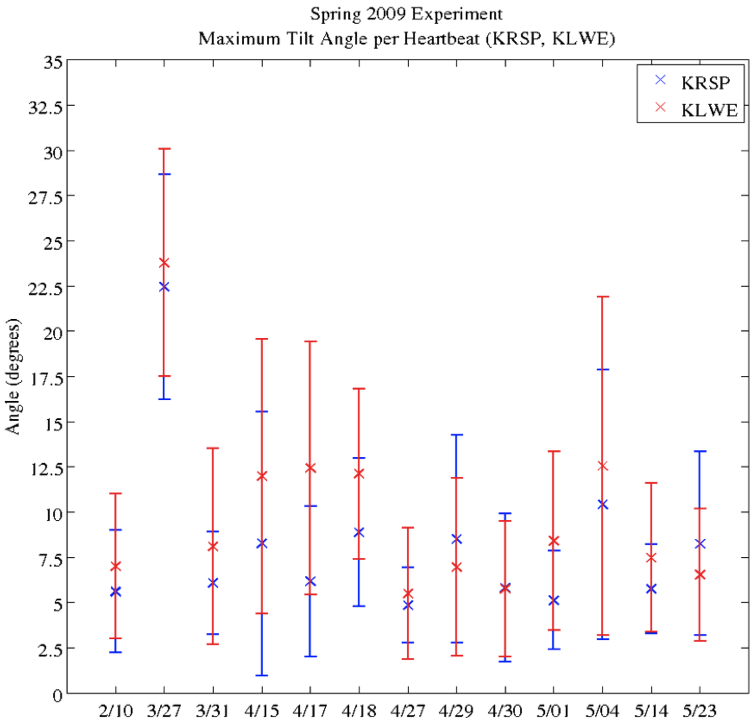

Figure 4.19: Maximum elevation angle per heartbeat for (KRSP, KLWE).

Table 4.23: Statistics for the maximum elevation/tilt angles for the pair (KRSP, KSAO)

| Date | Mean (°) | | std (°) | | Minimum (°) | | Maximum (°) | |
|---|---|---|---|---|---|---|---|---|
| | KRSP | KSAO | KRSP | KSAO | KRSP | KSAO | KRSP | KSAO |
| 02/10/2009 | 6.0 | 5.9 | 3.7 | 3.4 | 3.0 | 3.0 | 14.0 | 14.0 |
| 03/27/2009 | 25.0 | 23.6 | 5.6 | 6.1 | 15.9 | 15.9 | 28.7 | 28.7 |
| 03/31/2009 | 5.7 | 7.8 | 2.7 | 5.3 | 3.0 | 3.0 | 14.0 | 22.0 |
| 04/15/2009 | 7.7 | 6.4 | 5.3 | 4.5 | 3.0 | 3.0 | 28.7 | 28.7 |
| 04/17/2009 | 6.8 | 5.4 | 3.9 | 2.8 | 3.0 | 3.0 | 22.0 | 22.0 |
| 04/18/2009 | 10.9 | 7.2 | 5.0 | 4.1 | 3.2 | 3.2 | 18.6 | 18.6 |
| 04/27/2009 | 5.6 | 6.8 | 3.0 | 3.4 | 3.0 | 3.0 | 19.0 | 19.0 |
| 04/29/2009 | 7.7 | 6.1 | 4.9 | 3.8 | 3.2 | 3.2 | 28.7 | 28.7 |
| 04/30/2009 | 5.8 | 8.9 | 4.1 | 4.6 | 3.2 | 3.2 | 28.7 | 18.6 |
| 05/01/2009 | 6.0 | 5.3 | 3.4 | 2.8 | 3.0 | 3.0 | 19.0 | 19.0 |
| 05/04/2009 | 10.5 | 11.0 | 7.8 | 8.5 | 3.2 | 3.2 | 28.7 | 28.7 |
| 05/14/2009 | 5.6 | 8.7 | 2.6 | 4.2 | 3.0 | 3.0 | 16.0 | 19.0 |
| 05/23/2009 | 8.0 | 7.2 | 4.8 | 4.0 | 3.0 | 3.0 | 19.0 | 19.0 |

Table 4.24: Statistics for the maximum elevation/tilt angles for the pair (KRSP, KLWE)

| Date | Mean (°) | | std (°) | | Minimum (°) | | Maximum (°) | |
|---|---|---|---|---|---|---|---|---|
| | KRSP | KLWE | KRSP | KLWE | KRSP | KLWE | KRSP | KLWE |
| 02/10/2009 | 5.6 | 7.0 | 3.4 | 4.0 | 3.0 | 3.0 | 14.0 | 14.0 |
| 03/27/2009 | 22.4 | 23.8 | 6.2 | 6.3 | 15.9 | 15.9 | 28.7 | 28.7 |
| 03/31/2009 | 6.1 | 8.1 | 2.8 | 5.4 | 3.0 | 3.0 | 14.0 | 22.0 |
| 04/15/2009 | 8.3 | 12.0 | 7.3 | 7.6 | 3.0 | 3.0 | 28.7 | 28.7 |
| 04/17/2009 | 6.2 | 12.4 | 4.2 | 7.0 | 3.0 | 3.0 | 22.0 | 22.0 |
| 04/18/2009 | 8.9 | 12.1 | 4.1 | 4.7 | 3.2 | 3.2 | 18.6 | 18.6 |
| 04/27/2009 | 4.9 | 5.5 | 2.1 | 3.6 | 3.0 | 3.0 | 13.0 | 19.0 |
| 04/29/2009 | 8.5 | 7.0 | 5.7 | 4.9 | 3.2 | 3.2 | 28.7 | 28.7 |
| 04/30/2009 | 5.8 | 5.7 | 4.1 | 3.7 | 3.2 | 3.2 | 28.7 | 28.7 |
| 05/01/2009 | 5.1 | 8.4 | 2.7 | 4.9 | 3.0 | 3.0 | 19.0 | 19.0 |
| 05/04/2009 | 10.4 | 12.5 | 7.5 | 9.3 | 3.2 | 3.2 | 28.7 | 28.7 |
| 05/14/2009 | 5.7 | 7.5 | 2.5 | 4.1 | 3.0 | 3.0 | 13.0 | 19.0 |
| 05/23/2009 | 8.2 | 6.5 | 5.1 | 3.7 | 3.0 | 3.0 | 19.0 | 19.0 |

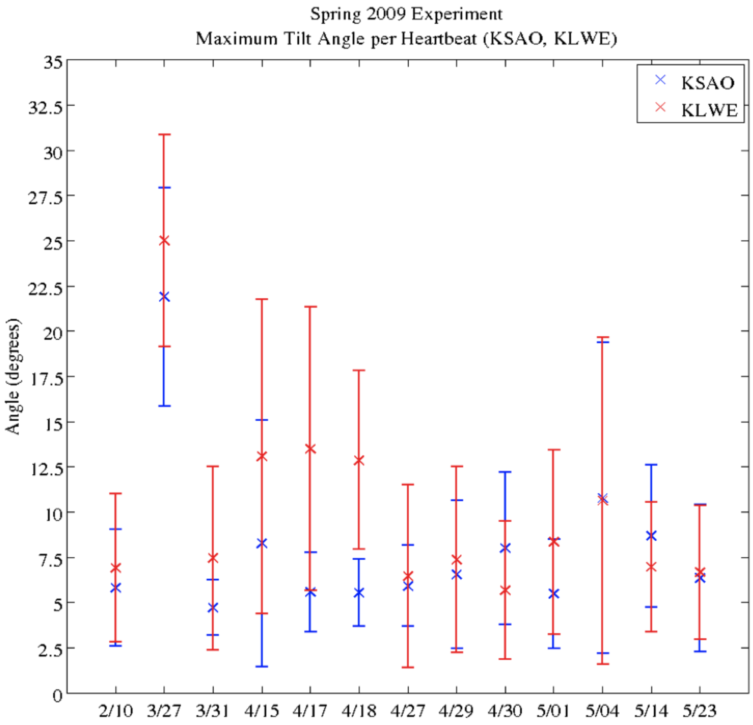

Figure 4.20: Maximum elevation angle per heartbeat for (KSAO, KLWE).

Table 4.25: Statistics for the maximum elevation/tilt angles for the pair (KSAO, KLWE)

| Date | Mean (°) | | std (°) | | Minimum (°) | | Maximum (°) | |
|---|---|---|---|---|---|---|---|---|
| | KSAO | KLWE | KSAO | KLWE | KSAO | KLWE | KSAO | KLWE |
| 02/10/2009 | 6.0 | 6.0 | 3.4 | 3.7 | 3.0 | 3.0 | 14.0 | 14.0 |
| 03/27/2009 | 23.6 | 25.0 | 6.1 | 5.6 | 15.9 | 15.9 | 28.7 | 28.7 |
| 03/31/2009 | 7.8 | 5.7 | 5.3 | 2.7 | 3.0 | 3.0 | 22.0 | 14.0 |
| 04/15/2009 | 6.4 | 7.7 | 4.5 | 5.3 | 3.0 | 3.0 | 28.7 | 28.7 |
| 04/17/2009 | 5.4 | 6.8 | 2.8 | 3.9 | 3.0 | 3.0 | 22.0 | 22.0 |
| 04/18/2009 | 7.2 | 10.9 | 4.1 | 5.0 | 3.2 | 3.2 | 18.6 | 18.6 |
| 04/27/2009 | 6.8 | 5.6 | 3.4 | 3.0 | 3.0 | 3.0 | 19.0 | 19.0 |
| 04/29/2009 | 6.1 | 7.7 | 3.8 | 4.9 | 3.2 | 3.2 | 28.7 | 28.7 |
| 04/30/2009 | 8.9 | 5.8 | 4.6 | 4.1 | 3.2 | 3.2 | 18.6 | 28.7 |
| 05/01/2009 | 5.3 | 6.0 | 2.8 | 3.4 | 3.0 | 3.0 | 19.0 | 19.0 |
| 05/04/2009 | 11.1 | 10.5 | 8.5 | 7.8 | 3.2 | 3.2 | 28.7 | 28.7 |
| 05/14/2009 | 8.7 | 5.6 | 4.2 | 2.6 | 3.0 | 3.0 | 19.0 | 16.0 |
| 05/23/2009 | 7.2 | 8.0 | 4.0 | 4.8 | 3.0 | 3.0 | 19.0 | 19.0 |

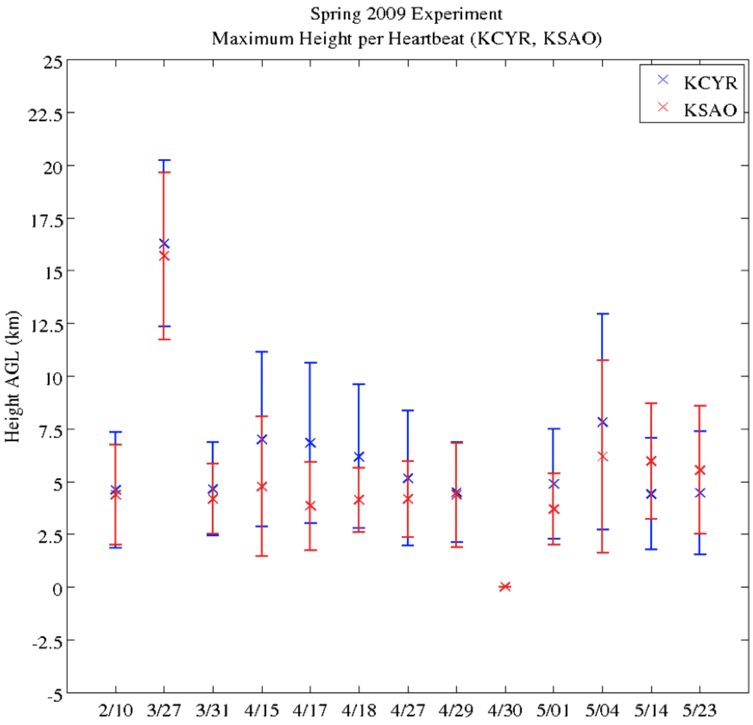

Figure 4.21: Maximum observation altitude for (KCYR, KSAO).

Table 4.26: Statistics for the maximum observation altitude for the pair (KCYR, KSAO)

| Date | Mean (km) | | std (km) | | Minimum (km) | | Maximum (km) | |
|---|---|---|---|---|---|---|---|---|
| | KCYR | KSAO | KCYR | KSAO | KCYR | KSAO | KCYR | KSAO |
| 7 02/10/2009 | 4.6 | 4.4 | 2.7 | 2.4 | 2.2 | 2.2 | 9.8 | 9.8 |
| 03/27/2009 | 16.3 | 15.7 | 3.9 | 4.0 | 11.1 | 11.1 | 19.3 | 19.3 |
| 03/31/2009 | 4.7 | 4.2 | 2.2 | 1.7 | 2.2 | 2.2 | 11.8 | 7.7 |
| 04/15/2009 | 7.0 | 4.8 | 4.1 | 3.3 | 2.2 | 2.2 | 17.0 | 19.3 |
| 04/17/2009 | 6.8 | 3.8 | 3.8 | 2.1 | 2.2 | 2.2 | 15.1 | 15.1 |
| 04/18/2009 | 6.2 | 4.1 | 3.4 | 1.5 | 2.3 | 2.3 | 12.8 | 8.1 |
| 04/27/2009 | 5.1 | 4.2 | 3.2 | 1.8 | 2.2 | 2.2 | 13.1 | 13.1 |
| 04/29/2009 | 4.5 | 4.4 | 2.4 | 2.5 | 2.3 | 2.3 | 14.8 | 19.3 |
| 04/30/2009 | NA | NA | NA | NA | NA | NA | NA | NA |
| 05/01/2009 | 4.9 | 3.7 | 2.6 | 1.7 | 2.2 | 2.2 | 13.1 | 13.1 |
| 05/04/2009 | 7.8 | 6.2 | 5.1 | 4.6 | 2.3 | 2.3 | 19.3 | 19.3 |
| 05/14/2009 | 4.4 | 6.0 | 2.7 | 2.7 | 2.2 | 2.2 | 13.1 | 13.1 |
| 05/23/2009 | 4.5 | 5.5 | 2.9 | 3.0 | 2.2 | 2.2 | 13.1 | 13.1 |

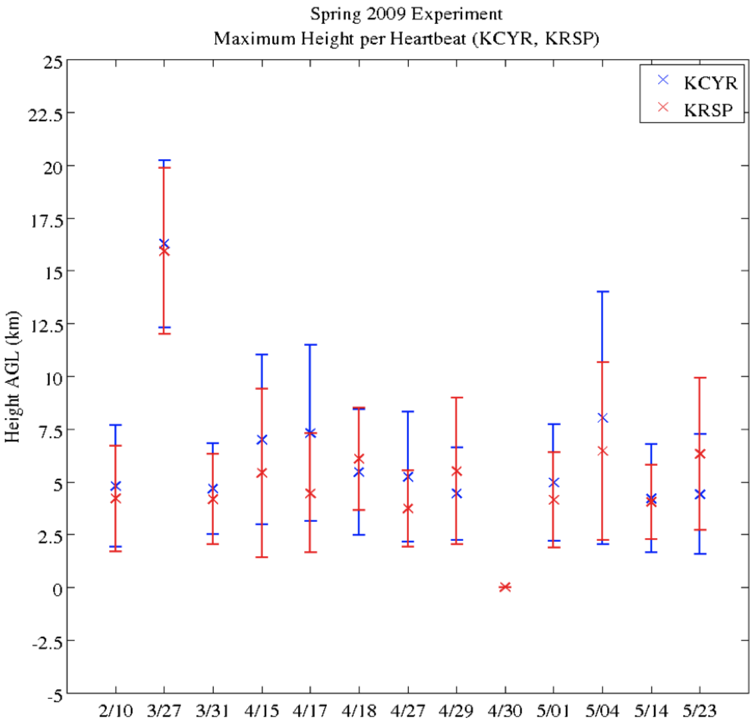

Figure 4.22: Maximum observation altitude for (KCYR, KRSP).

Table 4.27: Statistics for the maximum observation altitude for the pair (KCYR, KRSP)

| Date | Mean (km) | | std (km) | | Minimum (km) | | Maximum (km) | |
|---|---|---|---|---|---|---|---|---|
| | KCYR | KRSP | KCYR | KRSP | KCYR | KRSP | KCYR | KRSP |
| 7 02/10/2009 | 4.8 | 4.2 | 2.9 | 2.5 | 2.2 | 2.2 | 9.8 | 9.8 |
| 03/27/2009 | 16.3 | 16.0 | 3.9 | 3.9 | 11.0 | 11.1 | 19.3 | 19.3 |
| 03/31/2009 | 4.7 | 4.2 | 2.2 | 2.1 | 2.2 | 2.2 | 11.8 | 9.8 |
| 04/15/2009 | 7.0 | 5.4 | 4.0 | 4.0 | 2.2 | 2.2 | 15.1 | 19.3 |
| 04/17/2009 | 7.3 | 4.5 | 4.2 | 2.8 | 2.2 | 2.2 | 15.1 | 15.1 |
| 04/18/2009 | 5.5 | 6.1 | 3.0 | 2.4 | 2.3 | 2.3 | 12.8 | 12.8 |
| 04/27/2009 | 5.2 | 3.7 | 3.1 | 1.8 | 2.2 | 2.2 | 13.1 | 13.1 |
| 04/29/2009 | 4.4 | 5.5 | 2.2 | 3.5 | 2.3 | 2.3 | 14.8 | 19.3 |
| 04/30/2009 | NA | NA | NA | NA | NA | NA | NA | NA |
| 05/01/2009 | 5.0 | 4.1 | 2.8 | 2.3 | 2.2 | 2.2 | 13.1 | 13.1 |
| 05/04/2009 | 8.0 | 6.5 | 6.0 | 4.2 | 2.3 | 2.3 | 19.3 | 19.3 |
| 05/14/2009 | 4.2 | 4.0 | 2.6 | 1.8 | 2.2 | 2.2 | 13.1 | 11.1 |
| 05/23/2009 | 4.4 | 6.3 | 2.9 | 3.6 | 2.2 | 2.2 | 13.1 | 13.1 |

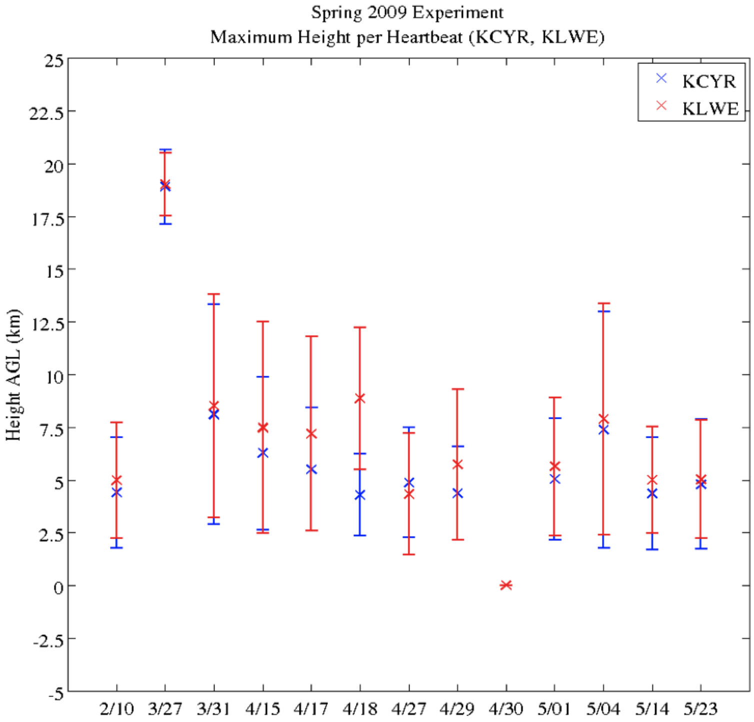

Figure 4.23: Maximum observation altitude per heartbeat for (KCYR, KLWE).

Table 4.28: Statistics for the maximum observation altitude for the pair (KCYR, KLWE)

| Date | Mean (km) | | std (km) | | Minimum (km) | | Maximum (km) | |
|---|---|---|---|---|---|---|---|---|
| | KCYR | KLWE | KCYR | KLWE | KCYR | KLWE | KCYR | KLWE |
| 7 02/10/2009 | 4.4 | 5.0 | 2.6 | 2.8 | 2.2 | 2.2 | 9.8 | 9.8 |
| 03/27/2009 | 18.9 | 19.0 | 1.8 | 1.5 | 11.1 | 11.1 | 19.3 | 19.3 |
| 03/31/2009 | 8.1 | 8.5 | 5.2 | 5.3 | 2.2 | 2.2 | 15.1 | 15.1 |
| 04/15/2009 | 6.3 | 7.5 | 3.6 | 5.0 | 2.2 | 2.2 | 17.0 | 19.3 |
| 04/17/2009 | 5.5 | 7.2 | 2.9 | 4.6 | 2.2 | 2.2 | 15.1 | 15.1 |
| 04/18/2009 | 4.3 | 8.9 | 1.9 | 3.4 | 2.3 | 2.3 | 9.5 | 12.8 |
| 04/27/2009 | 4.9 | 4.3 | 2.6 | 2.9 | 2.2 | 2.2 | 13.1 | 13.1 |
| 04/29/2009 | 4.4 | 5.7 | 2.2 | 3.6 | 2.3 | 2.3 | 14.8 | 19.3 |
| 04/30/2009 | NA | NA | NA | NA | NA | NA | NA | NA |
| 05/01/2009 | 5.0 | 5.6 | 2.9 | 3.3 | 2.2 | 2.2 | 13.1 | 13.1 |
| 05/04/2009 | 7.4 | 7.9 | 5.6 | 5.5 | 2.3 | 2.3 | 19.3 | 19.3 |
| 05/14/2009 | 4.4 | 5.0 | 2.7 | 2.5 | 2.2 | 2.2 | 13.1 | 13.1 |
| 05/23/2009 | 4.8 | 5.0 | 3.1 | 2.8 | 2.2 | 2.2 | 13.1 | 13.1 |

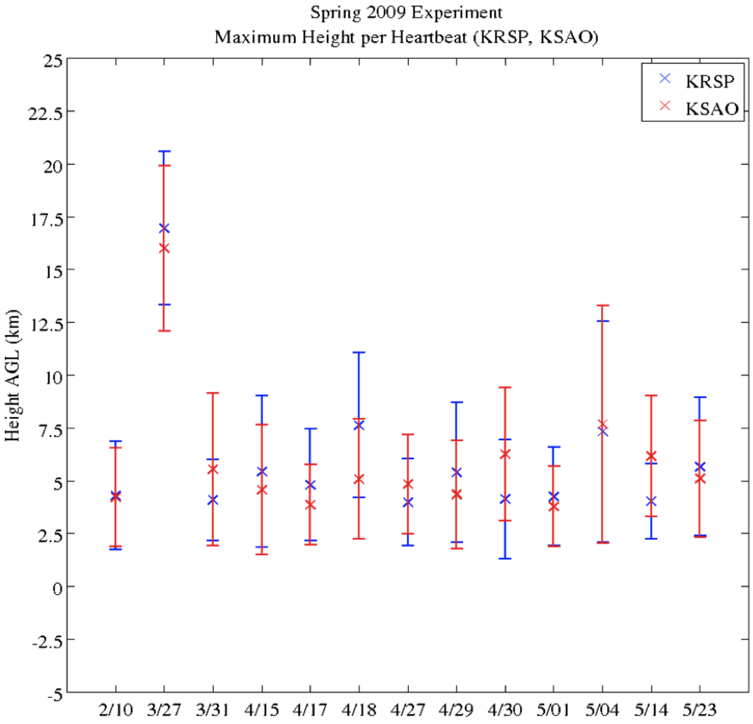

Figure 4.24: Maximum observation altitude per heartbeat for (KRSP, KSAO).

Table 4.29: Statistics for the maximum observation altitude for the pair (KRSP, KSAO)

| Date | Mean (km) | | std (km) | | Minimum (km) | | Maximum (km) | |
|---|---|---|---|---|---|---|---|---|
| | KRSP | KSAO | KRSP | KSAO | KRSP | KSAO | KRSP | KSAO |
| 02/10/2009 | 4.3 | 4.2 | 2.6 | 2.3 | 2.2 | 2.2 | 9.8 | 9.8 |
| 03/27/2009 | 17.0 | 16.0 | 3.6 | 3.9 | 11.1 | 11.1 | 19.3 | 19.3 |
| 03/31/2009 | 4.0 | 5.5 | 1.9 | 3.6 | 2.2 | 2.2 | 9.8 | 15.1 |
| 04/15/2009 | 5.4 | 4.6 | 3.6 | 3.1 | 2.2 | 2.2 | 19.3 | 19.3 |
| 04/17/2009 | 4.8 | 3.9 | 2.6 | 1.9 | 2.2 | 2.2 | 15.1 | 15.1 |
| 04/18/2009 | 7.6 | 5.1 | 3.4 | 2.9 | 2.3 | 2.3 | 12.8 | 12.8 |
| 04/27/2009 | 4.0 | 4.8 | 2.1 | 2.4 | 2.2 | 2.2 | 13.1 | 13.1 |
| 04/29/2009 | 5.4 | 4.3 | 3.3 | 2.6 | 2.3 | 2.3 | 19.3 | 19.3 |
| 04/30/2009 | 4.1 | 6.3 | 2.8 | 3.1 | 2.3 | 2.3 | 19.3 | 12.8 |
| 05/01/2009 | 4.3 | 3.8 | 2.3 | 1.9 | 2.2 | 2.2 | 13.1 | 13.1 |
| 05/04/2009 | 7.3 | 7.7 | 5.2 | 5.6 | 2.3 | 2.3 | 19.3 | 19.3 |
| 05/14/2009 | 4.0 | 6.2 | 1.8 | 2.9 | 2.2 | 2.2 | 11.1 | 13.1 |
| 05/23/2009 | 5.7 | 5.1 | 3.3 | 2.8 | 2.2 | 2.2 | 13.1 | 13.1 |

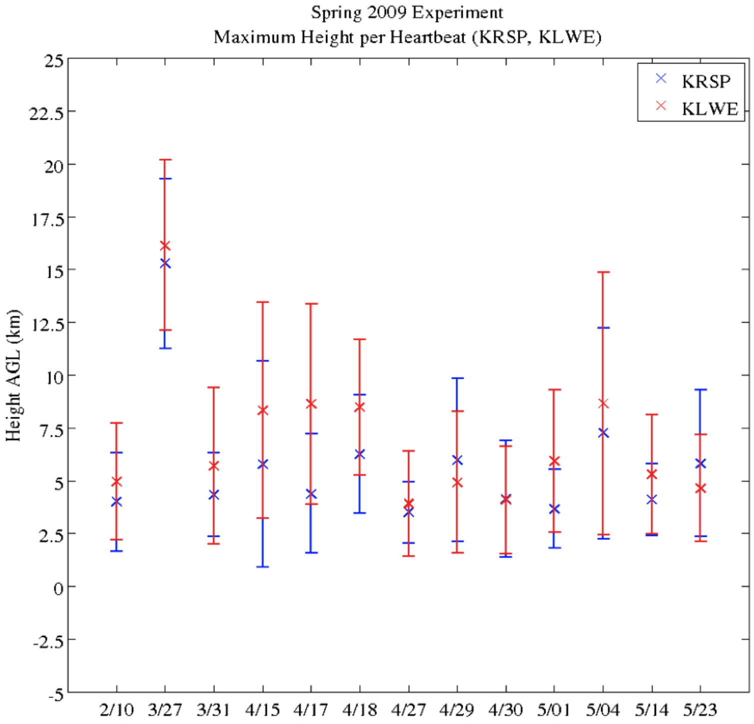

Figure 4.25: Maximum observation altitude per heartbeat for (KRSP, KLWE).

Table 4.30: Statistics for the maximum observation altitude for the pair (KRSP, KLWE)

| Date | Mean (km) | | std (km) | | Minimum (km) | | Maximum (km) | |
|---|---|---|---|---|---|---|---|---|
| | KRSP | KLWE | KRSP | KLWE | KRSP | KLWE | KRSP | KLWE |
| 02/10/2009 | 4.0 | 5.0 | 2.3 | 2.8 | 2.2 | 2.2 | 9.8 | 12.7 |
| 03/27/2009 | 15.3 | 16.1 | 4.0 | 4.0 | 11.0 | 11.1 | 19.3 | 9.8 |
| 03/31/2009 | 4.3 | 5.7 | 2.0 | 3.7 | 2.2 | 2.2 | 9.8 | 19.3 |
| 04/15/2009 | 5.8 | 8.3 | 4.9 | 5.1 | 2.2 | 2.2 | 19.3 | 15.1 |
| 04/17/2009 | 4.4 | 8.6 | 2.8 | 4.7 | 2.2 | 2.2 | 15.1 | 19.3 |
| 04/18/2009 | 6.3 | 8.5 | 2.8 | 3.2 | 2.3 | 2.3 | 12.8 | 15.1 |
| 04/27/2009 | 3.5 | 3.9 | 1.4 | 2.5 | 2.2 | 2.2 | 9.1 | 12.8 |
| 04/29/2009 | 6.0 | 4.9 | 3.9 | 3.3 | 2.3 | 2.3 | 19.3 | 13.1 |
| 04/30/2009 | 4.1 | 4.1 | 2.8 | 2.5 | 2.3 | 2.3 | 19.3 | 19.3 |
| 05/01/2009 | 3.7 | 5.9 | 1.9 | 3.4 | 2.2 | 2.2 | 13.1 | 19.3 |
| 05/04/2009 | 7.2 | 8.7 | 5.0 | 6.2 | 2.3 | 2.3 | 19.3 | 13.1 |
| 05/14/2009 | 4.1 | 5.3 | 1.7 | 2.8 | 2.2 | 2.2 | 9.1 | 19.3 |
| 05/23/2009 | 5.8 | 4.6 | 3.5 | 2.5 | 2.2 | 2.2 | 13.1 | 13.1 |

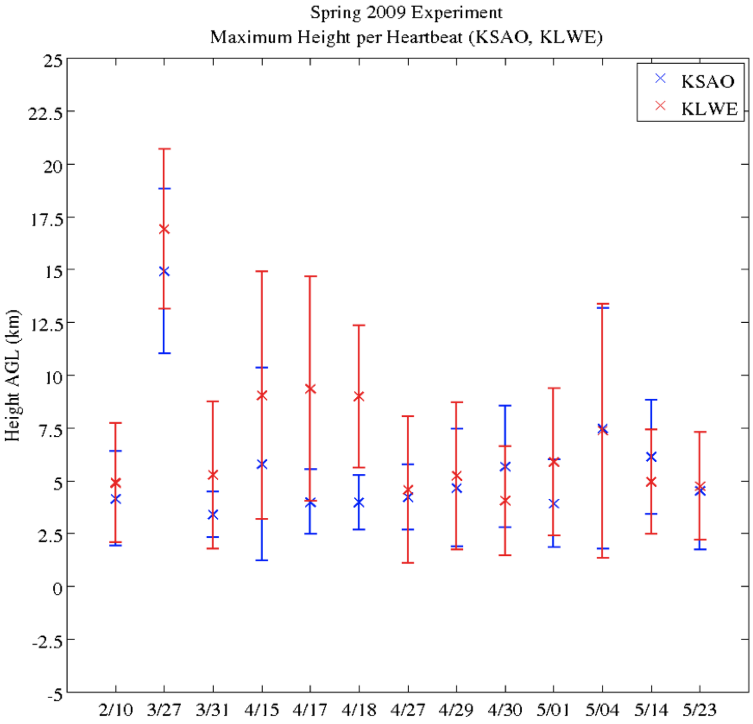

Figure 4.26: Maximum observation altitude per heartbeat for (KSAO, KLWE).

Table 4.31: Statistics for the maximum observation altitude for the pair (KSAO, KLWE)

| Date | Mean (km) | | std (km) | | Minimum (km) | | Maximum (km) | |
|---|---|---|---|---|---|---|---|---|
| | KSAO | KLWE | KSAO | KLWE | KSAO | KLWE | KSAO | KLWE |
| 02/10/2009 | 4.1 | 4.9 | 2.2 | 2.8 | 2.2 | 2.2 | 9.8 | 9.8 |
| 03/27/2009 | 14.9 | 16.9 | 3.9 | 3.8 | 11.1 | 11.1 | 19.3 | 19.3 |
| 03/31/2009 | 3.4 | 5.3 | 1.1 | 3.5 | 2.2 | 2.2 | 5.0 | 15.1 |
| 04/15/2009 | 5.8 | 9.0 | 4.6 | 5.9 | 2.2 | 2.2 | 19.3 | 19.3 |
| 04/17/2009 | 4.0 | 9.3 | 1.5 | 5.3 | 2.2 | 2.2 | 6.4 | 15.1 |
| 04/18/2009 | 4.0 | 9.0 | 1.3 | 3.4 | 2.3 | 2.3 | 6.7 | 12.8 |
| 04/27/2009 | 4.2 | 4.6 | 1.6 | 3.5 | 2.2 | 2.2 | 7.7 | 13.1 |
| 04/29/2009 | 4.7 | 5.2 | 2.8 | 3.5 | 2.3 | 2.3 | 19.3 | 19.3 |
| 04/30/2009 | 5.7 | 4.0 | 2.9 | 2.6 | 2.3 | 2.3 | 12.8 | 19.3 |
| 05/01/2009 | 3.9 | 5.9 | 2.1 | 3.5 | 2.2 | 2.2 | 13.1 | 13.1 |
| 05/04/2009 | 7.5 | 7.4 | 5.7 | 6.0 | 2.3 | 2.3 | 19.3 | 19.3 |
| 05/14/2009 | 6.1 | 4.9 | 2.7 | 2.5 | 2.2 | 2.2 | 13.1 | 13.1 |
| 05/23/2009 | 4.5 | 4.7 | 2.8 | 2.5 | 2.2 | 2.2 | 13.1 | 13.1 |

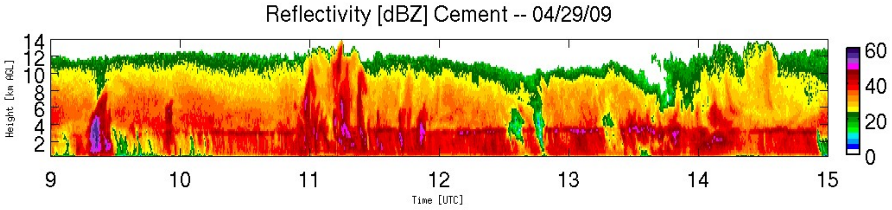

Figure 4.27: Reflectivity from April 29, 2009 from ARM profiler located in CASA domain.

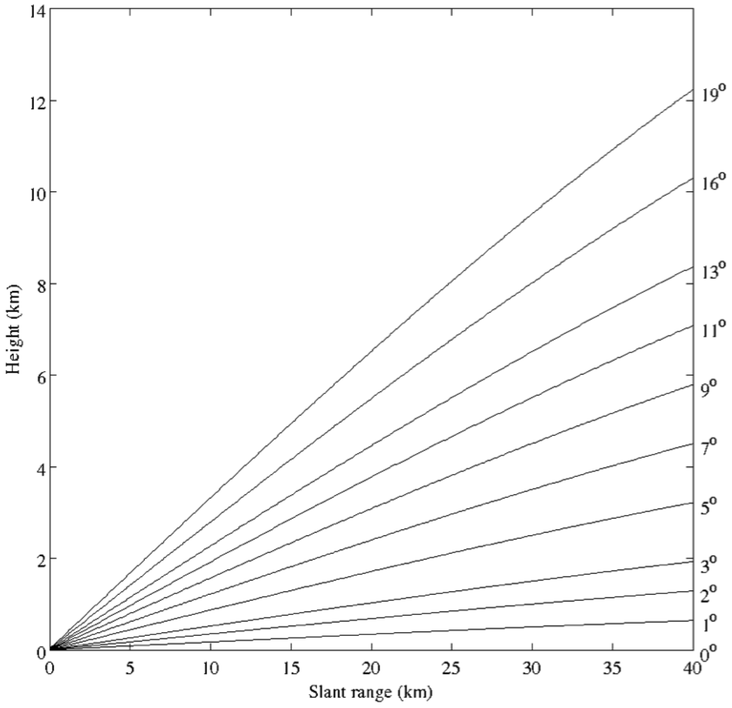

Figure 4.28: CASA beam height versus slant range for standard elevation angle set

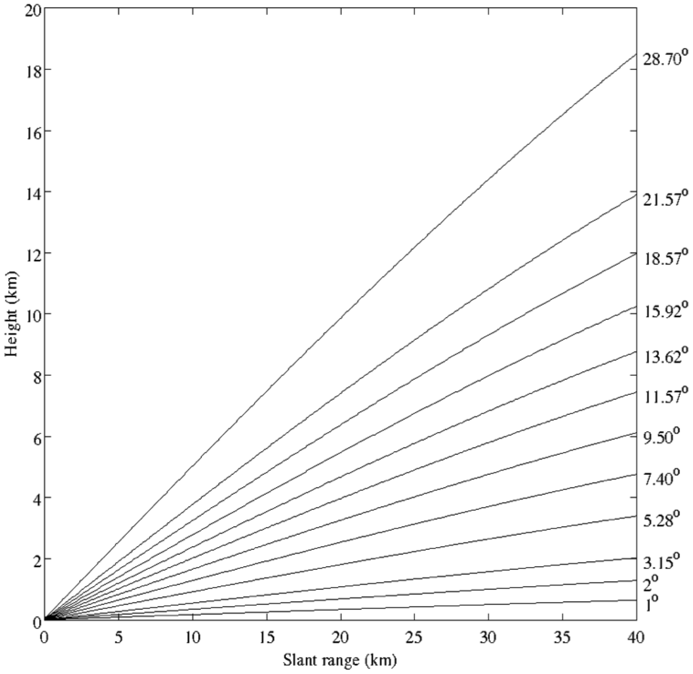

Figure 4.29: CASA beam height versus slant range for May 4, 2009 elevation angle set

#### 4.2.1.4 Synchronization Time

The synchronization between two radars for a given pair determines how well synchronized the data between two radars in a pair is. The closer in time that the radars are synchronized the closer in time the collected data is matched. Small time differences between data collection times is need as this will determine how much the collected volumes will need to be advected. This is an important characteristic of the scan strategy since the process of wind filed retrieval assumes that the data from both radars is collected at the same time. During operations the synchronization time is measured as the time that the netCDF file is stored at the SOCC.

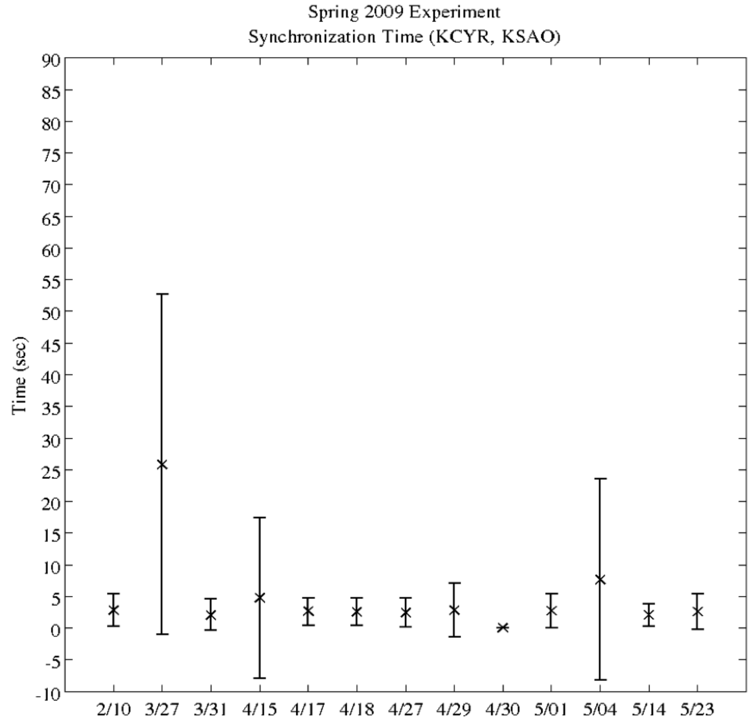

Figure 4.30: Bar chart of the synchronization time between KCYR and KSAO.

The given results for the six pairs indicate that on average the beam synchronization error is relatively small. This suggests that minimum advection needs to be applied to the collected reflectivity and velocity data, and that the data collected between radars in a given pair is well matched in time. However, there are times

Table 4.32: Statistics for synchronization time between KCYR and KSAO

| Date | Mean (sec) | std (sec) | Minimum (sec) | Maximum (sec) |
|---|---|---|---|---|
| 02/10/2009 | 2.8 | 2.6 | 0.0 | 14.3 |
| 03/27/2009 | 25.8 | 26.8 | 0.0 | 97.3 |
| 03/31/2009 | 2.0 | 2.5 | 0.0 | 14.9 |
| 04/15/2009 | 4.7 | 12.7 | 0.0 | 90.3 |
| 04/17/2009 | 2.6 | 2.2 | 0.0 | 8.0 |
| 04/18/2009 | 2.6 | 2.2 | 0.0 | 8.8 |
| 04/27/2009 | 2.4 | 2.3 | 0.0 | 11.6 |
| 04/29/2009 | 2.8 | 4.3 | 0.0 | 57.3 |
| 04/30/2009 | NA | NA | NA | NA |
| 05/01/2009 | 2.7 | 2.7 | 0.0 | 15.5 |
| 05/04/2009 | 7.6 | 15.9 | 0.0 | 67.4 |
| 05/14/2009 | 2.1 | 1.78 | 0.0 | 8.6 |
| 05/23/2009 | 2.6 | 2.8 | 0.0 | 35.7 |

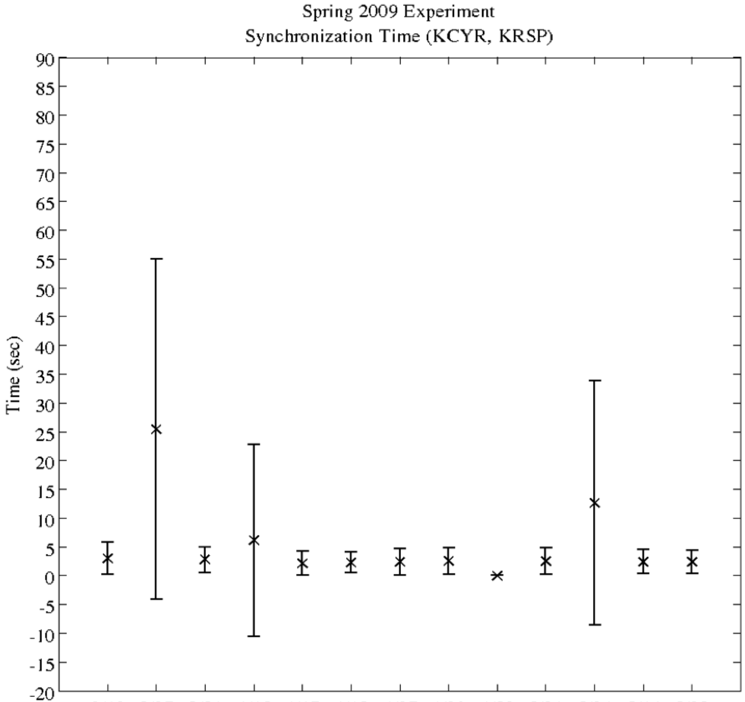

Figure 4.31: Bar chart of the synchronization time between KCYR and KRSP.

Table 4.33: Statistics for synchronization time between KCYR and KRSP

| Date | Mean (sec) | std (sec) | Minimum (sec) | Maximum (sec) |
|---|---|---|---|---|
| 02/10/2009 | 3.0 | 2.8 | 0.0 | 17.0 |
| 03/27/2009 | 25.5 | 29.6 | 0.0 | 97.3 |
| 03/31/2009 | 2.8 | 2.2 | 0.0 | 8.6 |
| 04/15/2009 | 6.1 | 16.6 | 0.0 | 94.0 |
| 04/17/2009 | 2.1 | 2.1 | 0.0 | 8.6 |
| 04/18/2009 | 2.3 | 1.8 | 0.0 | 7.6 |
| 04/27/2009 | 2.4 | 2.3 | 0.0 | 11.6 |
| 04/29/2009 | 2.5 | 2.3 | 0.0 | 11.0 |
| 04/30/2009 | NA | NA | NA | NA |
| 05/01/2009 | 2.4 | 2.2 | 0.0 | 10.4 |
| 05/04/2009 | 12.6 | 21.2 | 0.0 | 86.6 |
| 05/14/2009 | 2.4 | 2.1 | 0.0 | 9.5 |
| 05/23/2009 | 2.4 | 2.1 | 0.0 | 9.5 |

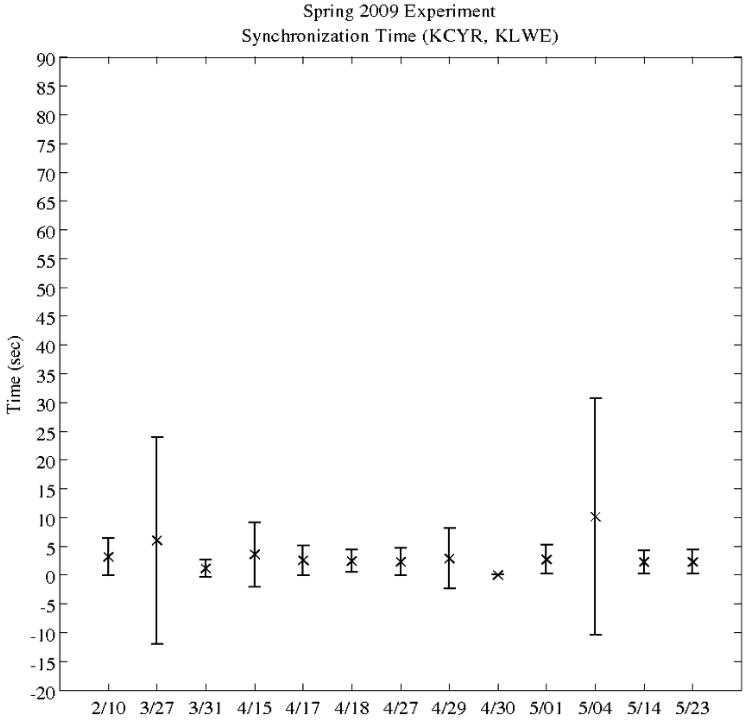

Figure 4.32: Bar chart of the synchronization time between KCYR and KLWE.

Table 4.34: Statistics for synchronization time between KCYR and KLWE

| Date | Mean (sec) | std (sec) | Minimum (sec) | Maximum (sec) |
|---|---|---|---|---|
| 02/10/2009 | 3.1 | 3.3 | 0.0 | 18.9 |
| 03/27/2009 | 6.0 | 18.0 | 0.0 | 97.3 |
| 03/31/2009 | 1.1 | 1.5 | 0.0 | 10.8 |
| 04/15/2009 | 3.5 | 5.6 | 0.0 | 41.0 |
| 04/17/2009 | 2.5 | 2.6 | 0.0 | 14.3 |
| 04/18/2009 | 2.4 | 1.9 | 0.1 | 7.7 |
| 04/27/2009 | 2.3 | 2.4 | 0.0 | 10.4 |
| 04/29/2009 | 2.9 | 5.3 | 0.0 | 60.2 |
| 04/30/2009 | NA | NA | NA | NA |
| 05/01/2009 | 2.7 | 2.5 | 0.0 | 11.8 |
| 05/04/2009 | 10.1 | 20.6 | 0.0 | 86.6 |
| 05/14/2009 | 2.2 | 2.0 | 0.0 | 8.1 |
| 05/23/2009 | 2.3 | 2.1 | 0.0 | 13.8 |

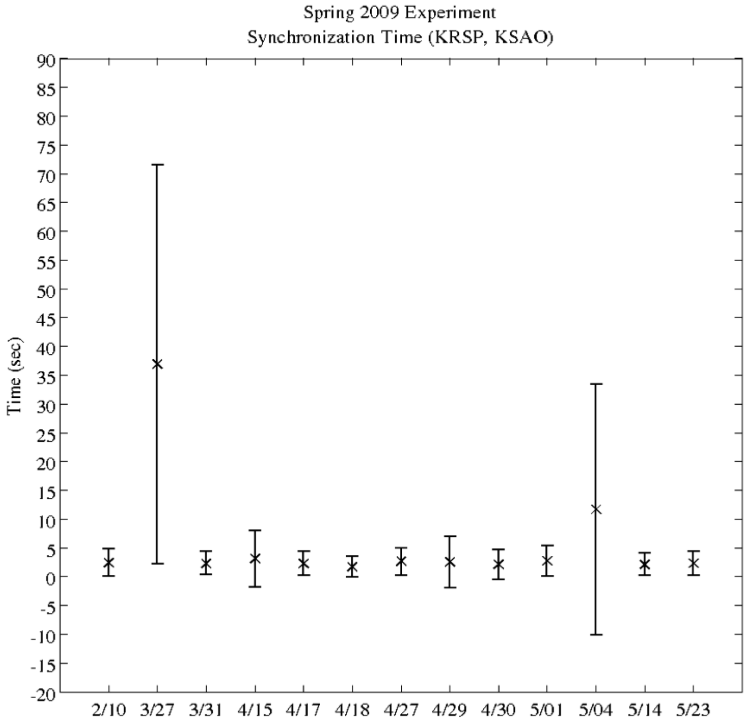

Figure 4.33: Bar chart of the synchronization time between KRSP and KSAO.

Table 4.35: Statistics for synchronization time between KRSP and KSAO

| Date | Mean (sec) | std (sec) | Minimum (sec) | Maximum (sec) |
|---|---|---|---|---|
| 02/10/2009 | 2.5 | 2.4 | 0.0 | 14.3 |
| 03/27/2009 | 36.9 | 34.7 | 0.0 | 97.3 |
| 03/31/2009 | 2.3 | 2.0 | 0.0 | 8.1 |
| 04/15/2009 | 3.1 | 4.9 | 0.0 | 35.7 |
| 04/17/2009 | 2.3 | 2.1 | 0.0 | 9.5 |
| 04/18/2009 | 1.7 | 1.8 | 0.0 | 7.4 |
| 04/27/2009 | 2.6 | 2.4 | 0.0 | 9.5 |
| 04/29/2009 | 2.5 | 4.5 | 0.0 | 60.0 |
| 04/30/2009 | 2.1 | 2.6 | 0.0 | 23.0 |
| 05/01/2009 | 2.7 | 2.6 | 0.0 | 16.7 |
| 05/04/2009 | 11.7 | 21.8 | 0.0 | 78.4 |
| 05/14/2009 | 2.1 | 1.9 | 0.0 | 9.5 |
| 05/23/2009 | 2.3 | 2.1 | 0.0 | 12.1 |

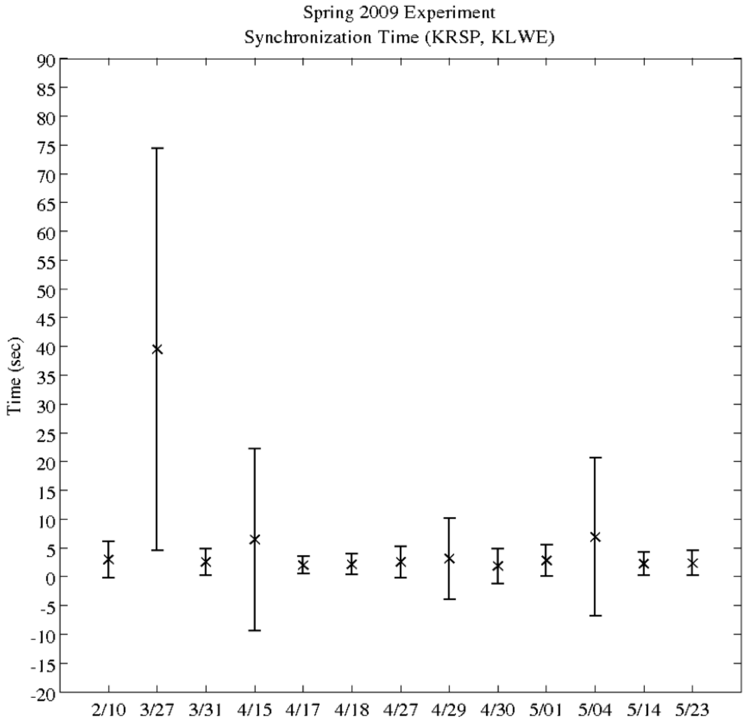

Figure 4.34: Bar chart of the synchronization time between KRSP and KLWE.

Table 4.36: Statistics for synchronization time between KRSP and KLWE

| Date | Mean (sec) | std (sec) | Minimum (sec) | Maximum (sec) |
|---|---|---|---|---|
| 02/10/2009 | 2.9 | 3.1 | 0.0 | 16.2 |
| 03/27/2009 | 39.5 | 34.9 | 0.0 | 97.3 |
| 03/31/2009 | 2.5 | 2.3 | 0.0 | 9.0 |
| 04/15/2009 | 6.4 | 15.8 | 0.0 | 83.4 |
| 04/17/2009 | 2.0 | 1.5 | 0.0 | 6.5 |
| 04/18/2009 | 2.1 | 1.8 | 0.0 | 7.7 |
| 04/27/2009 | 2.6 | 2.7 | 0.0 | 11.6 |
| 04/29/2009 | 3.1 | 7.0 | 0.0 | 62.9 |
| 04/30/2009 | 1.8 | 3.0 | 0.0 | 25.7 |
| 05/01/2009 | 2.8 | 2.7 | 0.0 | 13.4 |
| 05/04/2009 | 6.9 | 13.7 | 0.0 | 55.4 |
| 05/14/2009 | 2.2 | 2.0 | 0.0 | 9.5 |
| 05/23/2009 | 2.3 | 2.2 | 0.0 | 12.4 |

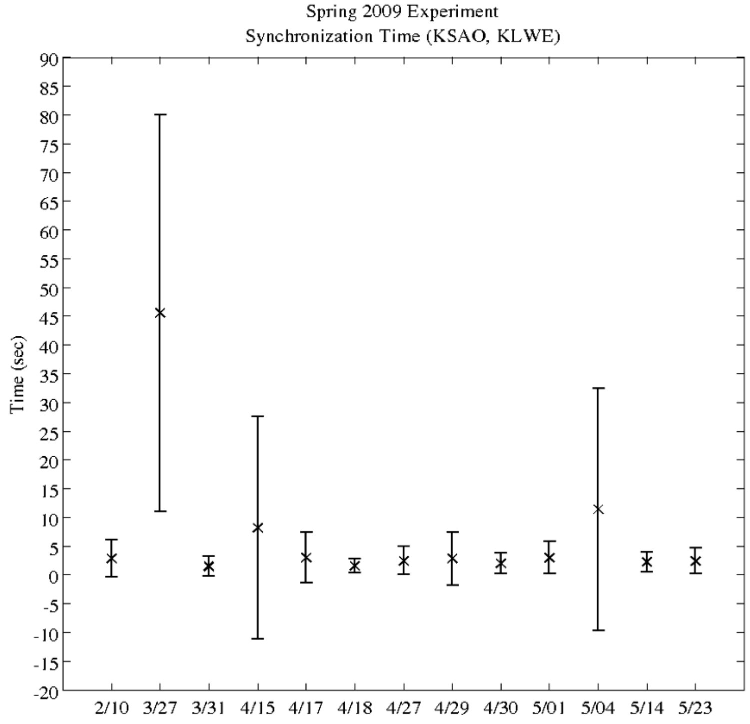

Figure 4.35: Bar chart of the synchronization time between KSAO and KLWE.

Table 4.37: Statistics for synchronization time between KSAO and KLWE

| Date | Mean (sec) | std (sec) | Minimum (sec) | Maximum (sec) |
|---|---|---|---|---|
| 02/10/2009 | 2.9 | 3.2 | 0.0 | 18.9 |
| 03/27/2009 | 45.5 | 34.5 | 0.0 | 97.3 |
| 03/31/2009 | 1.5 | 1.8 | 0.0 | 8.1 |
| 04/15/2009 | 8.2 | 19.3 | 0.0 | 89.7 |
| 04/17/2009 | 3.0 | 4.4 | 0.0 | 14.3 |
| 04/18/2009 | 1.6 | 1.2 | 0.0 | 3.7 |
| 04/27/2009 | 2.5 | 2.5 | 0.0 | 10.4 |
| 04/29/2009 | 2.8 | 4.6 | 0.0 | 40.1 |
| 04/30/2009 | 2.0 | 1.8 | 0.0 | 7.4 |
| 05/01/2009 | 3.0 | 2.8 | 0.0 | 12.2 |
| 05/04/2009 | 11.4 | 21.1 | 0.0 | 73.2 |
| 05/14/2009 | 2.2 | 1.7 | 0.0 | 9.0 |
| 05/23/2009 | 2.4 | 2.2 | 0.0 | 10.8 |

when the beam synchronization time exceeds the heartbeat time, i.e. May 4, 2009. These instances are associated with network latencies since the synchronization time is measured as the time that the netCDF files are created on the SOCC.

### 4.2.2 Detailed Analysis of April 2, 2010 Case

On April 2, 2010 a linear thunderstorm was observed in the IP1 network from 08:27 UTC until 13:42 UTC. This thunderstorm had a circulation feature at about 10:58 UTC and lasted until 11:03 UTC. Figure 4.36 shows the track of the circulation in the IP1 network from 10:58 UTC until 11:03 UTC. From figure 4.36 it is clear that the circulation is located in the quad-Doppler region of the IP1 network, and is well covered by each dual-Doppler pair for its lifespan. During the time frame of the circulation, significant attenuation was observed in the dual-Doppler regions formed by Lawton (KLWE) and KRSP, and the region formed by KLWE and KSAO. Also during the time the vortex was observed, Cyril (KCYR) did not generate data at the radar. When not considering attenuation and the data outage from KCYR, then of the six pairs, the best pairs for dual-Doppler retrieval are (KCYR, KLWE) from 10:58 to 10:59, and (KCYR, KSAO) from 11:00 to 11:03. Therefore KCYR, KLWE, and

KSAO were tasked to scan for dual-Doppler. Figure 4.37 shows the regions of the best dual-Doppler pairs with the location of the circulation. When the data outage is considered, then the possible pairs available for dual-Doppler retrievals are (KSAO, KRSP), (KSAO, KLWE), and (KRSP, KLWE).

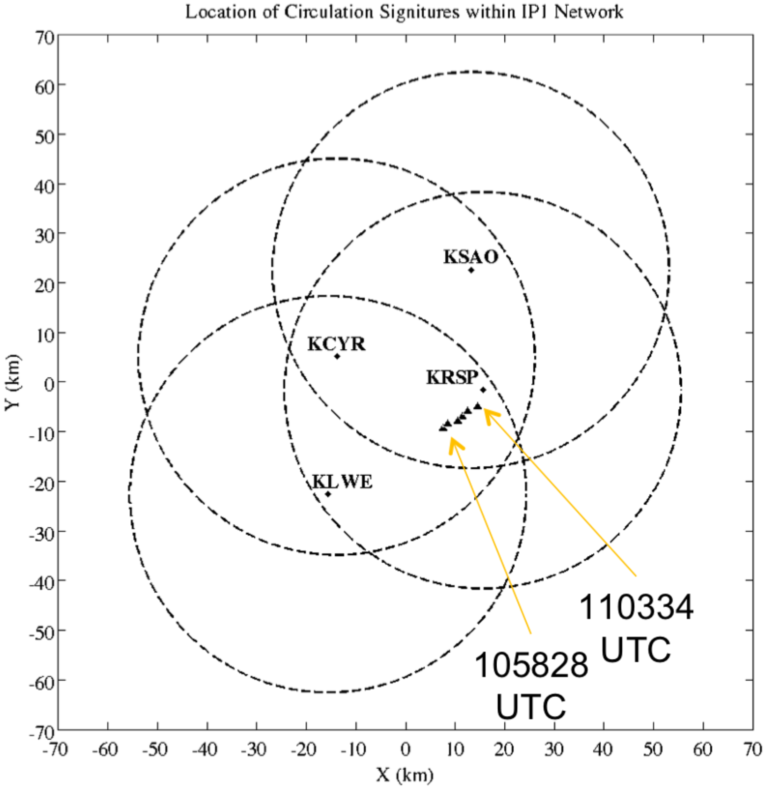

Figure 4.36: Location of circulation from 10:58 UTC to 11:03 UTC.

The attenuation in each dual-Doppler region can be inferred from the corrected reflectivity for each radar and corrected reflectivity composites for each pair and the IP1 network. Figure 4.38, 4.39, and 4.40 show the corrected reflectivity at 10:59 UTC for KRSP, KLWE and KSAO, respectively. In figure 4.38 attenuation can be seen on the southwestern edge of the storm. In the image in figure 4.39 attenuation was observed in the northeastern quadrant of the storm, and in figure 4.40 attenuation is noticeable in the southwestern region of the storm. Figure 4.41 shows the composite corrected reflectivity for the pair (KRSP, KLWE), figure 4.42 shows the composite

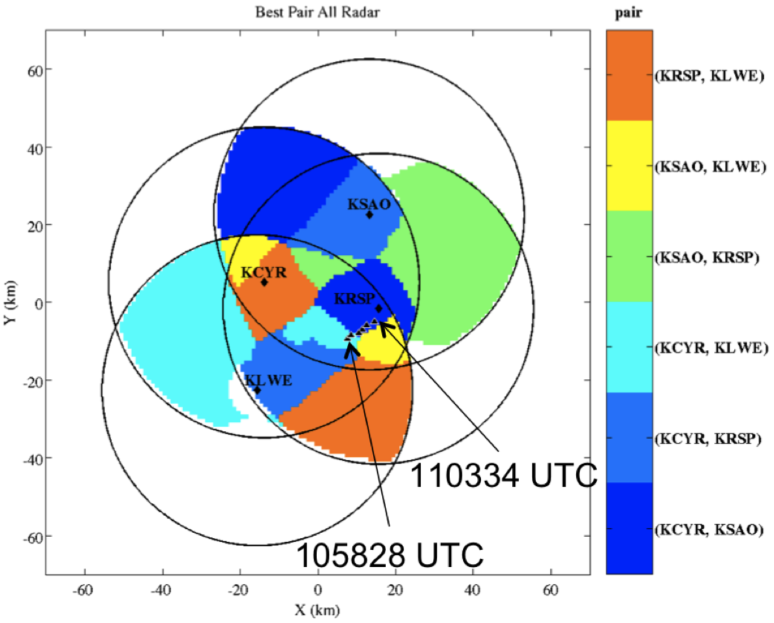

Figure 4.37: Location of circulation in best pair regions from 10:58 UTC to 11:03 UTC.

corrected reflectivity for (KRSP, KSAO), figure 4.43 shows the composite corrected reflectivity for the pair (KSAO, KLWE), and figure 4.44 shows the composite corrected reflectivity for the entire IP1 network. From the composite corrected reflectivity plots it is clear that there is significant attenuation in the dual-Doppler regions. For this case the attenuation was high enough that no velocity estimates existed in the regions of attenuation. The attenuation in the dual-Doppler regions affected the topology of the best pair regions, and which radar pairs can be used to retrieve the wind field around the circulation feature.

Both signal to noise ratio (SNR) and attenuation are used to objectively determine which radars should be tasked for dual-Doppler. A completely extinct signal is characterized by having been attenuated and having a low SNR. In some cases a signal might be attenuated but still have a sufficient SNR for moment estimation. For instance a SNR greater than 5 dB is sufficient for estimating radial velocity (Bringi and Chandrasekar, 2001). SNR was computed for each dual-Doppler region. Any gate with an SNR greater than 5 dB was removed. Attenuation in the dual-Doppler

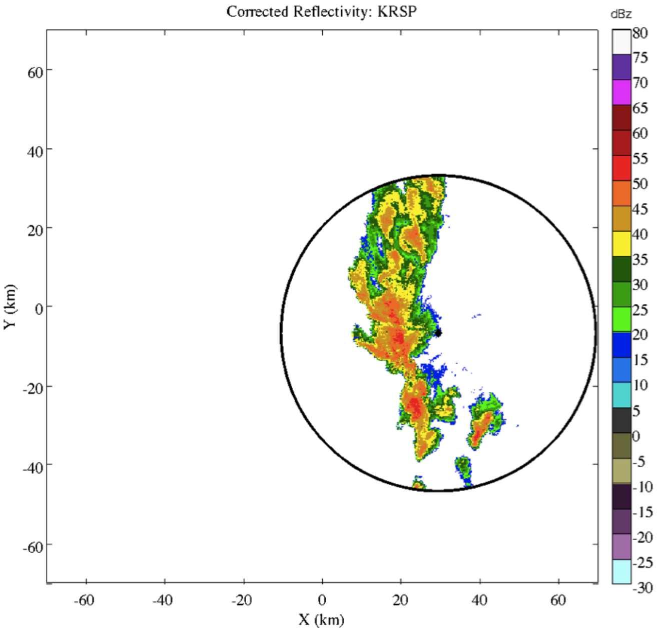

Figure 4.38: Corrected reflectivity for KRSP for April 2, 2010 at 10:59 UTC

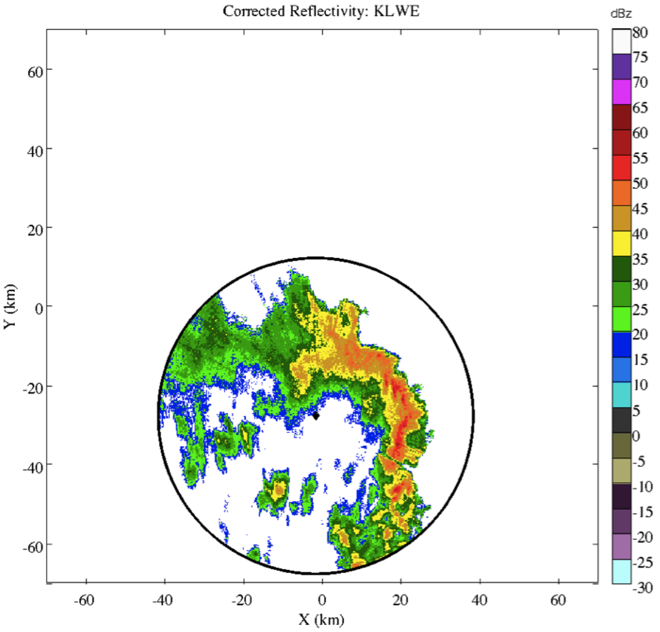

Figure 4.39: Corrected reflectivity for KLWE for April 2, 2010 at 10:59 UTC

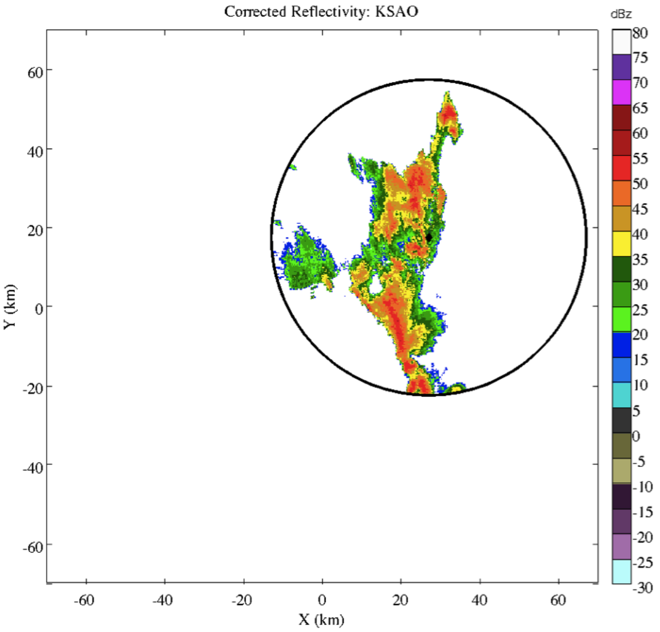

Figure 4.40: Corrected reflectivity for KSAO for April 2, 2010 at 10:59 UTC

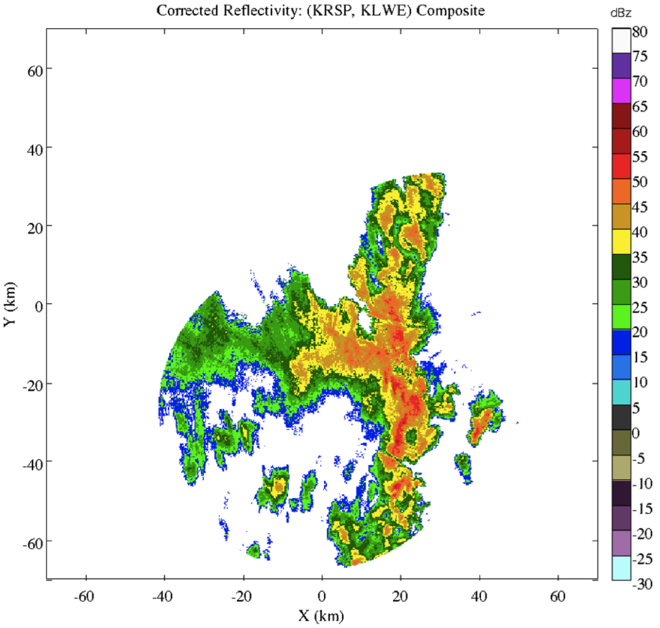

Figure 4.41: Composite reflectivity for (KRSP, KLWE) for April 2, 2010 at 10:59 UTC

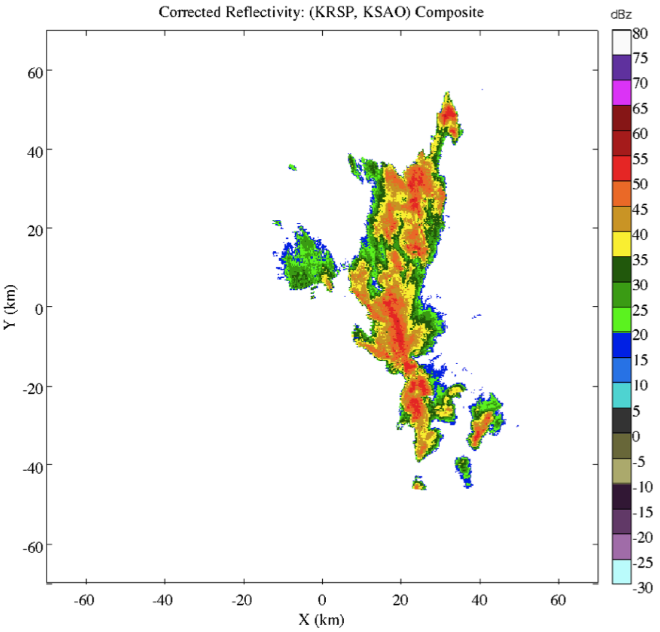

Figure 4.42: Composite reflectivity for (KRSP, KSAO) for April 2, 2010 at 10:59 UTC

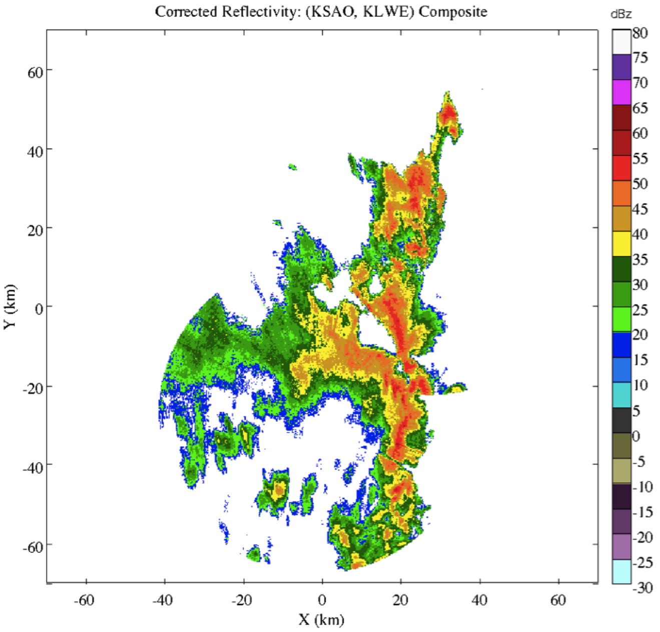

Figure 4.43: Composite reflectivity for (KSAO, KLWE) for April 2, 2010 at 10:59 UTC

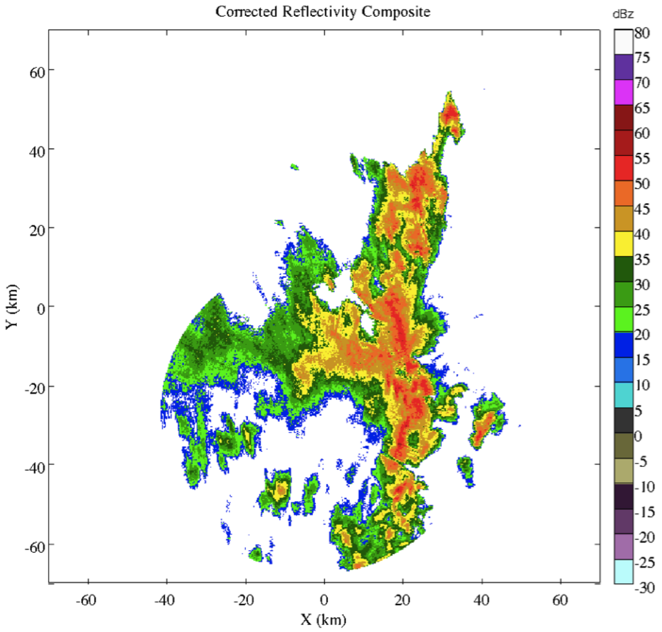

Figure 4.44: Composite reflectivity for April 2, 2010 at 10:59 UTC

regions was computed by subtracting the uncorrected reflectivity from the corrected reflectivity. Gates with an attenuation greater than 15 dB were retained. A threshold of 15 dB was selected based on the X-band attenuation statistics provided in Chandrasekar et al. (2009). Gates that had both an SNR less than 5 dB and an attenuation greater than 15 dB where retained. The gates remaining were considered the attenuated gates in the dual-Doppler region.

For the dual-Doppler region formed by the pair (KRSP, KLWE), figure 4.45 shows the attenuation from the KRSP and figure 4.46 shows the attenuation from KLWE. Figures 4.47 and 4.48 show the SNR for KRSP and KLWE, respectively. Both radars, KRSP and KLWE, have significant attenuation in the dual-Doppler region, and the SNR for both radars is well below the 5 dB threshold. Making the region unusable for dual-Doppler retrievals. For the dual-Doppler region formed by the pair (KRSP, KSAO), figure 4.49 and 4.50 give the attenuation for KRSP and KSAO, respectively. The SNR for KRSP and KSAO are given in figure 4.51 and 4.52. From the figures it is clear that there is little attenuation in the dual-Doppler region formed by KRSP and

KSAO. Which makes the pair usable for dual-Doppler retrievals. Figure 4.53 and 4.54 show the attenuation for KSAO and KLWE for the dual-Doppler region formed by KSAO and KLWE. Figure 4.55 and 4.56 shows the SNR for KSAO and KLWE. The pair (KSAO, KLWE) is also unusable since there is significant attenuation for both radars in the pair.

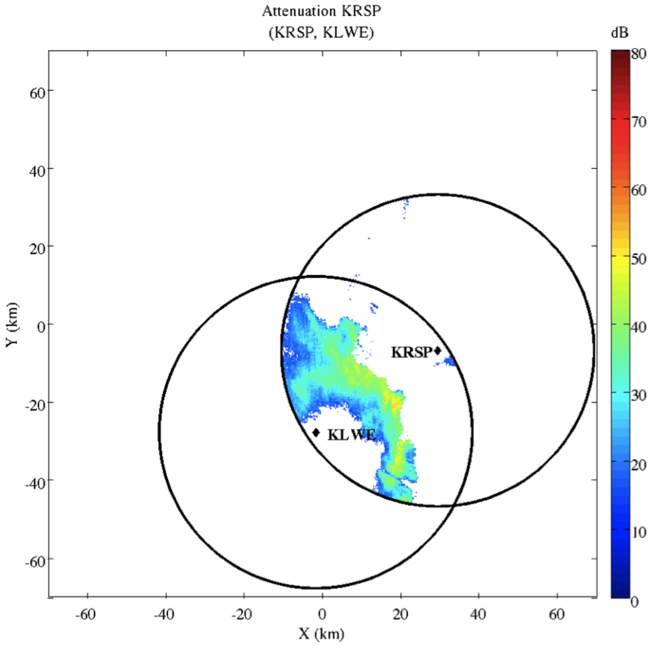

Figure 4.45: Attenuation for KRSP in the pair (KRSP, KLWE) for April 2, 2010 at 10:59 UTC

The pairs that have the most significant attenuation are those that are formed with KLWE. Therefore KLWE would be removed from the dual-Doppler optimization. It is noted that both KRSP and KSAO had significant attenuation when paired with KLWE, but where not removed since the pair formed by the two radars had minimal attenuation and was still usable for wind field retrievals. Removing KLWE from the scan optimization leaves only the pair formed by KRSP and KSAO. Attenuation also needed to be taken into account during the retrieval process. In this case the retrieval could only be performed with the pair (KRSP, KSAO). The location of the circulation resided mostly in the 20° beam crossing region. This fact was taken into

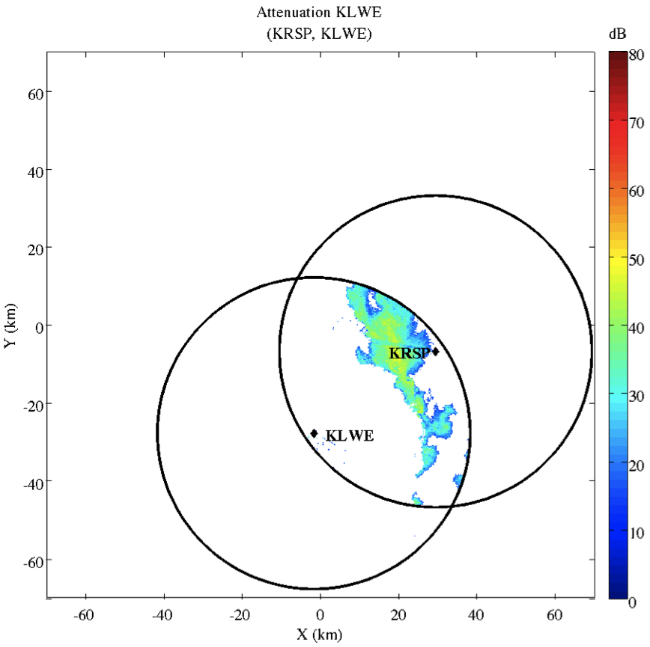

Figure 4.46: Attenuation for KLWE in the pair (KRSP, KLWE) for April 2, 2010 at 10:59 UTC

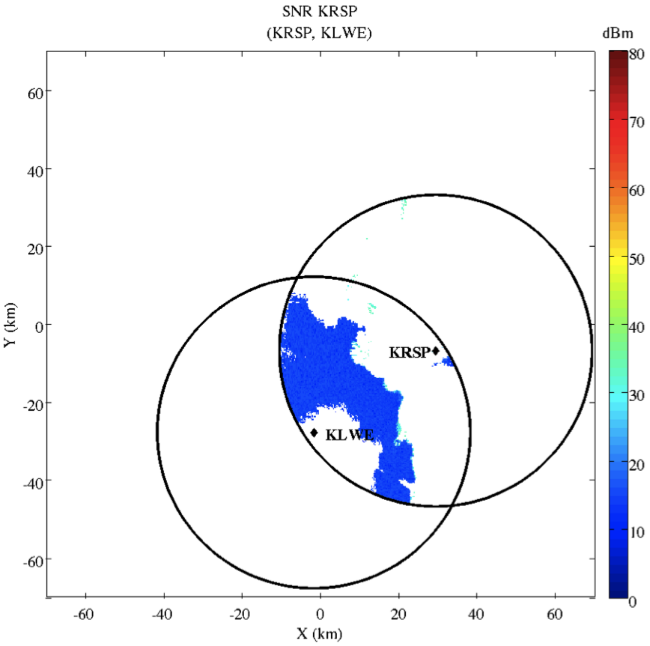

Figure 4.47: SNR for KRSP in the pair (KRSP, KLWE) for April 2, 2010 at 10:59 UTC

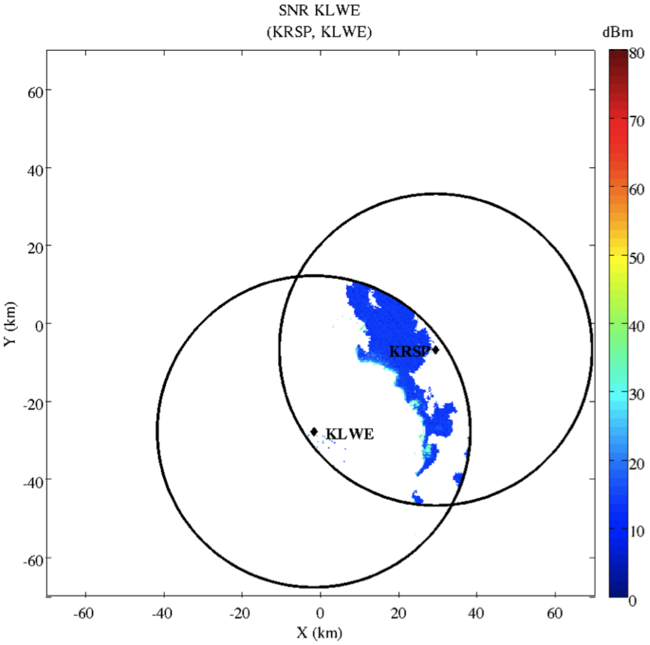

Figure 4.48: SNR for KLWE in the pair (KRSP, KLWE) for April 2, 2010 at 10:59 UTC

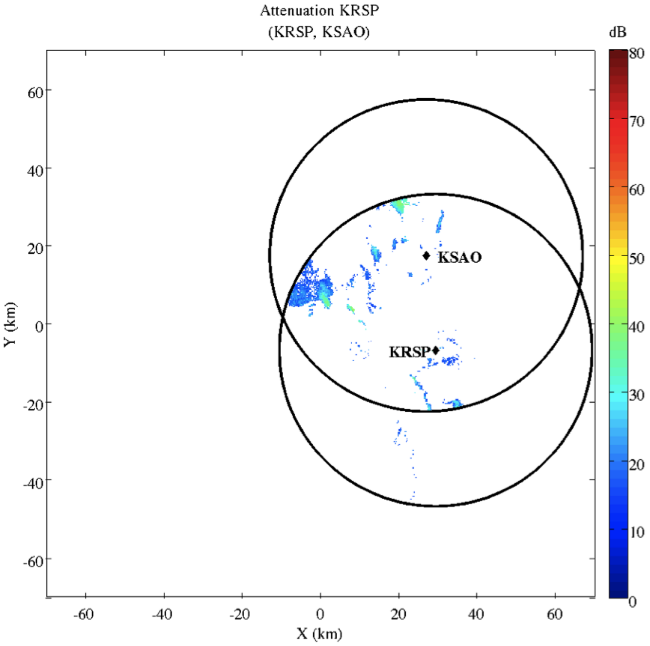

Figure 4.49: Attenuation for KRSP in the pair (KRSP, KSAO) for April 2, 2010 at 10:59 UTC

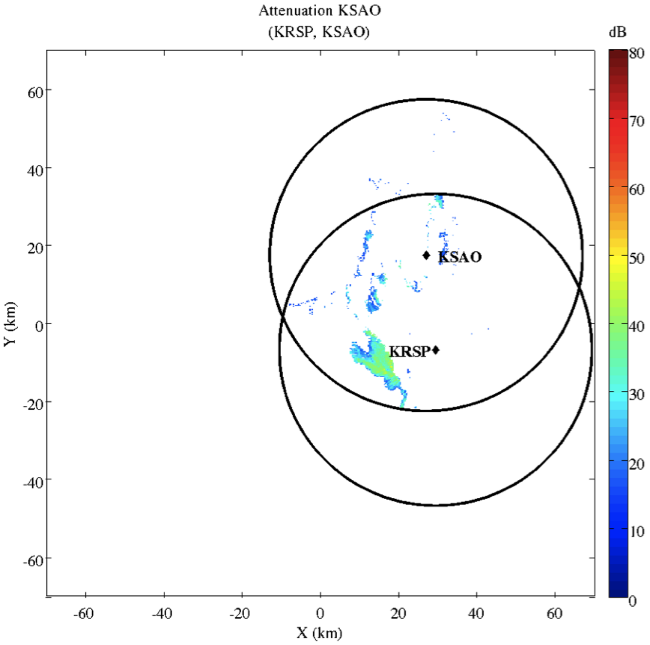

Figure 4.50: Attenuation for KSAO in the pair (KRSP, KSAO) for April 2, 2010 at 10:59 UTC

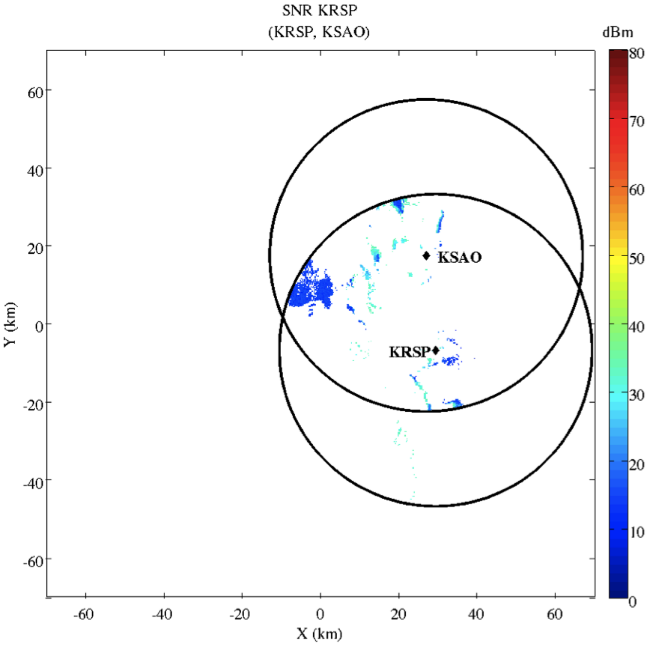

Figure 4.51: SNR for KRSP in the pair (KRSP, KSAO) for April 2, 2010 at 10:59 UTC

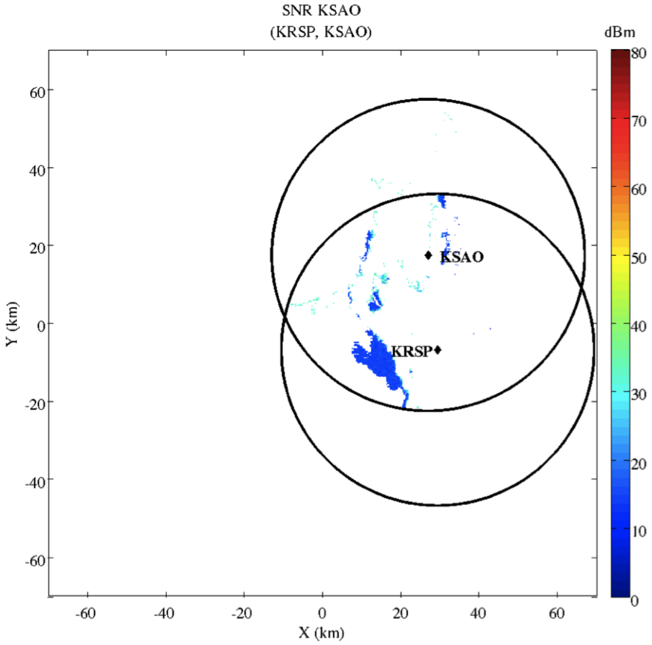

Figure 4.52: SNR for KRSP in the pair (KRSP, KSAO) for April 2, 2010 at 10:59 UTC

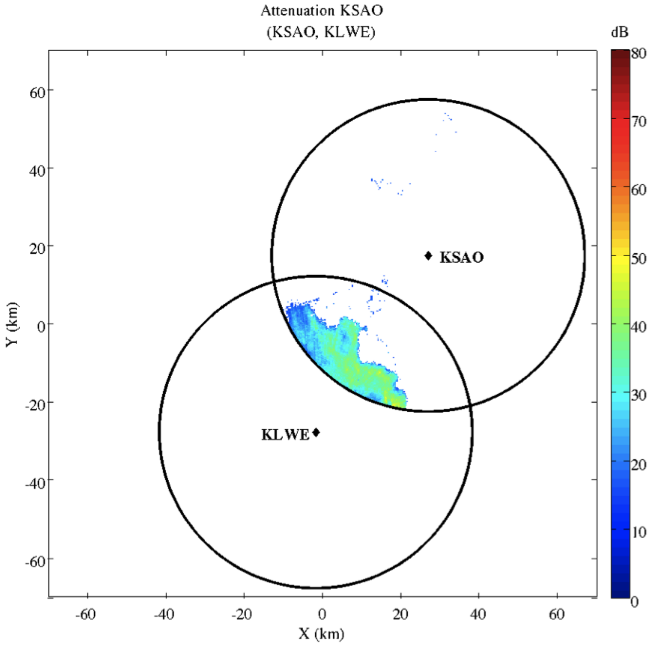

Figure 4.53: Attenuation for KSAO in the pair (KSAO, KLWE) for April 2, 2010 at 10:59 UTC

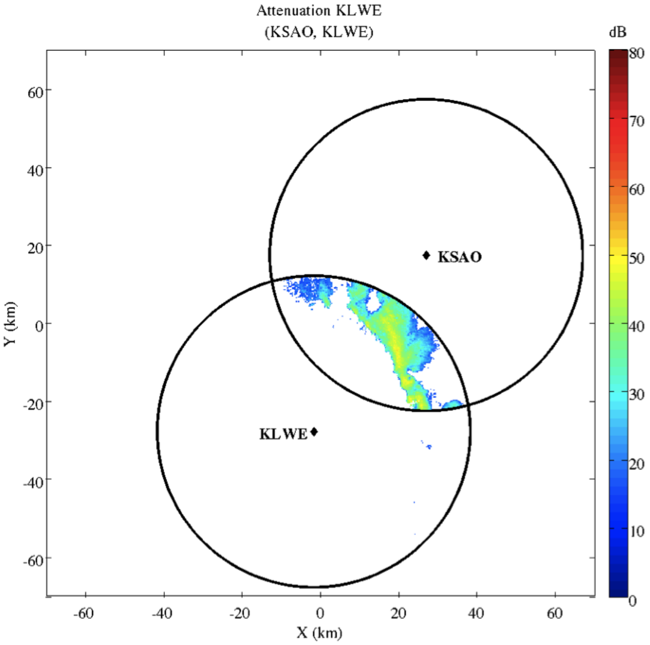

Figure 4.54: Attenuation for KLWE in the pair (KSAO, KLWE) for April 2, 2010 at 10:59 UTC

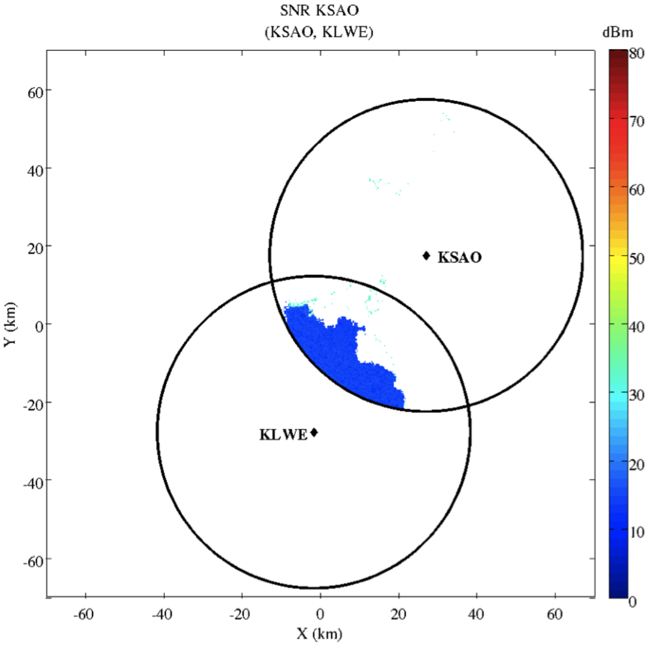

Figure 4.55: SNR for KSAO in the pair (KSAO, KLWE) for April 2, 2010 at 10:59 UTC

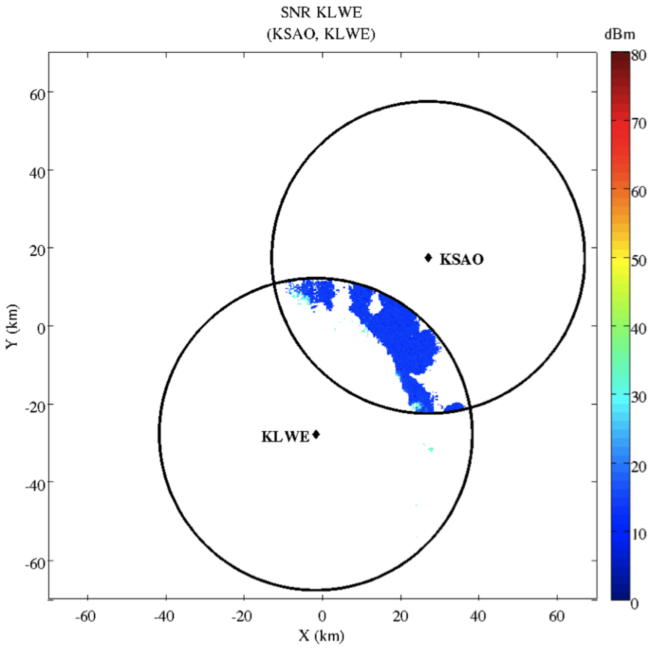

Figure 4.56: SNR for KLWE in the pair (KSAO, KLWE) for April 2, 2010 at 10:59 UTC

account when performing the dual-Doppler retrievals. Figure 4.57 shows a sequence (10:55 UTC to 11:02 UTC) of the retrieved wind field after attenuation and radar outages were considered.

More general best pair regions for when a radar is removed from the scan strategy optimization are given in figure 4.58, figure 4.62, figure 4.60, and figure 4.64. Figure 4.58 shows the best dual-Doppler pair regions when KCYR is removed from the scan strategy optimization, figure 4.60 shows the best dual-Doppler pair regions when KSAO is removed, figure 4.62 shows the best dual-Doppler pair region when KRSP is removed and figure 4.64 show the best dual-Doppler pair region when KLWE is removed. Figure 4.59 shows the dual-Doppler coverage for when KCYR is removed from the optimization, figure 4.61 shows the dual-Doppler coverage when KSAO is removed, figure 4.63 shows the dual-Doppler coverage when KRSP is removed, and figure 4.65 shows the dual-Doppler coverage when KLWE is removed. If two radars are removed from the optimization then best dual-Doppler pair is that formed by

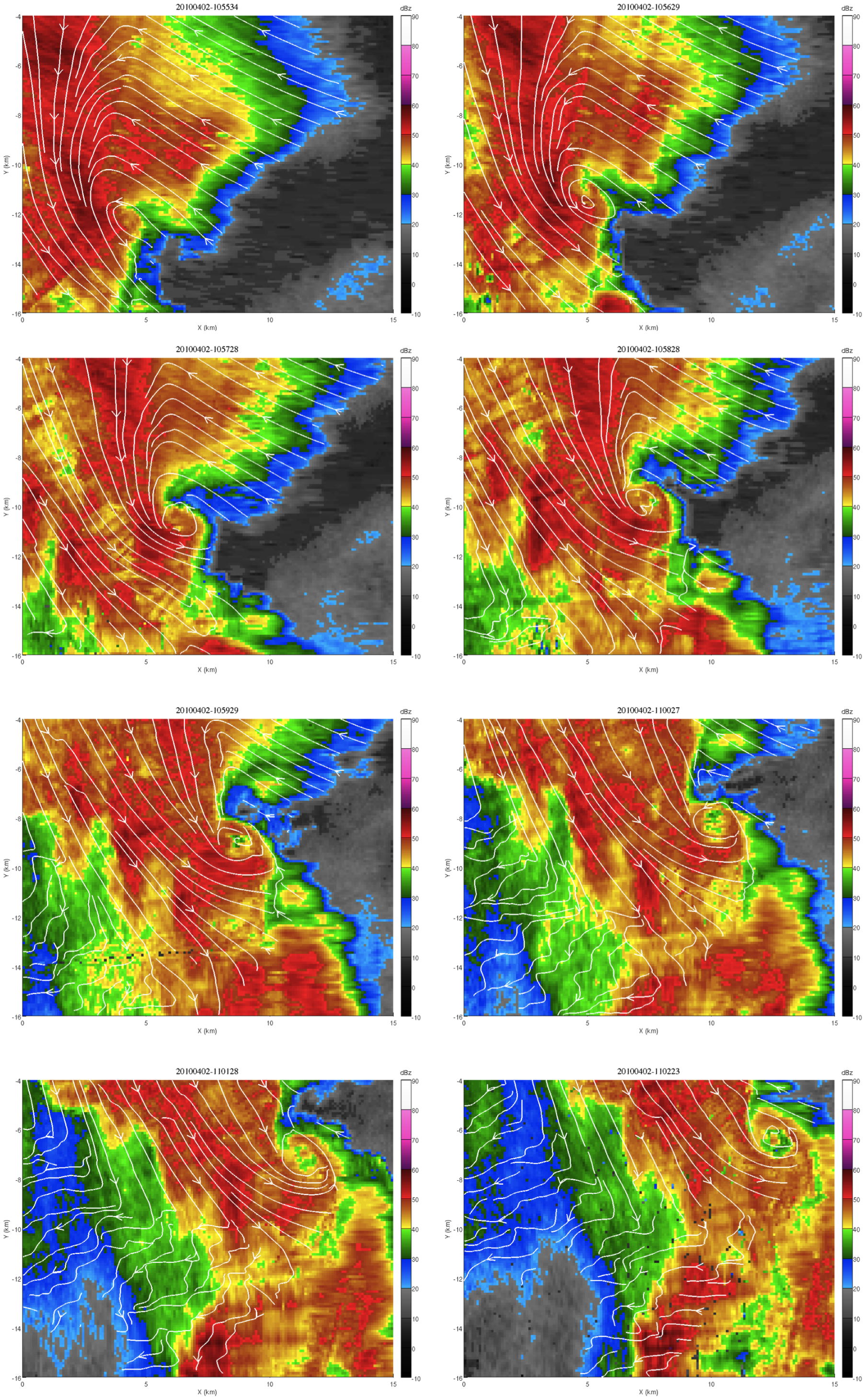

Figure 4.57: Retrieved wind field from severe wind event observed on April 2, 2010.

the remaining two radars. If three radars are removed then no pairs are left for dual-Doppler retrievals.

From the significant analysis of the April 2, 2010 event, it is evident that the current system rules do not account for attenuation in the dual-Doppler regions. It was shown that attenuation will change the topology of the best pair regions of the IP1 network and that the best pair for wind field retrievals will also be affected. The system rules for the scan strategy optimization are unable to adapt to the changes in the number of pairs available in the network. By providing the system with a new set of rules that adapt to changes number of dual-Doppler pairs in the IP1 network, the scan strategy optimization can adopt new best pair regions that reflect those changes. Thus, making it possible to retrieve the greatest amount of information from the available data.

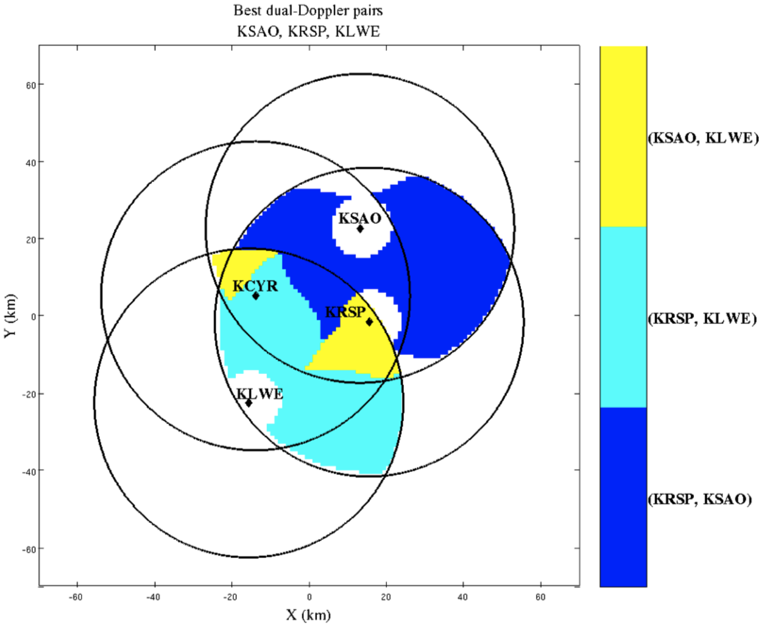

Figure 4.58: Best pair region when KCYR is removed.

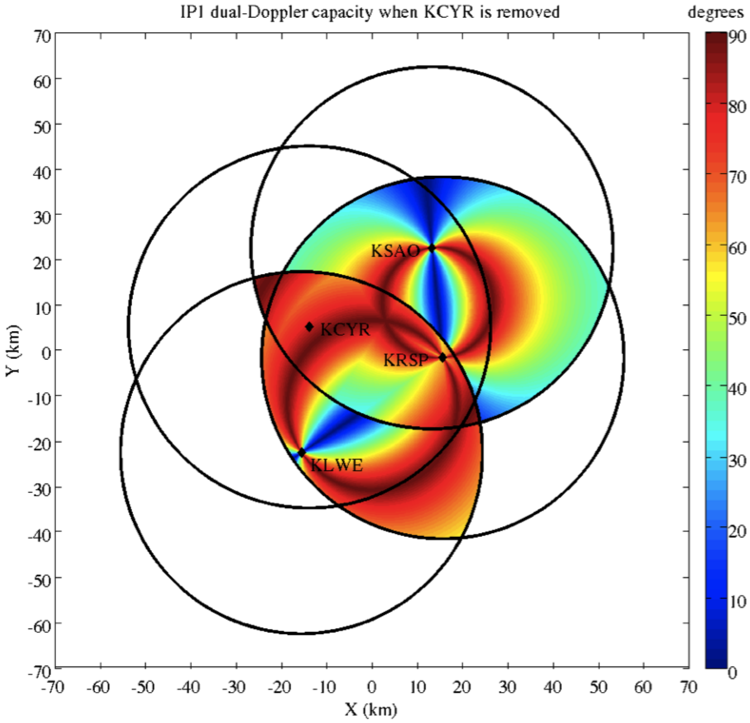

Figure 4.59: Dual-Doppler capacity when KCYR is removed.

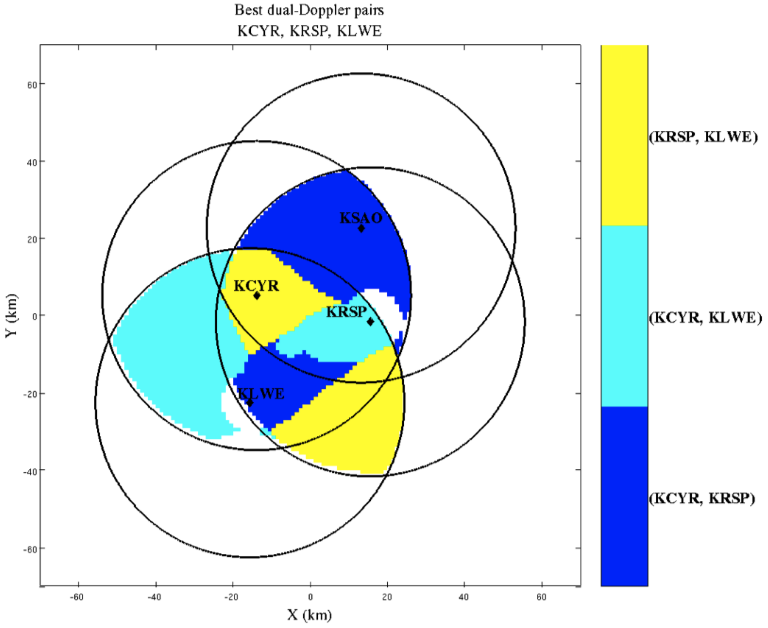

Figure 4.60: Best pair region when KSAO is removed.

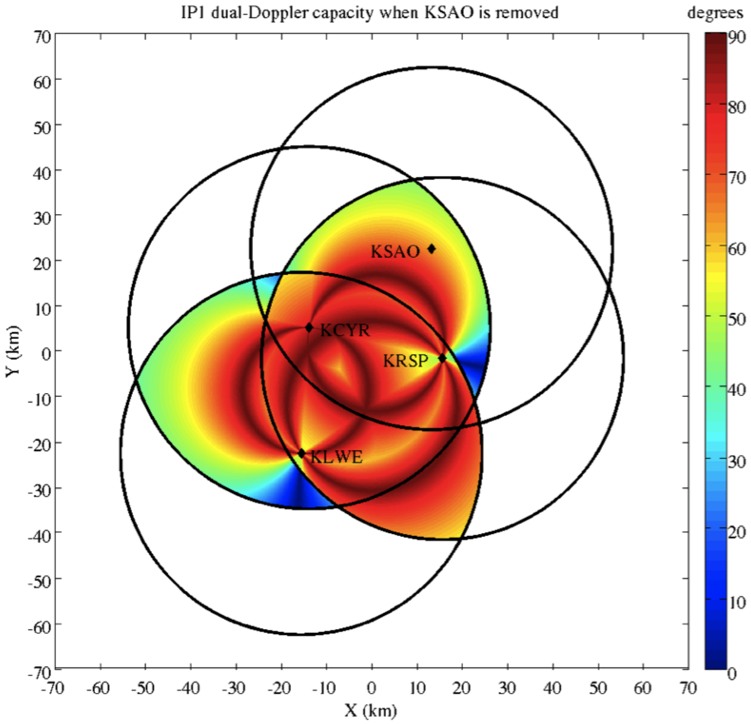

Figure 4.61: Dual-Doppler capacity when KSAO is removed.

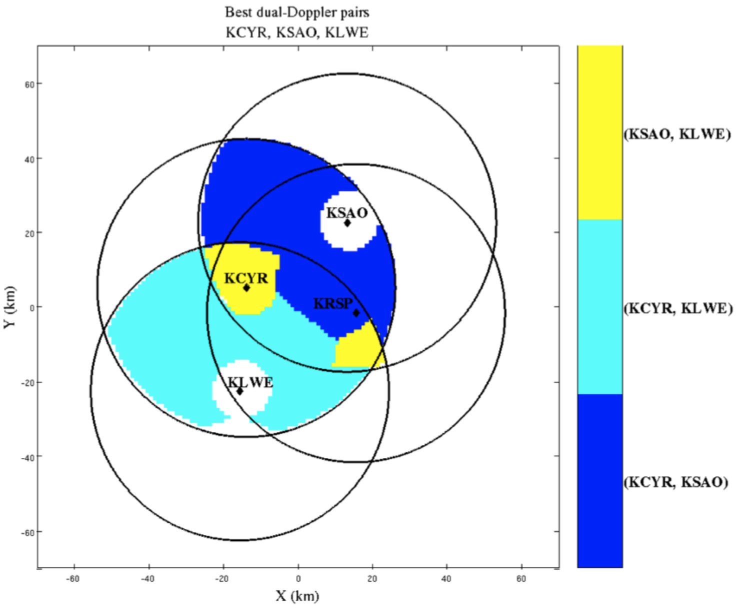

Figure 4.62: Best pair region when KRSP is removed.

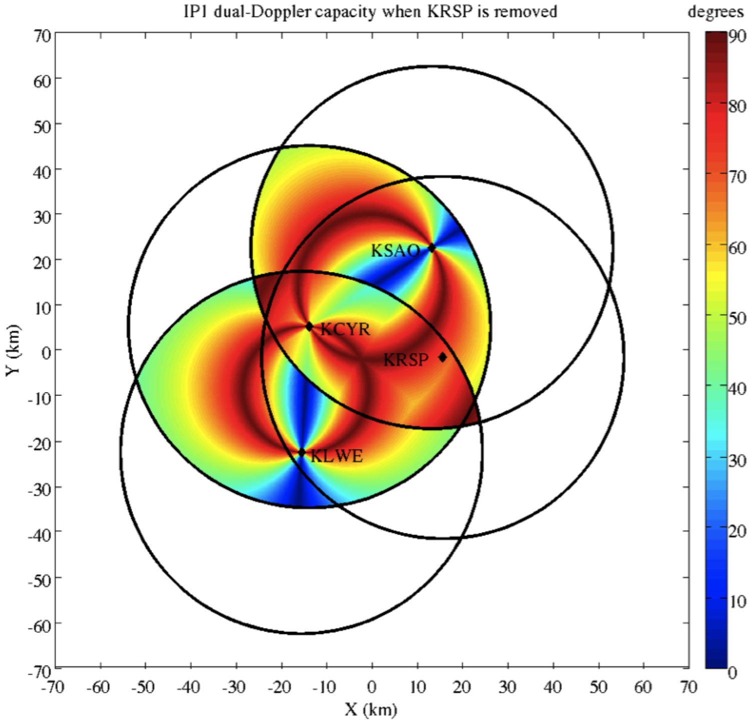

Figure 4.63: Dual-Doppler capacity when KRSP is removed.

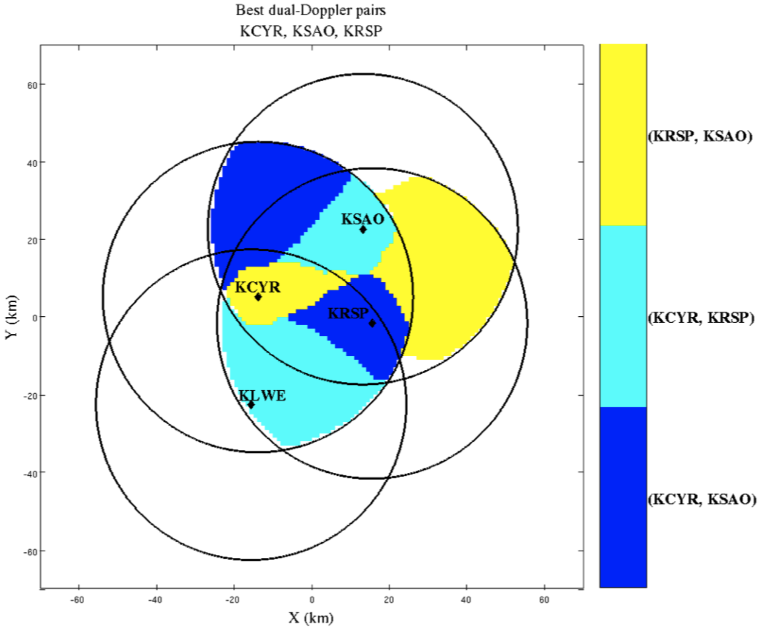

Figure 4.64: Best pair region when KLWE is removed.

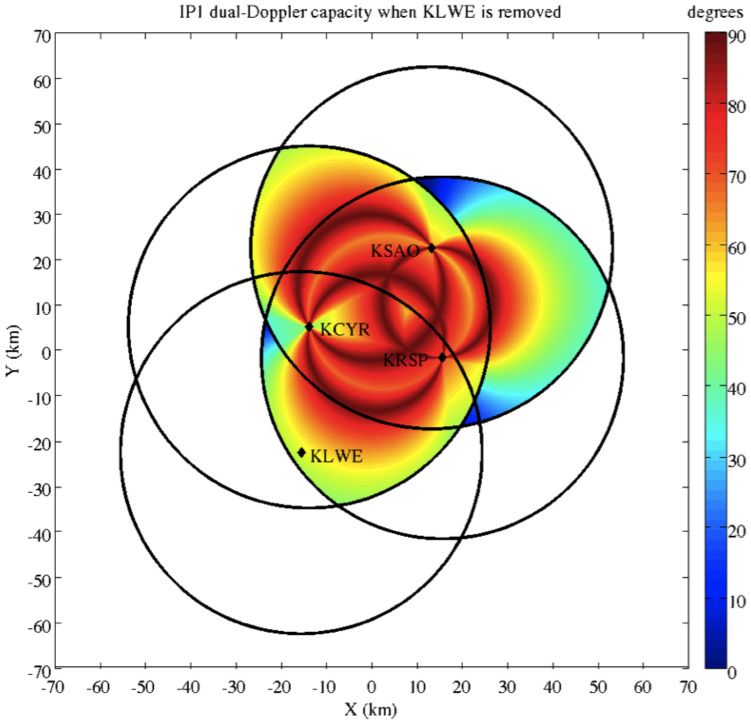

Figure 4.65: Dual-Doppler capacity when KLWE is removed.

## 4.3 Evaluation of Dual-Doppler Retrievals

In order to assess the quality of the retrieved wind field, the retrieved wind fields from the 2009 spring experiment were analyzed. An additional case was studied in order to evaluate the quality of the merged wind field in a severe weather event. Section 4.3.1 gives results for the quality of the wind field retrieval for the 2009 spring experiment, and section 4.3.2 gives the results for the quality of the wind field retrieval for an EF2 tornado observed by the CASA IP1 network on May 14, 2009.

### 4.3.1 2009 Spring Experiment

For each event the normalized variance was computed at each valid grid point at seven different altitudes. The altitudes selected are 0.0 kilometers, 0.5 kilometeres, 1.0 kilometers, 1.5 kilometers, 2.0 kilometers, 2.5 kilometers, and 3.0 kilometers. These altitudes were selected since CASA aims to increase coverage in the lowest part of the troposphere. Figure 4.66 - figure 4.72 give bar charts for the 0.0 kilometer to 3.0 kilometer altitudes in 0.5 kilometer intervals, and table 4.38 - table 4.44 summarizes the statistics for the figures. From these results on average the mean retrieval error of the wind field at the three lowest kilometers of the atmosphere are between 1.0 m/s to 1.5 m/s, and never exceeds an error of 1.5 m/s. Therefore it can be assumed that for an arbitrary event the average error in the retrieval will be between 1.0 m/s and 1.5 m/s. This error is slightly greater then the error in the radial velocity estimate, however this is sufficient for wind field retrievals.

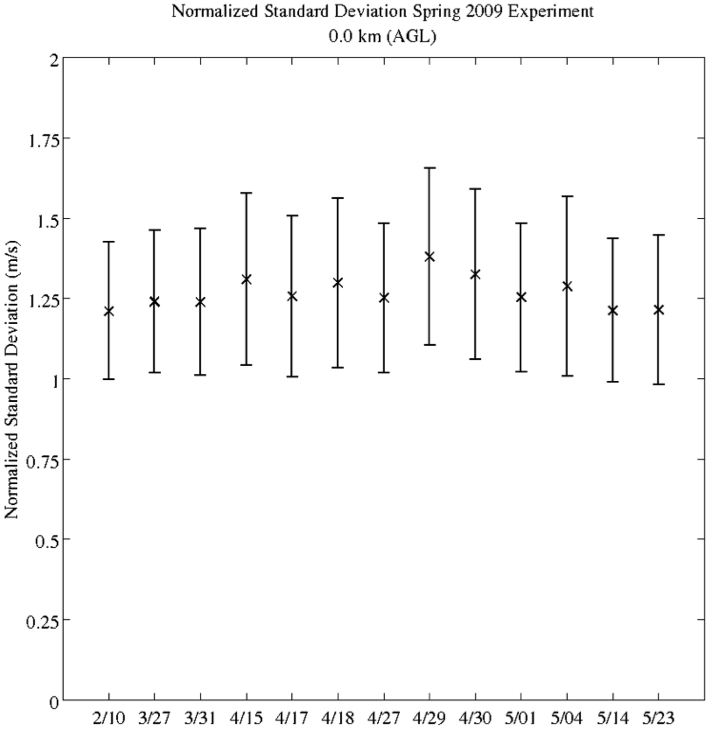

Figure 4.66: Bar chart for dual-Doppler normalized standard deviation at 0.0km AGL.

### 4.3.2 Detailed Analysis of May 14, 2009

On May 14, 2009 an EF2 tornado was observed in the IP1 network (Chandrasekar et al., 2010b). The tornado developed near Gracemont, Ok, and moved south along

Table 4.38: Statistics for normalized standard deviation at an altitude of 0.0km AGL

| Date | Mean (m/s) | std (m/s) | Minimum (m/s) | Maximum (m/s) |
|---|---|---|---|---|
| 02/10/2009 | 1.2 | 0.2 | 1.0 | 2.0 |
| 03/27/2009 | 1.2 | 0.2 | 1.0 | 2.0 |
| 03/31/2009 | 1.2 | 0.2 | 1.0 | 2.0 |
| 04/15/2009 | 1.3 | 0.3 | 1.0 | 2.0 |
| 04/17/2009 | 1.3 | 0.3 | 1.0 | 2.0 |
| 04/18/2009 | 1.3 | 0.3 | 1.0 | 2.0 |
| 04/27/2009 | 1.3 | 0.2 | 1.0 | 2.0 |
| 04/29/2009 | 1.4 | 0.3 | 1.0 | 2.0 |
| 04/30/2009 | 1.3 | 0.3 | 1.0 | 2.0 |
| 05/01/2009 | 1.3 | 0.2 | 1.0 | 2.0 |
| 05/04/2009 | 1.3 | 0.3 | 1.0 | 2.0 |
| 05/14/2009 | 1.2 | 0.2 | 1.0 | 2.0 |
| 05/23/2009 | 1.2 | 0.2 | 1.0 | 2.0 |

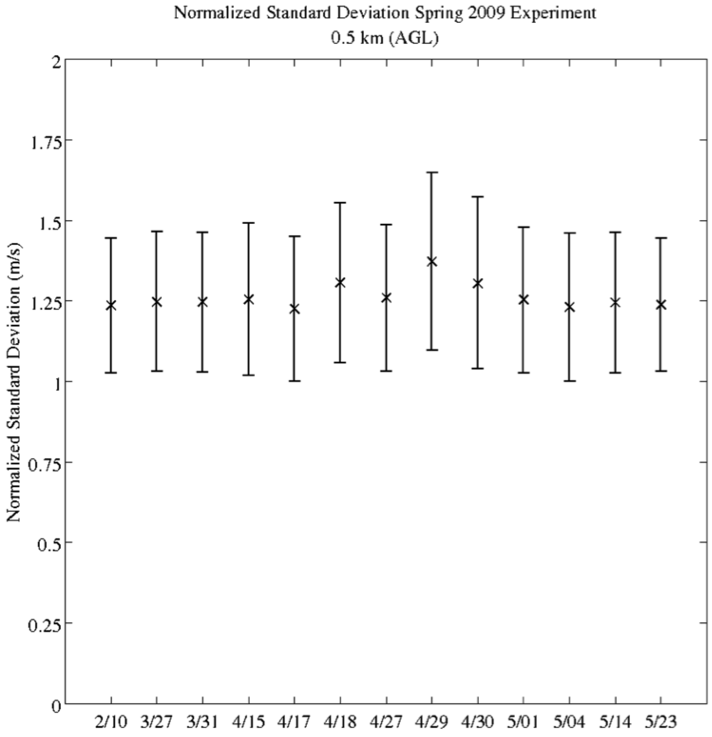

Figure 4.67: Bar chart for normalized standard deviation at 0.5km AGL.

Table 4.39: Statistics for normalized standard deviation at an altitude of 0.5km AGL

| Date | Mean (m/s) | std (m/s) | Minimum (m/s) | Maximum (m/s) |
|---|---|---|---|---|
| 02/10/2009 | 1.2 | 0.2 | 1.0 | 2.0 |
| 03/27/2009 | 1.2 | 0.2 | 1.0 | 2.0 |
| 03/31/2009 | 1.2 | 0.2 | 1.0 | 2.0 |
| 04/15/2009 | 1.3 | 0.2 | 1.0 | 2.0 |
| 04/17/2009 | 1.2 | 0.2 | 1.0 | 2.0 |
| 04/18/2009 | 1.3 | 0.2 | 1.0 | 2.0 |
| 04/27/2009 | 1.3 | 0.2 | 1.0 | 2.0 |
| 04/29/2009 | 1.4 | 0.3 | 1.0 | 2.0 |
| 04/30/2009 | 1.3 | 0.3 | 1.0 | 2.0 |
| 05/01/2009 | 1.3 | 0.2 | 1.0 | 2.0 |
| 05/04/2009 | 1.2 | 0.2 | 1.0 | 2.0 |
| 05/14/2009 | 1.2 | 0.2 | 1.0 | 2.0 |
| 05/23/2009 | 1.2 | 0.2 | 1.0 | 2.0 |

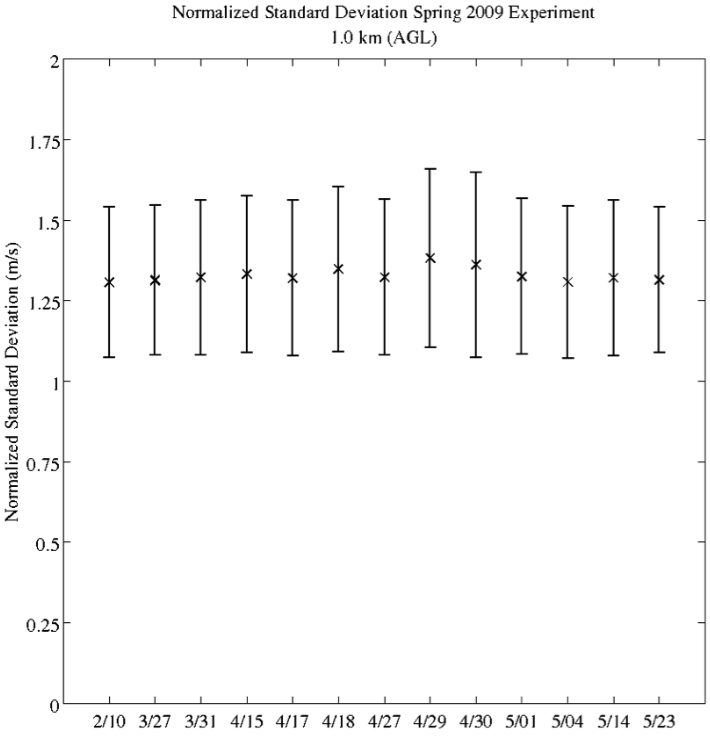

Figure 4.68: Bar chart for normalized standard deviation at 1.0km AGL.

Table 4.40: Statistics for normalized standard deviation at an altitude of 1.0km AGL

| Date | Mean (m/s) | std (m/s) | Minimum (m/s) | Maximum (m/s) |
|---|---|---|---|---|
| 02/10/2009 | 1.3 | 0.2 | 1.0 | 2.0 |
| 03/27/2009 | 1.3 | 0.2 | 1.0 | 2.0 |
| 03/31/2009 | 1.3 | 0.2 | 1.0 | 2.0 |
| 04/15/2009 | 1.3 | 0.2 | 1.0 | 2.0 |
| 04/17/2009 | 1.3 | 0.2 | 1.0 | 2.0 |
| 04/18/2009 | 1.3 | 0.3 | 1.0 | 2.0 |
| 04/27/2009 | 1.3 | 0.2 | 1.0 | 2.0 |
| 04/29/2009 | 1.4 | 0.3 | 1.0 | 2.0 |
| 04/30/2009 | 1.4 | 0.3 | 1.0 | 2.0 |
| 05/01/2009 | 1.3 | 0.2 | 1.0 | 2.0 |
| 05/04/2009 | 1.3 | 0.2 | 1.0 | 2.0 |
| 05/14/2009 | 1.3 | 0.2 | 1.0 | 2.0 |
| 05/23/2009 | 1.3 | 0.2 | 1.0 | 2.0 |

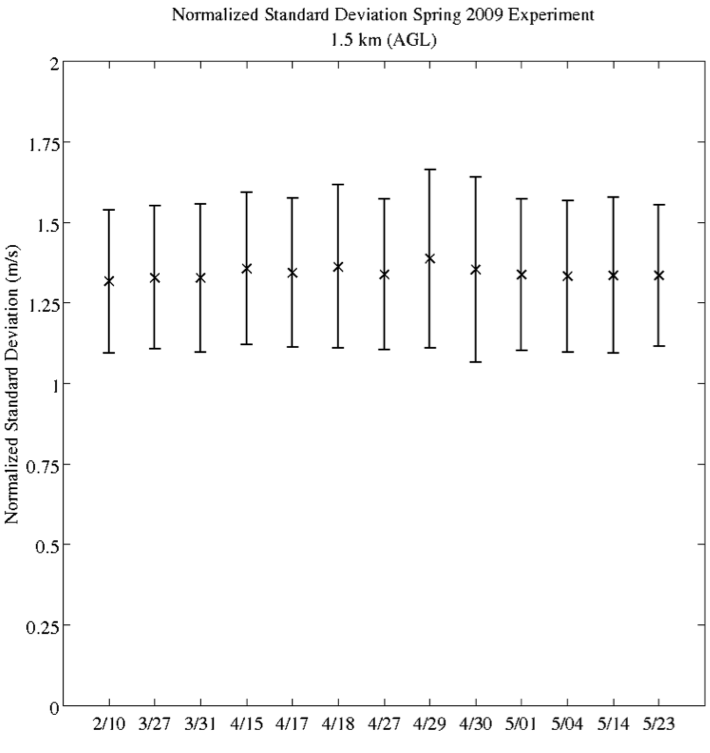

Figure 4.69: Bar chart for normalized standard deviation at 1.5km AGL.

Table 4.41: Statistics for normalized standard deviation at an altitude of 1.5km AGL

| Date | Mean (m/s) | std (m/s) | Minimum (m/s) | Maximum (m/s) |
|---|---|---|---|---|
| 02/10/2009 | 1.3 | 0.2 | 1.0 | 2.0 |
| 03/27/2009 | 1.3 | 0.2 | 1.0 | 2.0 |
| 03/31/2009 | 1.3 | 0.2 | 1.0 | 2.0 |
| 04/15/2009 | 1.4 | 0.2 | 1.0 | 2.0 |
| 04/17/2009 | 1.3 | 0.2 | 1.0 | 2.0 |
| 04/18/2009 | 1.4 | 0.3 | 1.0 | 2.0 |
| 04/27/2009 | 1.3 | 0.2 | 1.0 | 2.0 |
| 04/29/2009 | 1.4 | 0.3 | 1.0 | 2.0 |
| 04/30/2009 | 1.4 | 0.3 | 1.0 | 2.0 |
| 05/01/2009 | 1.3 | 0.2 | 1.0 | 2.0 |
| 05/04/2009 | 1.3 | 0.2 | 1.0 | 2.0 |
| 05/14/2009 | 1.3 | 0.2 | 1.0 | 2.0 |
| 05/23/2009 | 1.3 | 0.2 | 1.0 | 2.0 |

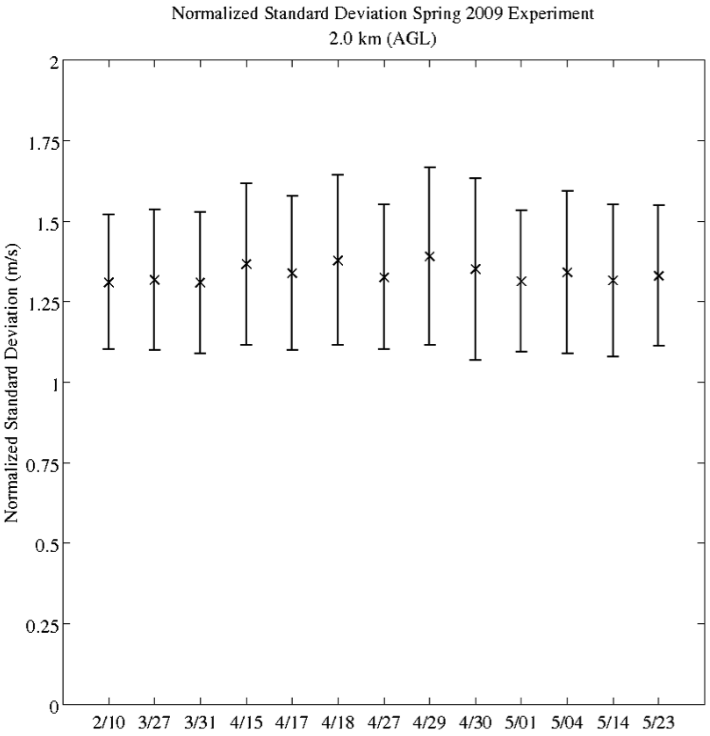

Figure 4.70: Bar chart for normalized standard deviation at 2.0km AGL.

Table 4.42: Statistics for normalized standard deviation at an altitude of 2.0km AGL

| Date | Mean (m/s) | std (m/s) | Minimum (m/s) | Maximum (m/s) |
|---|---|---|---|---|
| 02/10/2009 | 1.3 | 0.2 | 1.0 | 2.0 |
| 03/27/2009 | 1.3 | 0.2 | 1.0 | 2.0 |
| 03/31/2009 | 1.3 | 0.2 | 1.0 | 2.0 |
| 04/15/2009 | 1.4 | 0.3 | 1.0 | 2.0 |
| 04/17/2009 | 1.3 | 0.2 | 1.0 | 2.0 |
| 04/18/2009 | 1.4 | 0.3 | 1.0 | 2.0 |
| 04/27/2009 | 1.3 | 0.2 | 1.0 | 2.0 |
| 04/29/2009 | 1.4 | 0.3 | 1.0 | 2.0 |
| 04/30/2009 | 1.4 | 0.3 | 1.0 | 2.0 |
| 05/01/2009 | 1.3 | 0.2 | 1.0 | 2.0 |
| 05/04/2009 | 1.3 | 0.3 | 1.0 | 2.0 |
| 05/14/2009 | 1.3 | 0.2 | 1.0 | 2.0 |
| 05/23/2009 | 1.3 | 0.2 | 1.0 | 2.0 |

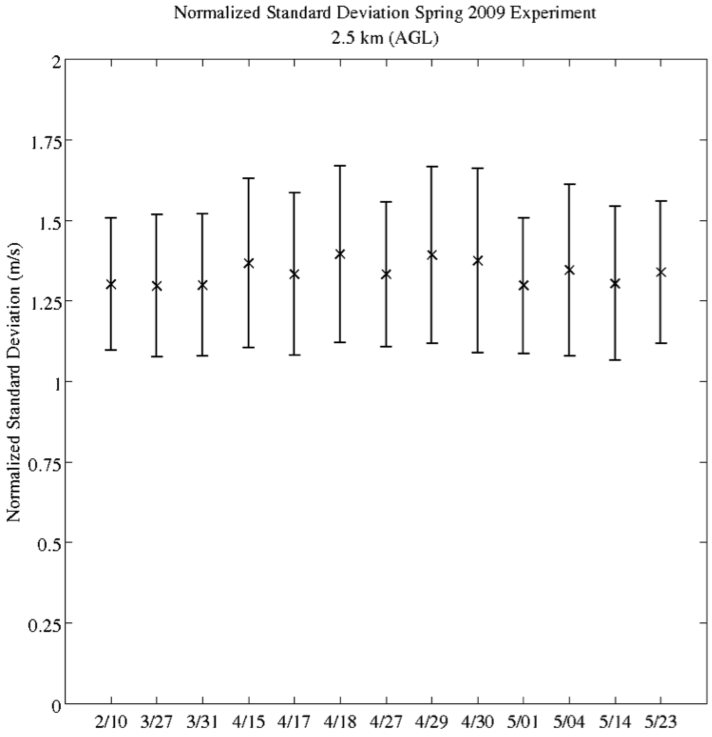

Figure 4.71: Bar chart for normalized standard deviation at 2.5km AGL.

Table 4.43: Statistics for normalized standard deviation at an altitude of 2.5km AGL

| Date | Mean (m/s) | std (m/s) | Minimum (m/s) | Maximum (m/s) |
|---|---|---|---|---|
| 02/10/2009 | 1.3 | 0.2 | 1.0 | 2.0 |
| 03/27/2009 | 1.3 | 0.2 | 1.0 | 2.0 |
| 03/31/2009 | 1.3 | 0.2 | 1.0 | 2.0 |
| 04/15/2009 | 1.4 | 0.3 | 1.0 | 2.0 |
| 04/17/2009 | 1.3 | 0.3 | 1.0 | 2.0 |
| 04/18/2009 | 1.4 | 0.3 | 1.0 | 2.0 |
| 04/27/2009 | 1.3 | 0.2 | 1.0 | 2.0 |
| 04/29/2009 | 1.4 | 0.3 | 1.0 | 2.0 |
| 04/30/2009 | 1.4 | 0.3 | 1.0 | 2.0 |
| 05/01/2009 | 1.3 | 0.2 | 1.0 | 2.0 |
| 05/04/2009 | 1.3 | 0.3 | 1.0 | 2.0 |
| 05/14/2009 | 1.3 | 0.2 | 1.0 | 2.0 |
| 05/23/2009 | 1.3 | 0.2 | 1.0 | 2.0 |

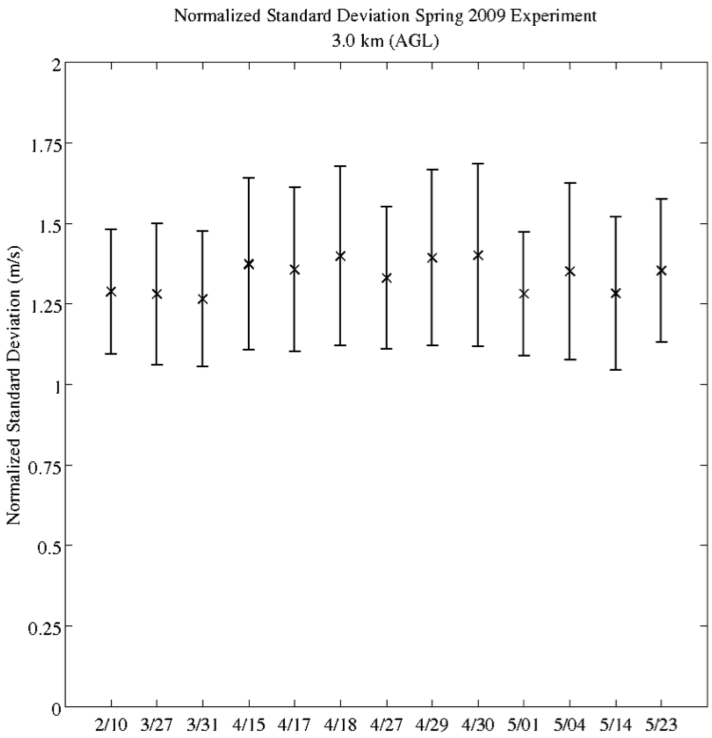

Figure 4.72: Bar chart for normalized standard deviation at 3.0km AGL.

Table 4.44: Statistics for normalized standard deviation at an altitude of 3.0km AGL

| Date | Mean (m/s) | std (m/s) | Minimum (m/s) | Maximum (m/s) |
|---|---|---|---|---|
| 02/10/2009 | 1.3 | 0.2 | 1.0 | 2.0 |
| 03/27/2009 | 1.3 | 0.2 | 1.0 | 2.0 |
| 03/31/2009 | 1.3 | 0.2 | 1.0 | 2.0 |
| 04/15/2009 | 1.4 | 0.3 | 1.0 | 2.0 |
| 04/17/2009 | 1.4 | 0.3 | 1.0 | 2.0 |
| 04/18/2009 | 1.4 | 0.3 | 1.0 | 2.0 |
| 04/27/2009 | 1.3 | 0.2 | 1.0 | 2.0 |
| 04/29/2009 | 1.4 | 0.3 | 1.0 | 2.0 |
| 04/30/2009 | 1.4 | 0.3 | 1.0 | 2.0 |
| 05/01/2009 | 1.3 | 0.2 | 1.0 | 2.0 |
| 05/04/2009 | 1.4 | 0.3 | 1.0 | 2.0 |
| 05/14/2009 | 1.3 | 0.2 | 1.0 | 2.0 |
| 05/23/2009 | 1.4 | 0.2 | 1.0 | 2.0 |

highway 28 and eventually affected the southeastern side of Anadarko, Ok (Chandrasekar et al., 2010b). Figure 4.73 shows the path of the tornado. The black shows the path of the tornado derived from the dual-Doppler retrievals, and the flags show the path derived from a damage survey taken after the event. The tornado was observed by both the Chickashsa (KSAO) and Cyril (KCYR) radars from 02:12:06 UTC until 02:47:09 UTC. The observation was well situated in the dual-Doppler region formed by Chickashsa and Cyril. Figure 4.74 shows a sequence of dual-Doppler retrievals for the observed tornado. Figures 4.75 - 4.81 show histograms of the normalized standard deviation of wind field retrieval at 0.0 kilometers, 0.5 kilometers, 1.0 kilometers, 1.5 kilometers, 2.0 kilometers, 2.5 kilometers, and 3.0 kilometers for the May 14, 2009 case. Table 4.45 summarizes the statistics for the histograms. At all altitude levels the standard deviation is between 0.2188 and 0.2414 m/s. This indicates that there is relatively little variation in the retrievals. At the 0.0 kilometer level the minimum possible normalized standard deviation is 0.9555 standard deviations from mean, where as the maximum possible normalized standard deviation is 3.5348 standard deviations from the mean. This indicates that a small percentage of the retrievals have a normalized standard deviation close to 2.0 m/s. Similar conclusions can be made about the other altitude levels. Table 4.46 gives the percentage of the retrievals with a normalized standard deviation less than or equal to 1.5 m/s, and the percentage of retrievals with a normalized standard deviation greater than 1.5 m/s. At all altitude levels more than 80% of the retrievals had a normalized standard deviation less than or equal to 1.5 m/s. This indicates that a large percentage of the retrievals fall within beam crossing angles between 41.8103° and 90°. These results demonstrate that the quality of the dual-Doppler retrievals are sufficient for observing a an EF2 tornado. These results also show that a large percentage of the retrievals have a normalized standard deviation less then 1.5 m/s at altitude levels between 0.0 kilometers and 3.0 kilometers, which indicates that the quality of the retrievals is sufficient for hazardous weather events.

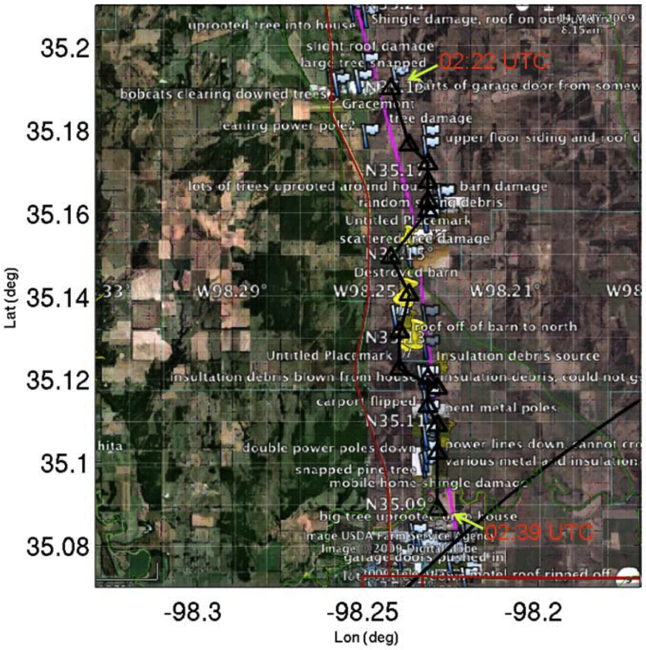

Figure 4.73: Path of an observed EF2 tornado on May 14, 2009.

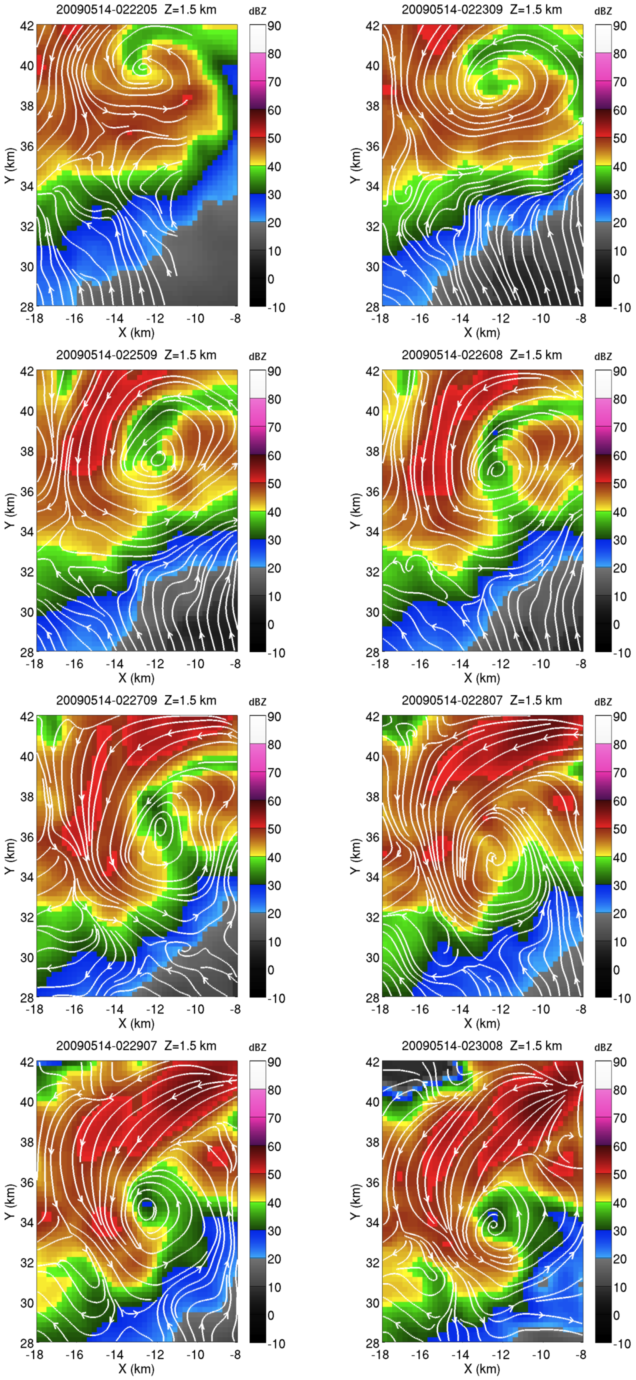

Figure 4.74: Sequence of wind field retrievals from observed EF2 tornado on May 14, 2009.

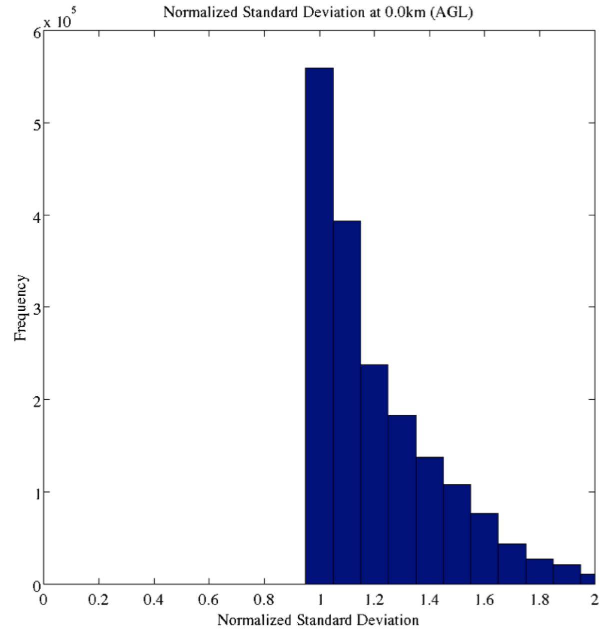

Figure 4.75: Histogram of normalized standard deviation of wind field retrieval at 0.0 kilometers

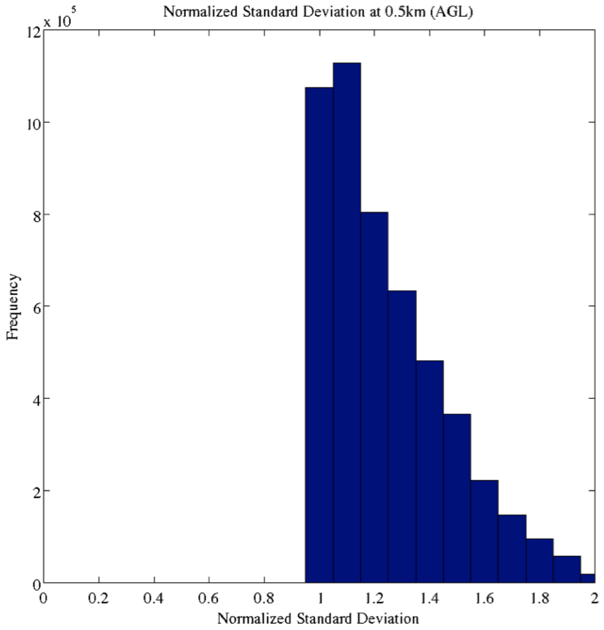

Figure 4.76: Histogram of normalized standard deviation of wind field retrieval at 0.5 kilometers

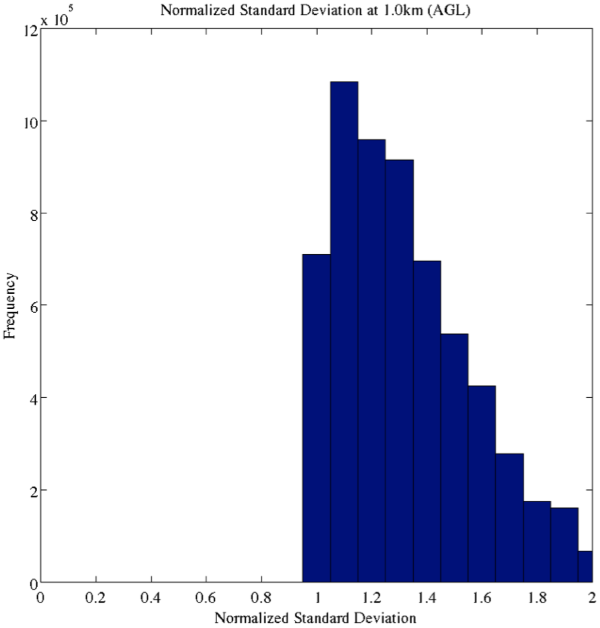

Figure 4.77: Histogram of normalized standard deviation of wind field retrieval at 1.0 kilometers

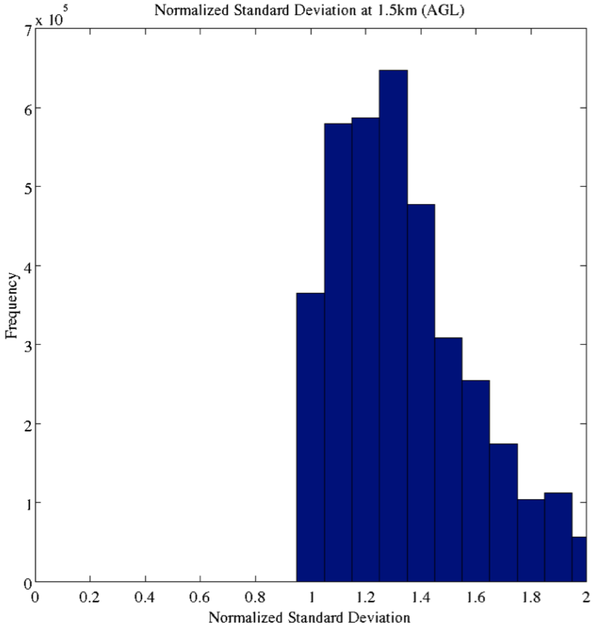

Figure 4.78: Histogram of normalized standard deviation of wind field retrieval at 1.5 kilometers

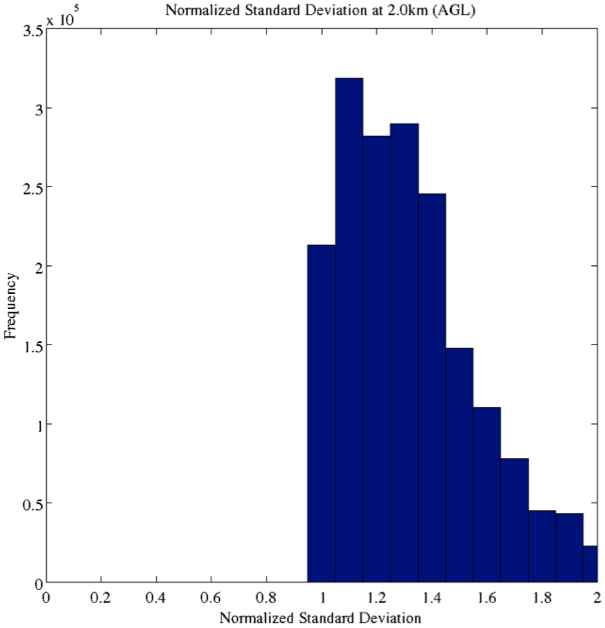

Figure 4.79: Histogram of normalized standard deviation of wind field retrieval at 2.0 kilometers

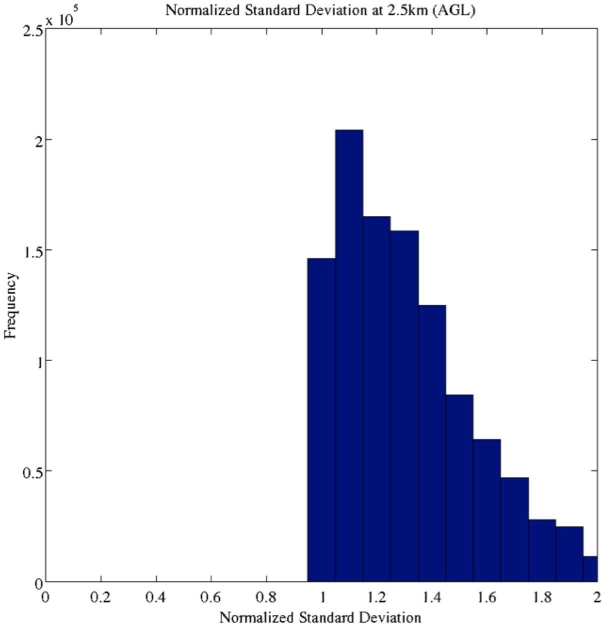

Figure 4.80: Histogram of normalized standard deviation of wind field retrieval at 2.5 kilometers

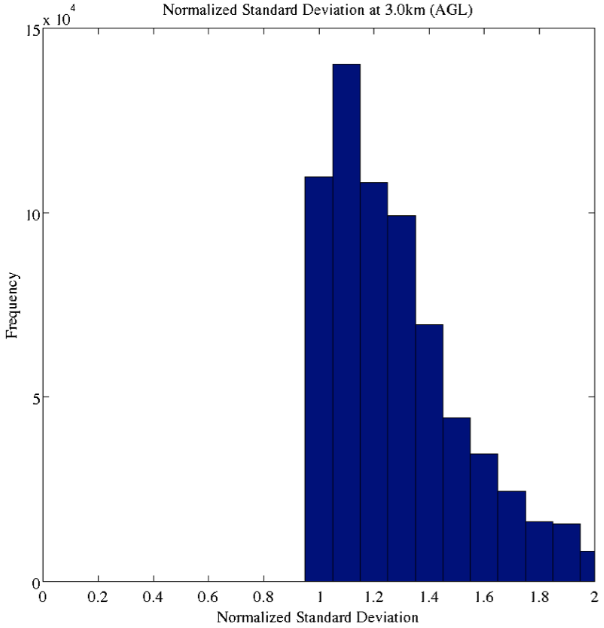

Figure 4.81: Histogram of normalized standard deviation of wind field retrieval at 3.0 kilometers

Table 4.45: Statistics for wind field retrieval on May 14, 2009

| Height (AGL) | Mean (m/s) | std (m/s) | Minimum (m/s) | Maximum (m/s) |
|---|---|---|---|---|
| 0.0 km | 1.2 | 0.2 | 1.0 | 2.0 |
| 0.5 km | 1.2 | 0.2 | 1.0 | 2.0 |
| 1.0 km | 1.3 | 0.2 | 1.0 | 2.0 |
| 1.5 km | 1.3 | 0.2 | 1.0 | 2.0 |
| 2.0 km | 1.3 | 0.2 | 1.0 | 2.0 |
| 2.5 km | 1.3 | 0.2 | 1.0 | 2.0 |
| 3.0 km | 1.3 | 0.2 | 1.0 | 2.0 |

Table 4.46: Percentage of retrievals $\leq 1.5$ m/s and $> 1.5$ m/s

| Height (AGL) | $\leq 1.5$ m/s | $> 1.5$ m/s |
|---|---|---|
| 0.0 km | 90.1% | 9.9% |
| 0.5 km | 89.3% | 10.7% |
| 1.0 km | 81.6% | 18.4% |
| 1.5 km | 80.9% | 19.1% |
| 2.0 km | 83.4% | 16.6% |
| 2.5 km | 83.5% | 16.5% |
| 3.0 km | 85.3% | 14.7% |

## 4.4 Visualization and Applications

### 4.4.1 Visualization

Traditionally dual- and multi-Doppler derived wind fields have been visualized using arrows. For the CASA dual-Doppler system two visualization techniques, arrows and streamlines, were evaluated during the 2009 spring experiment. In an arrow visualization representation of the wind field the length of the arrow is determined by the magnitude of the $u$ and $v$ components, $\sqrt{u^2 + v^2}$, and the direction of the arrow is determined by $tan^{-1}\left(\frac{v}{u}\right)$. The arrows are placed on a regular grid. Figure 4.82 shows an example of the arrow style visualization.

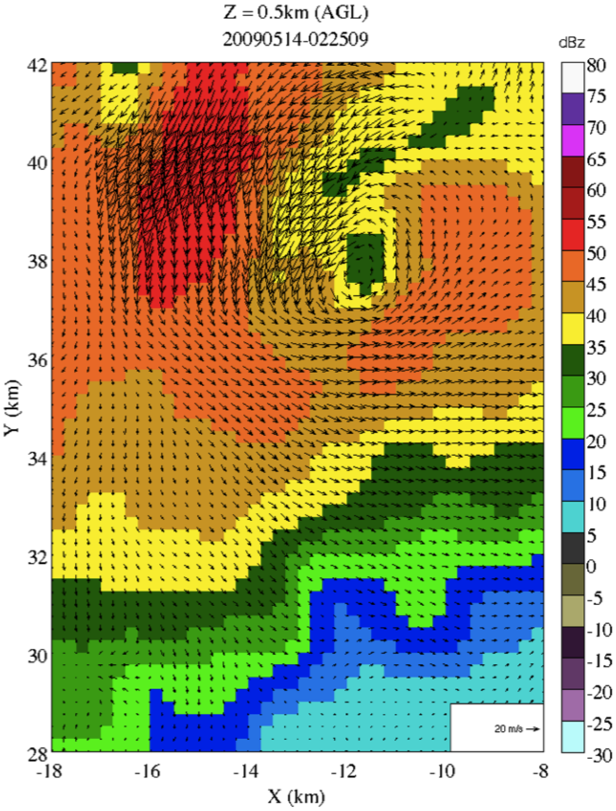

Figure 4.82: Example of arrow style visualization for observed EF2 tornado on May 14, 2009.

The streamline representation of the wind field is a family of curves that are instantaneously tangent to the wind field. Consider a vector field **n** with components

$(\delta_1, \delta_2, \delta_3)$ in a Cartesian system with coordinates $(x_1, x_2, x_3)$. Then the streamline becomes a solution to the equations (Aminov, 2000):

$$\frac{dx_1}{ds} = \delta_1 (x_1, x_2, x_3) \tag{4.2}$$

$$\frac{dx_2}{ds} = \delta_2 (x_1, x_2, x_3) \tag{4.3}$$

$$\frac{dx_3}{ds} = \delta_3 (x_1, x_2, x_3) \tag{4.4}$$

The magnitude of the vector is given by the line density of the streamlines. The higher the density the more intense the wind. However, streamlines do not give a quantitative vector magnitude. Streamlines are represented with and without arrows. The exclusion of arrows make direction of flow ambiguous. Streamlines with arrows are used to visualize the retrieved wind field, which reduces the ambiguity in the direction of the wind. Figure 4.74 shows a sequence of a wind field using streamline style visualization.

Studies have been performed to determine the best methods for visualizing two-dimensional vector fields (Laidlaw et al., 2005, 2001). In Laidlaw et al. (2005) six visualization techniques were evaluated. Both arrow style visualization and streamlines were included in the evaluation. The study had experts and non-experts in the field of fluid mechanics perform three tasks, advecting a particle, locating a critical point, and identifying a critical point. These tasks were selected as common tasks researchers perform on vector field visualizations. From the study the authors found that visualizations that attempt to visually represent integral curves (or streamlines) and show flow directionality had better task performance. Other authors, Ware (2004), have noted that vectors placed on a regular grid, for example arrow visualization, are less effective then vectors placed using streamlines. However, the best visualization method depends on the task (Laidlaw et al., 2005).

Two tasks are associated with the visualization of the wind fields. The first task is being able to resolve large scale features such as the general direction and magnitude of the wind. The second is being able to resolve small scale features such as circulation associated with tornadoes. Streamlines are not ideal for large grids since it can be computationally intensive to generate the streamline. For this reason the arrow style technique is used to visualize the retrieved wind field for the entire CASA domain, figure 4.83.

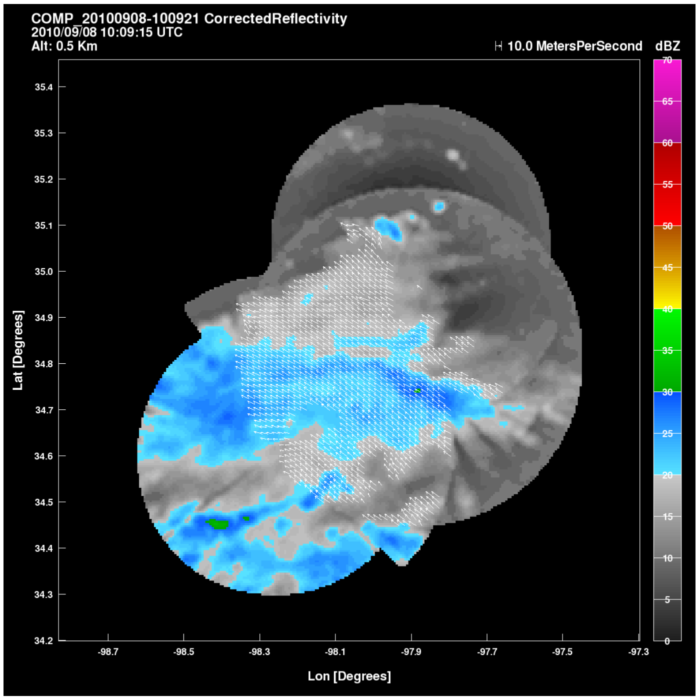

Figure 4.83: Example arrow style visualization for entire CASA domain.

The representation of a wind field using arrows has several drawbacks when visualizing small scale features within a retrieved wind field. First visualization of high resolution wind fields requires that the density of arrows be reduced. The high density of vectors makes it difficult to clearly identify features of the wind field, therefore wind fields are traditionally visualized using every other grid point. The second draw back to visualizing wind fields is setting the scale appropriately. If the scale is set too large for the dynamic range of the retrieved wind field then the arrows are too small to interrupt magnitude information, figure 4.84. If the scale is too small then the arrows overpower each other and making the features difficult to identify, figure 4.85. Streamlines offer several advantages over the arrow style visualization techniques. First, streamlines are not affected by the density of vectors, which makes them ideal for high resolution wind fields. Second, streamlines do not require a scale in order to be visualized, thus features within the retrieved wind field are clearly visible. The streamline visualization technique is used when analysing select areas of the retrieved wind field figure 4.74.

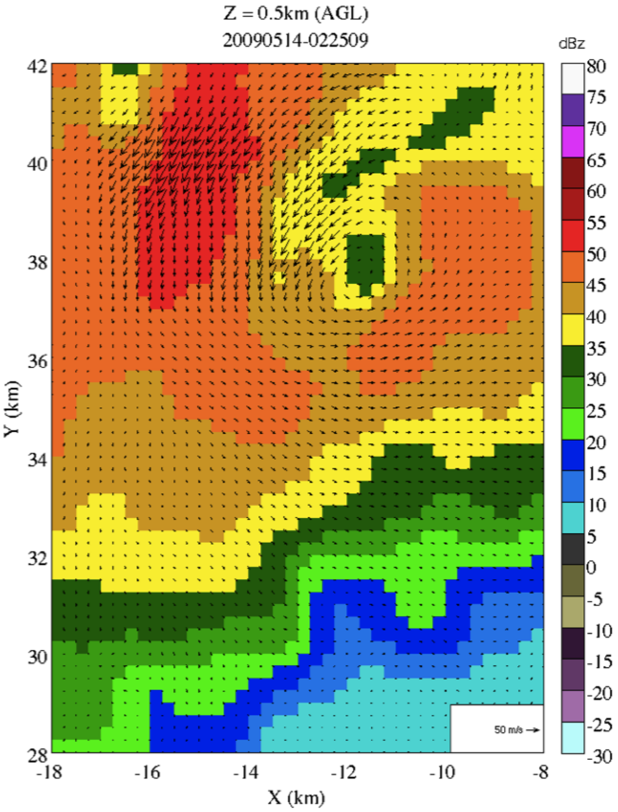

Figure 4.84: Example arrow style visualization when scale is set too large

### 4.4.2 Vorticity and Divergence

Application of dual-Doppler data is the measurement of vorticity and divergence. Vorticity is a measure of the amount of rotation a fluid has about a local axis, and is

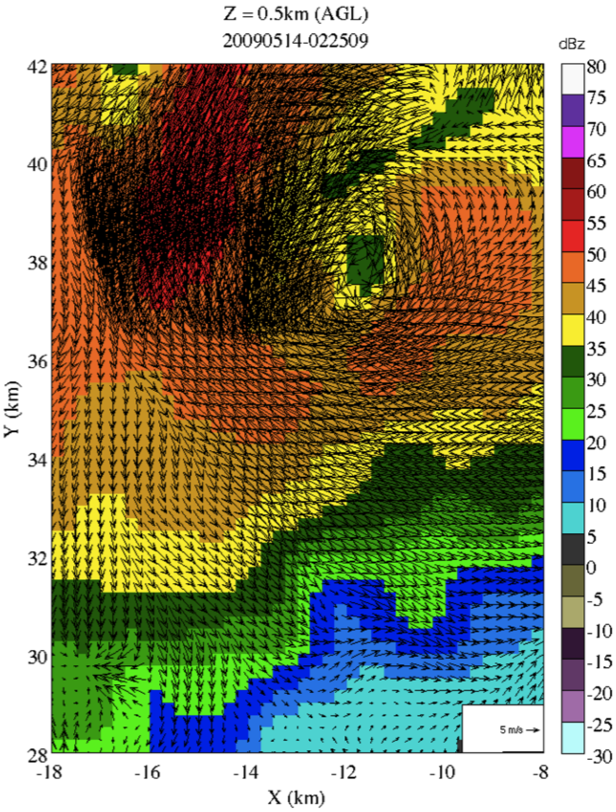

Figure 4.85: Example arrow style visualization when scale is set too small

defined as the curl of the velocity field.

$$\overrightarrow{w} = \overrightarrow{\bigtriangledown} \times \overrightarrow{v} \tag{4.5}$$

Vertical vorticity is given as

$$w_z = \frac{\partial v}{\partial x} - \frac{\partial u}{\partial y} \tag{4.6}$$

In the atmosphere, the air motions of clouds are especially subject to rotation. In the northern hemisphere cyclonic rotation is in the counterclockwise direction, and is associated with positive vorticity. On the other hand, anti-cyclonic rotation is in the clockwise directions and is associated with negative vorticity.

By applying the vorticity equation to a dual-Doppler derived wind field circulation features, such as tornadoes, can be detected within the IP1 dual-Doppler regions. Also the vertical vorticity can be used to find the center of the circulation. The center is associated with the maximum vertical vorticity. A sequence of vorticity fields for an observed tornado on May 14, 2009 is shown in figure 4.86. The highest vorticity values are in the center of the circulation where the rotation of the air is at its greatest. The vorticity values in the area of the circulation are around $0.04s^{-1}$. These values are similar to those found in Wurman et al. (2007a,b). The vorticity computations show that the dual-Doppler data can be used to make accurate computations of vorticity, which can be used for further kinematic studies.

Divergence is the measurement of how a vector field behaves like a sink or a source at any given point and is defined as:

$$f = \bigtriangledown \cdot \overrightarrow{v} \tag{4.7}$$

In the atmosphere divergence is the outflow of air. Downward motion (positive divergence) in the air is a result of the divergence of horizontal winds. Upward motion (negative divergence) in the air is a result of the convergence of horizontal winds.

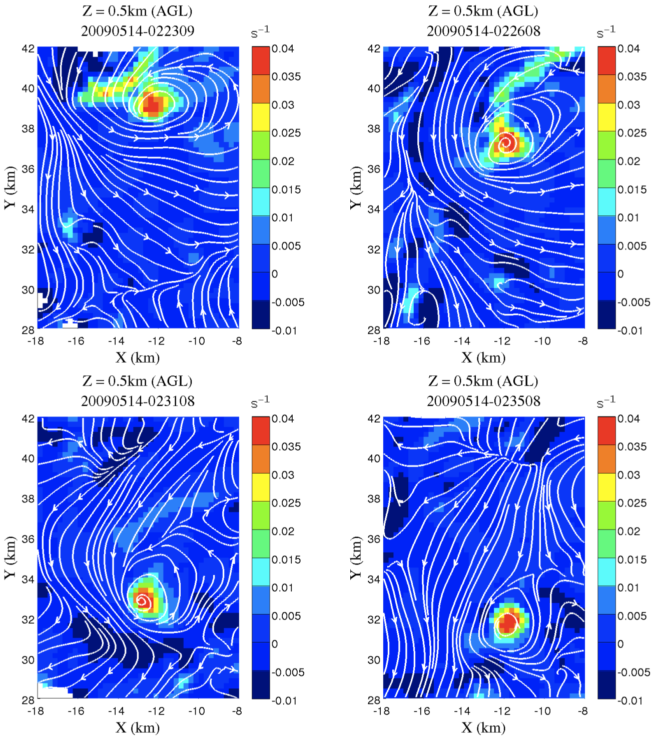

Figure 4.86: Vorticity sequence from an observed EF2 tornado on May 14, 2009.

Divergence computations from dual-Doppler data can be used diagnose upward and downward air motion. Divergence computations from dual-Doppler data have also been used to study the structure of tornadoes Wurman et al. (2007a). In figure 4.87 a sequence of divergence fields are shown for an observed EF2 tornado on May 14, 2009. The divergence fields are similar to those found in Wurman et al. (2007b). In Wurman et al. (2007b), there is strong divergence and convergence around the area of the circulation, which is also observed in figure 4.87. These divergence computations indicate that the dual-Doppler data can be used to compute reliable divergence fields that are comparable with observations made by others.

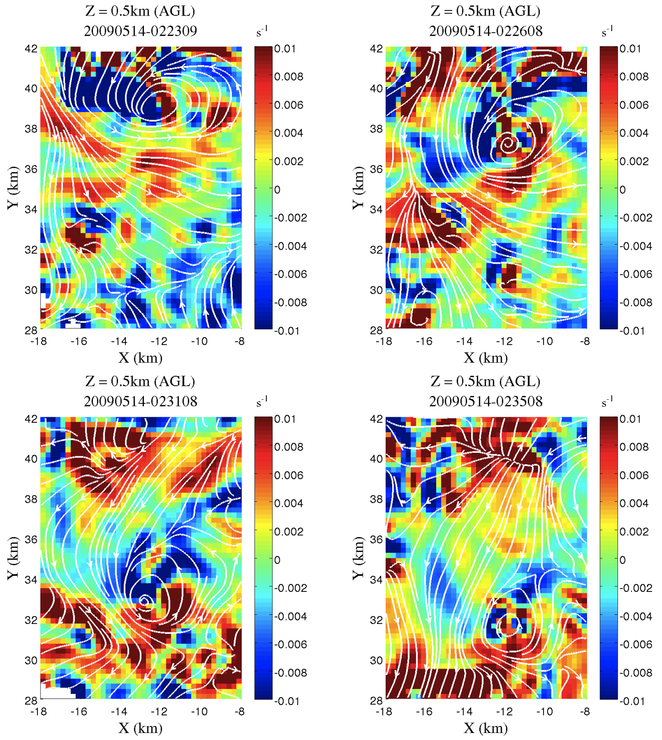

Figure 4.87: Divergence sequence from an observed EF2 tornado on May 14, 2009.

## 4.5 Summary

This chapter has provided an extensive evaluation of the two subsystems making up the CASA IP1 dual-Doppler system, namely the scan strategy subsystem and retrieval subsystem. An evaluation of the scan strategy subsystem provided an analysis of the three main components of the dual-Doppler scan strategy, beam crossing angle, vertical coverage,and synchronization time of coordinated scans. The evaluation of the scan strategy subsystem was done using the cases from the 2009 spring experiment and an event occurring on April 2, 2010. It was shown that the beam crossing angles for each pair provided sufficient bounds on the collected data for wind field retrieval. It was also shown that the vertical coverage of the IP1 radars with the current heartbeat was insufficient for retrieving the vertical components of the wind field accurately. Finally it was shown that the radars that make up a pair were well synchronized. The evaluation of the retrieval subsystem was done using the data from the 2009 spring experiment and a tornadic event occurring on May 14, 2009. The evaluation showed the retrievals in the first three kilometers was within the bounds provided by the scan strategy subsystem, and had a sufficiently low enough error to be considered accurate.The final part of the chapter discussed the visualization and applications of the CASA dual-Doppler system.Two visualization techniques, arrow and streamline, were discussed. The computation of vorticity and divergence were also discussed. Overall the dual-Doppler system works well for retrieving accurate horizontal wind fields that can be used for decision making and scientific analysis.

# CHAPTER 5

# CONCLUSIONS AND SUGGESTIONS FOR FUTURE WORK

## 5.1 Conclusion

A description and comprehensive evaluation of the CASA dual-Doppler system has been presented in this thesis. Chapter one gave on overview of the wind field retrieval problem with the current network of NEXRAD radars and has described how the CASA IP1 network solves this problem. Also an overview of current dual- and multi-Doppler networks along with applications of retrieved wind fields was given. Chapter two has described the CASA IP1 radar systems and the moment data fields needed for wind field retrievals. Chapter three gave a discussion of the theory for wind field retrievals and provided a description of the CASA IP1 dual-Doppler system. The discussion of the dual-Doppler theory included an overview of data resampling techniques, dual- and multi-Doppler wind field retrieval techniques, and an error analysis of the retrieved wind field. The description of the CASA IP1 dual-Doppler system described the scan optimization subsystem and the retrieval subsystem. Chapter four of this thesis gave an evaluation of the CASA dual-Doppler system. The two subsystems, scan optimization and retrievals, were comprehensively evaluated. The chapter also provided an evaluation of wind field visualization techniques, and applications of wind field retrievals.

In chapter two of this thesis the methods for resampling of radar data and wind field retrievals were described. Also a description of the CASA dual-Doppler system was provided. Resampling to a common Cartesian grid is an important step in wind field retrievals. This places all the data on to a common frame of reference. The resampling method described in chapter two was the distance dependent weighted averaging (DDWA) scheme. The DDWA scheme uses a Cressman weighting method to interpolate from radar coordinates to Cartesian coordinates. The weighting nature of the DDWA scheme results in a filtered version of the original data field. The resampled reflectivity and velocity data are used for wind field retrievals. Methods for retrieving three-dimensional winds using two or more radars was given. The methods for retrieving horizontal winds using two radars was first developed, and then extended to n radars. A description of vertical wind field retrievals was also provided. Three integration methods for solving the mass continuity equation where discussed. The discussed methods were upward integration, downward integration, and the variational method. The upward integration method is inherently error prone due to sensitivities in setting the boundary condition. For this reason the upward integration method is not preferred. The downward integration method is the preferred method since it is less sensitive to errors in setting the boundary condition at the top of the storm. However, the downward integration method requires that the storm is topped throughout the entire dual- or multi-Doppler region. The variational method performs the integration in the upward direction first and than distributes the errors throughout the vertical column during a downward integration. The variational method requires that the boundary condition be set at the ground and top of the storm, which can be difficult since the storm is not always topped in the dual- and multi-Doppler region. An error analysis of the retrieved horizontal wind field was also provided. It was established that the minimum beam crossing angle needed for reliable horizontal wind field retrievals is 30 °.

The description of the CASA dual-Doppler system focused on three parts, the dual-Doppler coverage in the IP1 network, the scanning subsystem, and the retrieval subsystem. In the description of the dual-Doppler coverage it was shown that there are six possible dual-Doppler pairs within the CASA IP1 network. The location of the six pairs within the network were shown, and the dual-Doppler coverage of each pair was given. Also the triple- and quad-Doppler regions in the IP1 network were discussed. In the description of the scan strategy subsystem the specifications for the subsystem were given. It was shown that the scan strategy optimization was designed to determine the best dual-Doppler pair based on the location of a storm. The optimization accounts for the mechanically scanned nature of the IP1 radars, and uses the steering limitations of the radars as a constraint in the optimization. Therefore the scan strategy optimization is performed at the maximum coverage altitude of the IP1 radars. The best pair is determined by minimizing the error variance at the maximum altitude. Also it was discussed that the optimization prefers radar pairs that have lower elevation angles at long ranges. Based on the optimization constraints a cost function was given. The description of scan optimization subsystem also included a discussion of real-time operation. The section described how the lookup table of geo-located dual-Doppler zones are used with storm detection and end user requirements to determine the best dual-Doppler scan. Also a description of contouring and convex polygon generation and its application to determining the best dual-Doppler scan was given. In the description of the retrieval subsystem the specification of the data resampling and retrieval algorithm were given. The reflectivity and radial velocity data are resampled from radar coordinates to a common Cartesian grid using a DDWA interpolation scheme which uses a Cressman weight with a radius of influence of less than 1 kilometer. The grid for the real-time wind field retrievals is 140 kilometers by 140 kilometers by 10 km, with a resolution of 0.5 km in the x, y, and z direction. The grid is centered at ($34.8276^\circ$ N, $-98.1007^\circ$ W, 0.0 m). A description of the retrieval process and data quality methods were given. The horizontal wind field is retrieved using the theory described in chapter three. The retrieval process uses both dual- and multi-Doppler regions of the IP1 network to retrieve the wind field. The retrieved wind field is quality controlled using a local de-spiking routine and beam crossing thresholding. The local de-spiking routine masks outlying grid points that are seven standard deviations from the local mean as bad points. Grid points that are in beam crossing angles less then 30 ° are also masked as bad points. The resulting wind field is stored on the SOCC in a netCDF file.

Chapter four of this thesis presented an evaluation of the CASA dual-Doppler system. The evaluation focused on the two subsystems that make up the CASA dual-Doppler system, the scan strategy and the retrievals. Also an evaluation of wind field visualization techniques and applications of the retrieved wind fields were given. The evaluation of the both subsystems included an assessment of both subsystems during the 2009 spring experiment and detailed case studies. The evaluation of the scan strategy subsystem assessed four groups of parameters, the dual-Doppler coverage per heartbeat, beam crossing angle, vertical coverage, and data synchronization. The evaluation of the number of pairs tasked per heartbeat found that the dual-Doppler scan strategy was able to provide continuous dual-Doppler coverage throughout the life of an event, which is import to end-users. The evaluation of the beam crossing angle focused on two parts, the beam crossing angle itself and the expected error in the retrieval. A key finding was that for all six dual-Doppler pairs in the IP1 network the average beam crossing angles were within 30° and 90°. It was also shown that the beam crossing angle could be used to determine the expected wind field retrieval error for the collected data. From the beam crossing angle it was verified that the expected error in the wind field retrieval would be between 1.0 m/s and 1.5 m/s. It was found that the scan strategy does a satisfactory job of maintaining scans that consist of beam crossing angles between 30° and 90°. The assessment of the vertical coverage focused on three parameters, the number of elevation angles in a volume, the maximum elevation angle in a volume, and the maximum observable height in a volume. The evaluation was used to asses the possibility of using the CASA IP1 system for vertical air motion retrievals. From the assessment of the maximum observable altitude it was established that the systemwide scan strategy used in the CASA system was not suitable for vertical velocity retrievals. On average the maximum scanned height was around 5 kilometers AGL, which is not sufficient for retrieving the vertical component of a wind field using a reliable method. The evaluation of data synchronization was done in order to assess how closely related the data was collected between radars in a pair. This evaluation found the data between two radars was well matched in time and on average did not exceed five seconds. However, there were times when the synchronization time exceeded the system heartbeat. These situations where due to network latencies between the radar sites and the SOCC.For the scan strategy evaluation a case from April 2, 2010 was selected in order to assess the effect that attenuation in the dual-Doppler regions had on the scan strategy. The case study examined how the structure of the best pair regions would change based on the level of attenuation in the dual-Doppler region, and the location of storm features. From this case study new best pair regions were derived when one of the four radars suffered from significant attenuation. When two radars suffer attenuation in the dual-Doppler regions then the best regions becomes the dual-Doppler regions for the remaining radars.

The second part of the evaluation focused on the assessment of the wind field retrieval. For each event occurring for the 2009 spring experiment the error in the wind field retrieval was assessed. This was done for altitudes from 0.0 kilometers AGL to 3.0 kilometers AGL with 0.5 kilometer intervals. The evaluation found that on average the error in the wind field retrieval was between 1.0 m/s and 1.5 m/s. And that the average error never exceeds 2.0 m/s. This gives an indication that the wind field retrievals are of high quality. This also shows that the topology of the IP1 network is such that the error in the wind fields are minimized. A case study was also done for the retrievals for a severe wind event. The selected case was from May 14, 2009 when an EF2 tornado was observed by the CASA IP1 system. It was found that the error in the wind field retrieval was acceptable for a reliable wind field in a severe weather event. The case study showed that the quality of the wind field at seven altitude levels was sufficient for resolving small scale features such as the circulation of a tornado. Also part of the evaluation of the CASA dual-Doppler system was the assessment of visualization techniques. This section showed that the type of visualization method depended on the task required for the visualization. If the retrieved wind field was used to visualize large scale effects, such as general magnitude and direction of the wind, then arrow based visualization techniques were appropriate since computational complexity of the generating streamlines is too great. However if the retrieved wind field is being used to visualize small scale features, such as circulation associated with a tornado, then streamline visualization techniques were more appropriate, since they do not rely on scale of the arrow which can make it difficult to visualize the desired feature. Two applications of the wind the field data were provided. The applications discussed were the computation of vertical vorticity and divergence. Vertical vorticity and divergence field were computed for the May 14, 2009 case. The resulting fields were compared against vorticity and divergence fields found in literature. From the comparison it was found that the vorticity and divergence fields were comparable to those found in literature for dual-Doppler observations of tornadoes. This shows that the CASA dual-Doppler system is able to make meaning and reliable wind field retrievals that can be used for scientific study. Overall this study has presented a comprehensive evaluation and description of the CASA dual-Doppler system. The provided case studies have shown that the system has satisfactory operation and is capable of providing retrieved wind fields that can be used for emergency decision and scientific applications.

## 5.2 Future Work

Although an extensive evaluation of the CASA of the dual-Doppler system has been given, several extensions to this work can be done. Some of these extensions are but not limited to

- Although it was shown that with the current system scan strategy does not enable reliable vertical velocity retrievals it would be worthwhile to look at different scan strategies that would increase the chances of topping a storm throughout all of the dual-Doppler domains within the CASA IP1 system. Being able to top the storm at all locations of the dual-Doppler domains would provide a way to increase the ability of using CASA IP1 radars for kinematic studies.

- It was shown that in the presence of attenuation the best pair regions would change as radars that suffer significant attenuation are removed from the scan optimization. This concept can be extended for a larger network. In this case the best pair regions can be determined for when all radars available for the optimization. Then individual radars for a larger network can be removed to generate new best pair regions for attenuation effects. Also the explicit inclusion of attenuation can be included in the scan strategy optimization.

- One extension of the applications of the retrieved wind field data would be to examine methods for feature detection that uses retrieved wind field data and other parameters such as reflectivity, velocity and dual-polarized products. The feature detection could then use vorticity data with other data fields to detect circulation in overlapping regions of the network, or divergence data can be used with other fields to detect updrafts and downdrafts within the network.

- One method used in the CASA IP1 radar system is to use radar data to make decision that are used to steer the radars. Currently reflectivity data is used to steer the radars. Adding velocity data and data from the retrieved wind can improve the decision process by focusing radar coverage to areas with hazardous wind features. For instance, this will improve the ability to detect the beginnings of hazardous wind events, which will increase the lead time for severe wind related warnings and advisories.

# BIBLIOGRAPHY

Aminov, Y., 2000: *The Geometry of Vector Fields*. Gordon and Breach Science Publishers, 172 pp.

Armijo, L., 1969: A theory for the determination of wind and precipitation velocities with doppler radars. *J. Atmos. Sci.*, **26**, 570–573.

Atlas, D., R. Srivastava, and R. Sekon, 1973: Doppler radar characteristics of precipitation at vertical incidence. *Rev. of Geophysics and Space Physics*, **11**, 1–35.

Barnes, S., 1964: A technique for maximizing details in numerical weather map analysis. *J. Appl. Meteor.*, **3**, 396–409.

Bharadwaj, N., V. Chandrasekar, and F. Junyent, 2010: Signal processing system for the casa integrated project 1 radars. *J. Atmos. Oceanic Technol.*, In press.

Bohn, V. and R. Srivastava, 1975: Random errors in wind and precipitation fall speed measurement by a triple-doppler radar system. *University of Chicago Laboratory for Atmospheric Probing*, 44.

Bringi, V., T. Keenan, and V. Chandrasekar, 2001: Correcting c-band radar reflectivity and differential reflectivity data for rain attenuation: A self-consistent method with constraints. *IEEE Trans. Geosci. Remote Sens.*, **39**, 1906–1915.

Bringi, V. N. and V. Chandrasekar, 2001: *Polarimetric Doppler Weather Radar: Principles and Applications*. Cambridge University Press, 636 pp.

Carbone, R., M. Carpernter, and C. Burghart, 1985: Doppler radar sampling limitations in convective storms. *J. Atmos. Oceanic Technol.*, **2**, 357 – 361.

Chandrasekar, V., M. Martinez, and S. Zhang, 2010a: The CASA dual-doppler system. *Proc. IEEE IGARSS 2010.*, IEEE, Honolulu, Hawaii, 4138–4141.

Chandrasekar, V., Y. Wang, N. Bharadwaj, S. Zhang, M. Martinez, D. Mclaughlin, B. J., M. Zink, and B. Phillips, 2010b: Observation of an ef2 tornado winds using networked radar test-bed. *Proc. IEEE Radar Conference 2010.*, IEEE, Washington, DC, 1167–1171.

Chandrasekar, V., D. Willie, Y. Wang, and S. Lim, 2009: Attenuation margin requirements in a networked radar system for observation of precipitation. IEEE, Cape Town, South Africa, 957–959.

Chong, M., J. Georgis, S. Bousquet, S. Brodzik, C. Burghart, S. Cosma, U. Germann, V. Gouget, R. J. Houze, C. James, S. Prieur, R. Rotunno, F. Roux, J. Vivekanandan, and Z. Zeng, 2000: Real-time wind synthesis from doppler radar observations during the mesoscale alpine programme. *Bull. Amer. Meteor. Soc.*, **81**, 2953–2962.

Cressman, G., 1959: An operational objective analysis system. *Mon. Wea. Rev.*, **87**, 357–361.

Crum, T. and R. Alberty, 1993: The WSR-88D and the WSR-88D operational support facility. *Bulletin of the American Meteorological Society*, **74**, 1669 – 1687.

Davies-Jones, R., 1979: Dual-doppler radar coverage area as a function of measurement accuracy and spatial resolution. *J. Appl. Meteor.*, **18**, 1229–1233.

Dolan, B. and S. Rutledge, 2007: An integrated display and analysis methodology for multivariable radar data. *J. Appl. Meteor. Climatol.*, **46**, 1196–1213.

— 2010: Using CASA IP1 to diagnose kinematic and micropyhsical interactions in a convective storm. *Mon. Wea. Rev.*.

Friedrich, K. and M. Hagen, 2004: Evaluation of wind vectors measured by a bistatic doppler radar network. *J. Atmos. Oceanic Technol.*, **21**, 1840–1854.

Given, T. and P. Ray, 1994: Response of a two-dimensional dual-doppler radar wind synthesis. *J. Atmos. Oceanic Technol.*, **11**, 239–255.

Heymsfield, G., 1978: Kinematic and dynamic aspects of the harrah tornadic storm analyzed from dual-doppler radar data. *Mon. Wea. Rev.*, **106**.

Junyent, F., V. Chandrasekar, D. McLaughlin, E. Insanic, and N. Bharadwaj, 2010: The casa integrated project 1 network radar system. *J. Atmos. Oceanic Technol*, **27**, 61–78.

Kessinger, C., P. Ray, and C. Hane, 1987: The oklahoma squall line of 19 may 1977. part I: A multiple doppler analysis of convective and stratiform structure. *J. Atmos. Sci.*.

Laidlaw, D., R. Kirby, C. Jackson, J. Davidson, T. Miller, M. da Silva, W. Warren, and M. Tarr, 2005: Comparing 2D vector field visualization methods: A user study. *IEEE Trans. on Visualization and Computer Grapics*, **11**, 59 – 70.

Laidlaw, D., R. Kirby, T. Miller, M. da Silva, J. Davidson, W. Warren, and M. Tarr, 2001: Quantitative comparative evaluation of 2D vector field visualization methods. *Proc. IEEE Visualization '01*, IEEE, San Diego, CA.

Lakshmanan, V., T. Smith, G. Stumpf, and K. Hondi, 2007: The warning decision support system - integrated information. *Wea. Forcasting*, **22**, 596–612.

Matejka, T. and B. Bartles, 1998: The accuracy of vertical air velocities from doppler radar data. *Mon. Wea. Rev.*, **126**, 92–117.

Miller, L. and R. Strauch, 1974: A dual-doppler radar method for the determination of wind velocities within precipitation weather systems. *Remote Sensing of the Environment*, **3**, 219–235.

Miller, M., R. Avissar, L. Berg, S. Edgerton, M. Fischer, K. B. Jackson, T., P. Lamb, G. McFarquhar, Q. Min, B. Schmid, M. Torn, and D. Turner, 2007: SCG cloud and land surface interaction campaign (CLASIC): Science and implementation plan. Technical report, U.S. Department of Energy Atmospheric Radiation Measurement (ARM) Climate Research Facility, Washington D.C.

Mohr, C. and R. Vaughan, 1979: A economical procedure for cartesian interpolation and display of reflectivity factor data in three dimensional space. *J. Appl. Meteor.*, **18**, 661 – 670.

O'Brien, J., 1970: Alternative solutions to the classical vertical velocity problem. *J. Appl. Meteor.*, **9**, 197–203.

Protat, A. and I. Zawadzki, 1999: A variational method for real-time retrieval of three-dimensional wind field from multiple-doppler bistatic radar network data. *J. Atmos. Oceanic Technol*, **16**.

Ray, P., K. Wagner, K. Johnson, J. Stephens, W. Bumgarner, and E. Mueller, 1978: Triple-doppler observations of a convective storm. *J. Appl. Meteor.*, **17**, 1201–1212.

Ray, P., C. Ziegler, W. Bumgarner, and R. Serafin, 1980: Single- and multiple- doppler radar observations of a convective storm. *J. Climate Appl. Meteor.*, **24**, 688 – 698.

Satoh, S. and J. Wurman, 2003: Accuracy of wind field observed by a bistatic doppler radar network. *J. Atmos. Oceanic Technol.*

Siggia, A. and J. Passarelli, 2004: Gaussian model adaptive processing (GMAP) for improved ground clutter cancellation and moment calculation. *European Conference on Radar in Meteorology and Hydrology*, ERAD., 67–73.

Trapp, R. and C. Dowswell, 2000: Radar data objective analysis. *J. Atmos. Oceanic Technol.*, **17**, 105 – 120.

Wang, Y., V. Chandrasekar, and B. Dolan, 2008: Development of scan strategy for dual-doppler retrieval in a networked radar system. *Proc. IEEE IGARSS 2008.*, IEEE, Boston, MA, 322–325.

Ware, C., 2004: *Information Visualization: Perception for Design*. Morgan Kaufmann, 486 pp.

Wurman, J., Y. Richardson, C. Alexander, S. Weygandt, and P. Zhang, 2007a: Dual-doppler analysis of a tornadic storm undergoing mergers and repeated tornadogensis. *Mon. Wea. Rev.*, **135**, 736–758.

— 2007b: Dual-doppler analysis of winds and vorticity budget terms near a tornado. *Mon. Wea. Rev*, **135**, 2392–2405.

Zink, M., D. Westbrook, S. Abdallah, B. Horling, E. Lyons, V. Lakamraju, V. Manfredi, J. Kurose, and K. Hondl, 2005: Meteorological Command and Control: An End-to-end Architecture for a Hazardous Weather Detection Sensor Network. *Proceedings of the ACM Workshop on End-to-End, Sense-and-Respond Systems, Applications, and Services (EESR 05)*, Seattle, WA, 37–42.